

AD A090291

LEVEL

10

F

A summary report, entitled
DEVELOPMENT AND APPLICATION OF THE MAXIMUM ENTROPY METHOD
AND OTHER
SPECTRAL ESTIMATION TECHNIQUES

by

William R. King

King Research
10209 Westford Drive
Vienna, Virginia 22180

DTIC
ELECTE
OCT 15 1980

DISTRIBUTION STATEMENT A

Approved for public release;
Distribution Unlimited

prepared for

Office of Naval Research
Arlington, Virginia 22217
Contract number N00014-80-C-0519

1 September 1980

DDC FILE COPY

394223

30 9 24 002

FORWARD

This summary report is a collection of four separate progress reports prepared under three contracts, which are all sponsored by the Office of Naval Research in Arlington, Virginia. This report contains the results of investigations into the application of the maximum entropy method (MEM), a high resolution, frequency and wavenumber estimation technique. The report also contains a description of two new, stable, high resolution spectral estimation techniques that is provided in the final report section. Many examples of wavenumber spectral patterns for all investigated techniques are included throughout the report.

The maximum entropy method is also known as the maximum entropy spectral analysis (MESA) technique, and both names are used in the report. Many MEM wavenumber spectral patterns are demonstrated using both simulated and measured radar signal and noise data. Methods for obtaining stable MEM wavenumber spectra are discussed, broadband signal detection using the MEM prediction error transform (PET) is discussed, and doppler radar narrowband signal detection is demonstrated using the MEM technique. It is also shown that MEM cannot be applied to randomly sampled data.

The two new, stable, high resolution, spectral estimation techniques discussed in the final report section, are named the Wiener-King and the Fourier spectral estimation techniques. The two new techniques have a similar derivation based upon the Wiener prediction filter, but the two techniques are otherwise quite different. Further development of the techniques and measurement of the technique spectral characteristics is recommended for subsequent investigation.

William R King

TABLE OF CONTENTS

<u>SECTION TITLE</u>	<u>PAGE</u>
STABLE MESA ANTENNA PATTERNS	
I. Introduction	
A. Wavenumber Power Spectra	1
B. High Resolution Power Spectral Techniques	1
C. Application of MESA	2
II. The Maximum Entropy Method	2
III. MESA Snapshots	4
IV. MESA Instabilities	5
V. Averaging Techniques	
A. Averaged Filter Weights	8
B. Averaged Prediction Errors	11
C. Averaged Covariance Matrix	15
D. Averaged MESA Snapshots	21
VI. Adaptive Filter Weights	25
VII. Resolution	34
VIII. Conclusions	37
BROADBAND SIGNAL DETECTION WITH THE SCOT AND SCOT-PET	
1.0 Introduction	
1.1 Background	40
1.2 Comparative Evaluation	41
2.0 Theory	
2.1 Crosscorrelation	41
2.2 Smoothed Coherence Transform (SCOT)	42
2.3 The SCOT-PET Function	43

SECTION TITLE

PAGE

3.0	Data Simulation	46
4.0	Examples of Crosspower Functions	48
5.0	Examples of Crosscorrelation, SCOT, and SCOT-PET Time Functions	49
6.0	ROC Curves	
6.1	Construction Based Upon 100 Time Functions	50
6.2	Other BB SNR Values	51
6.3	Partially Coherent Broadband Noise	52
7.0	Summary	

RESOLUTION AND DETECTION CHARACTERISTICS OF THE MAXIMUM ENTROPY METHOD

1.0	Introduction	68
2.0	Radar Data	
2.1	The Maximum Entropy Method	69
2.2	The Maximum Likelihood Method	69
2.3	Results of Analysis	70
3.0	Signal Detection	72
4.0	Summary	73

POWER SPECTRA USING RANDOM SAMPLING AND THE W-K SPECTRAL ESTIMATION TECHNIQUE

I.	Random Data Sampling	
	Introduction	86
	Examples of Fourier Antenna Patterns	86
	Examples of MEM Wavenumber Patterns	91
II.	The W-K Spectral Estimation Technique	
	Introduction	96
	Prediction Error Definition	96
	Prediction Filter	97
	Power Spectra	100

SECTION TITLE

PAGE

Prediction Filter	97
Power Spectra	100
Example Wavenumber Power Spectra	101
III. The All-Pole and Zero-Pole Fourier Spectral Estimator	
Introduction	111
Wiener Prediction Filter	111
Filter Definition	112
All-Pole Solution	112
Zero-Pole Solution	113

STABLE MESA ANTENNA PATTERNS

I. INTRODUCTION

A. Wavenumber Power Spectra

Power spectral analysis techniques are applicable to the processing of spatial multi-channel antenna data, since computed antenna patterns are actually wavenumber power spectra, $P(k)$. The wavenumber k is a function of θ , the signal angle of incidence to the antenna as follows:

$$k = (2\pi/\lambda)\sin(\theta)$$

Because an antenna array is a collector of spatially sampled data, any power spectral technique which is designed for such discrete data sets is applicable for computing antenna patterns.

B. High Resolution Power Spectral Techniques

During recent years several high resolution power spectral techniques have been developed (or rediscovered) for use with discrete data sets. Some of the techniques are: the maximum entropy method (1), the autoregressive model (2), the moving average model (3), the Yule-Walker technique (4), and the maximum likelihood method (5). Of these techniques the maximum entropy, autoregressive, and Yule-Walker techniques are all pole models, the moving average technique is an all zero model, and maximum likelihood is only a criteria function applicable to any model. Most of these methods are described in a tutorial review article (6). These particular methods have also been investigated and compared in two reports (7), (8) in which the best results were achieved with the maximum entropy method.

More conventional high resolution Fourier methods have also been recently developed (9), (10), (11), but have not been so thoroughly investigated. As a consequence, in this paper several methods are investigated for applying the maximum entropy spectral

analysis technique (MESA) to the processing of spatial, uniformly sampled data.

C. Application of MESA

Several methods of applying MESA to spatial data are investigated. In particular spatial data, which is simulated for an 8 element linear antenna array, is processed with MESA and the Burg technique (1). The Burg technique is a recursive method for evaluating the MESA filter weights, which substantially reduces the number of calculations required of the more conventional inverse matrix evaluation method.

MESA antenna patterns (wavenumber spectra) may be computed upon the collection of the set of 8 spatial data samples at any instant of time. Such "snapshot" patterns are inherently inconsistent and unstable. However it is possible to compute stable MESA antenna patterns using one of several stabilization techniques. It remains only to determine which technique provides sufficient stability for an acceptable averaging period without destroying the desired high resolution property which is characteristic of MESA. Averaging techniques which are investigated employ a time average of one of the following sets of variables:

- a.) filter weights
- b.) prediction errors
- c.) covariance matrix
- d.) "snapshot" patterns

And as an alternative to averaging, stabilization may also be achieved with use of time adaptive filter weights. In particular a set of adaptive filter weights, which are defined as proportional to the prediction error (12), are utilized in conjunction with a proportionality constant (convergence parameter) to comprise a stable, adaptive MESA processing technique.

II. THE MAXIMUM ENTROPY METHOD

The MESA technique, as the name implies, originated (1) by

maximizing the entropy of a signal mixed with noise. However, the same filter weights may also be derived (13) by whitening the Wiener prediction error filter as specified for discrete data samples (14). The resulting maximum entropy wavenumber spectra $P(k)$ is given as follows:

$$P(k) = \frac{P_N}{\left| 1 + \sum_{n=1}^N \gamma_n^N \exp(ikn\Delta x) \right|^2} \quad (1)$$

where

- N = number of filter weights ($1 \leq N \leq M$)
- M = number of data samples
- P_N = total noise power
- Δx = antenna element spacing
- γ_n^N = n th prediction error filter weight of a set of N weights.

The variables of eqn. (1), which are computed using a set of equations known as the "Burg technique", are listed as follows:

a.) Total Noise Power P_N

$$\begin{aligned} P_1 &= r_0 \text{ (} r_0 \text{ is the data set autocorrelation function)} \\ P_{n+1} &= P_n \left[1 + (\gamma_{n+1}^{n+1})^2 \right] \quad \text{for } (1 \leq n \leq N) \end{aligned} \quad (2)$$

b.) Filter Weights γ_n^{N+1}

$$\gamma_1^{N+1} = 1.0$$

$$\gamma_n^{N+1} = \gamma_n^N + \gamma_{N+1}^{N+1} (\gamma_{N-n+2}^N)^* \quad \text{for } (2 \leq n \leq N) \quad (3)$$

$$\gamma_{N+1}^{N+1} = \frac{-2 \sum_{n=1}^{M-N} (B_n^N)^* \cdot F_{N+n}^N}{\sum_{n=1}^{M-N} \left[(B_n^N)^2 + (F_{N+n}^N)^2 \right]} \quad \text{for } (1 \leq N \leq M-1) \quad (4)$$

c.) Forward Prediction Error F_n^N

$$F_{K+1}^1 = X_{K+1} \quad \text{for } (1 \leq K \leq M)$$

$$F_K^{N+1} = \gamma_{N+1}^{N+1} \cdot B_{K-N}^N + F_K^N \quad \text{for } (N+1 \leq K \leq M) \quad (5)$$

d.) Backward Prediction Error B_K^N

$$B_K^1 = X_K \quad \text{for } (1 \leq K \leq M-1)$$

$$B_K^{N+1} = (\gamma_{N+1}^{N+1})^* \cdot F_{K+N}^N + B_K^N \quad \text{for } (1 \leq K \leq M-N) \quad (6)$$

where the Kth data sample = X_K for $(1 \leq K \leq M)$

III. MESA SNAPSHOTS

It is possible to compute an antenna pattern with MESA using only one set of M data samples all recorded at the same instant of time. For example, consider one set of 8 data samples collected with 8 uniformly spaced antennas. The Burg technique equations, eqns. (1-6) are initially evaluated for $N=1$ and $M=8$, and then evaluated repeatedly for increasing unit incremental values of N up to the desired value of N provided that $(1 \leq N \leq 7)$.

However the final value of N must be such that $(NS \leq N)$ where NS is the number of signals present in the given data set X_K .

Consider a MESA snapshot pattern evaluated for $N=4, M=8$ where the Burg technique equations are evaluated repeatedly for $(1 \leq N \leq 4)$. A MESA snapshot pattern of one signal incident at ± 10 degrees (0 degrees is broadside to the antenna) and a signal-to-noise ratio of 15 dB is shown in Fig. 1a. The 8 data points contain Gaussian, white noise, simulated using a set of 8 random numbers computed for a generator "seed" value of 1 ($IR=1$). Another MESA snapshot shown in Fig. 1b, is computed using a different set of 8 random numbers for which $IR=2$.

The single signal is located accurately at ± 10 degrees (within ± 0.5 degrees) in both MESA snapshots of Fig. 1. The side peaks, which are randomly located, occur at different positions in the two snapshots. The total number of peaks, which represent the poles of eqn. (1), is always less or equal to the value of N , the number of filter weights. Since the two independent data sets used in the computed antenna patterns of Fig. 1 are considered to be recorded at two different instances of time, MESA snapshots are clearly time variant when computed with short ($M=8$) data sets. It is evident that some stabilizing technique is needed in the application of MESA to short data sets, so that computed MESA antenna patterns are invariant and repeatable in time for stationary data.

IV. MESA INSTABILITIES

Besides the side peak location instability depicted by Fig. 1, another instability associated with MESA is the inaccurate representation of signal peaks. Signal peaks may not be accurately located at very low signal-to-noise ratios or when other signals are present at adjacent angles. Nearby signals cause distortion in both signal location and in relative signal peak height. It has been noted (15) that isolated MESA signal peaks are not linearly related to the signal-to-noise ratios, but the actual relationship

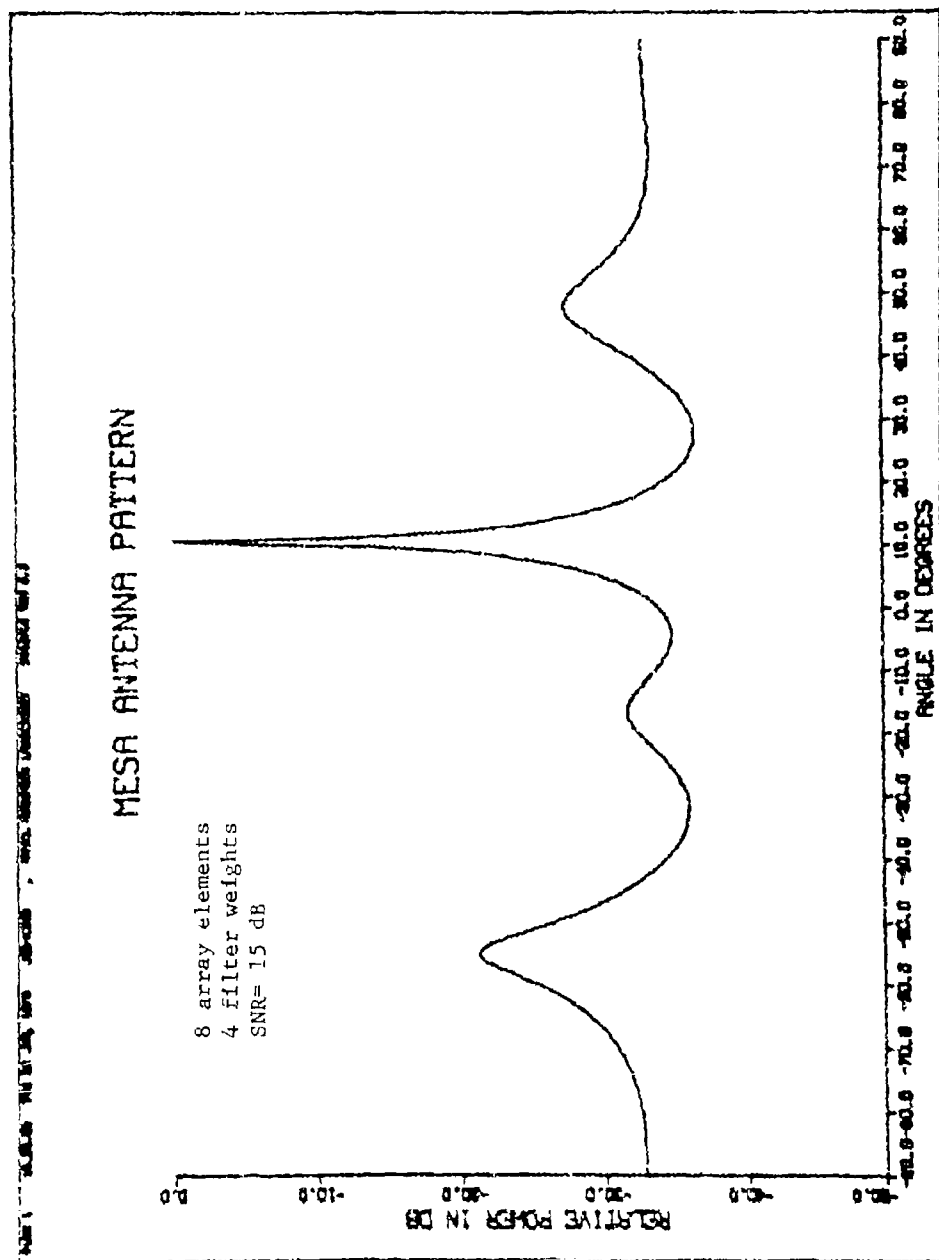


Fig. 1a - MESA snapshot, one signal, IR=1

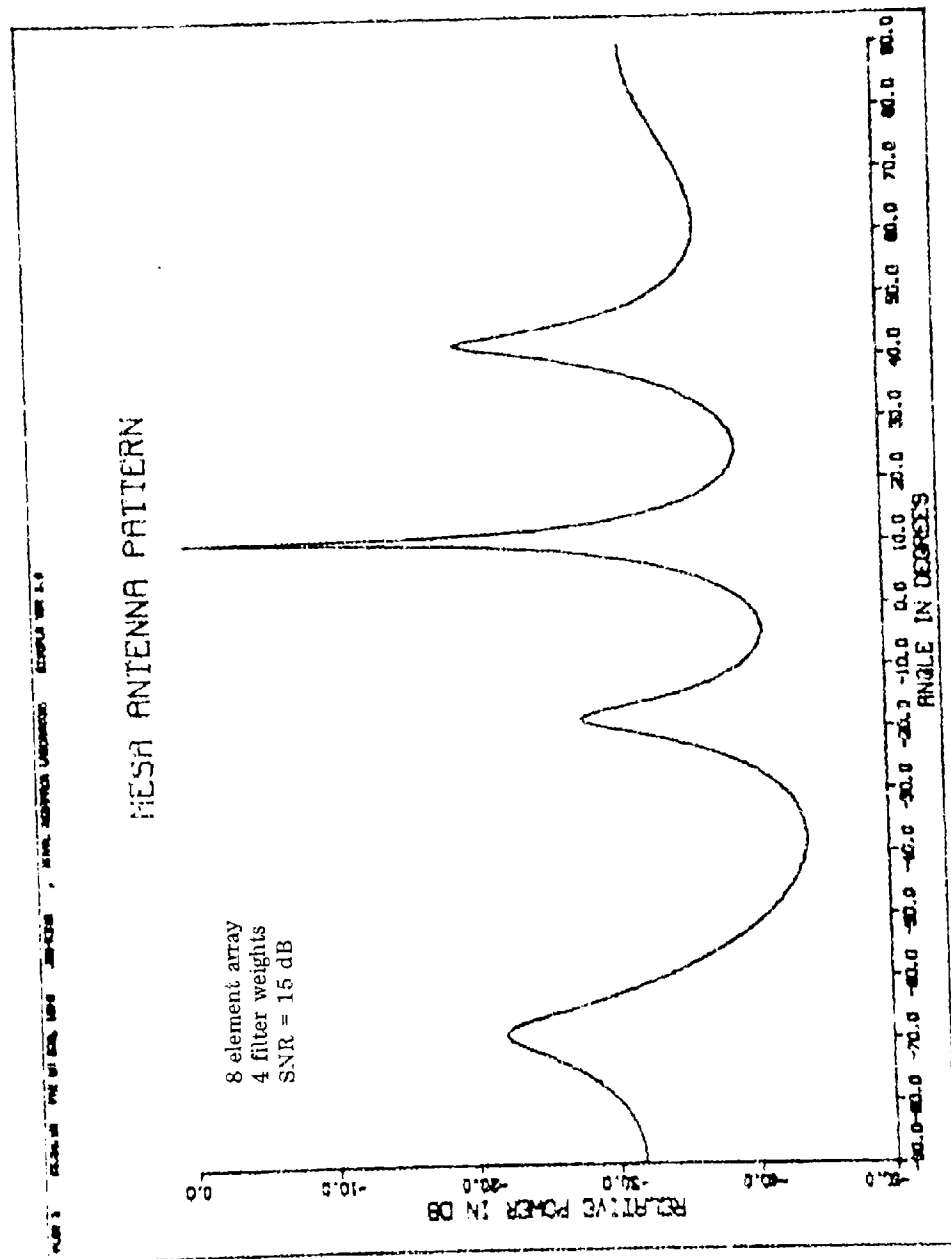


Fig. 1b - MESA snapshot, one signal, IR=2

has not been demonstrated. Both the power level and relative phase of adjacent signals affect the accuracy of the MESA power spectra. Such signal instabilities have been noted previously (14).

The noise field associated with a multi-channel antenna array may also be a source of signal distortion. Split signal peaks are a common problem with MESA snapshots (16). An example of how such problems arise is depicted in Figs. 2 and 3. The MESA snapshot of Fig. 2 is computed using only 3 complex noise data points (no signal present) and a 5 point filter ($N=5$). The MESA snapshot of Fig. 2 has two large noise peaks near 0 and 10 degrees. When a signal having a 10 dB signal-to-noise ratio is introduced into the same noise field ($IR=5$), at an angle of +5 degrees, the signal is ambiguously represented in the MESA snapshot of Fig. 3 by a split peak (two adjacent peaks). The split peak which is observed in Fig. 3 near the signal angle of +5 degrees is apparently due to interference of the two noise peaks which are present at angles near the signal. Since the complex noise peaks are randomly located, split peaks caused by such noise interference may be eliminated with some form of averaging within the MESA algorithm. The same set of complex noise data ($IR=5$) is used in the evaluation of several averaging techniques.

V. AVERAGING TECHNIQUES

A. Averaged Filter Weights

It is not necessary to average a complete set of filter weights. γ_n^{N+1} , where ($1 \leq n \leq N$), since all filter weights for ($2 \leq n \leq N$) are a function of the last filter weight γ_{N+1}^{N+1} as given by eqn. (3). The last filter weight, which is given by eqn. (4) is computed and averaged over L data sets.

$$\gamma_{N+1}^{N+1} = \frac{1}{L} \sum_{k=1}^L \gamma_{N+1}^{N+1}(k\Delta t)$$

In all, a total of ($L \cdot M$) data points are utilized in computing such an averaged MESA antenna pattern.

An average MESA antenna pattern utilizing an averaged

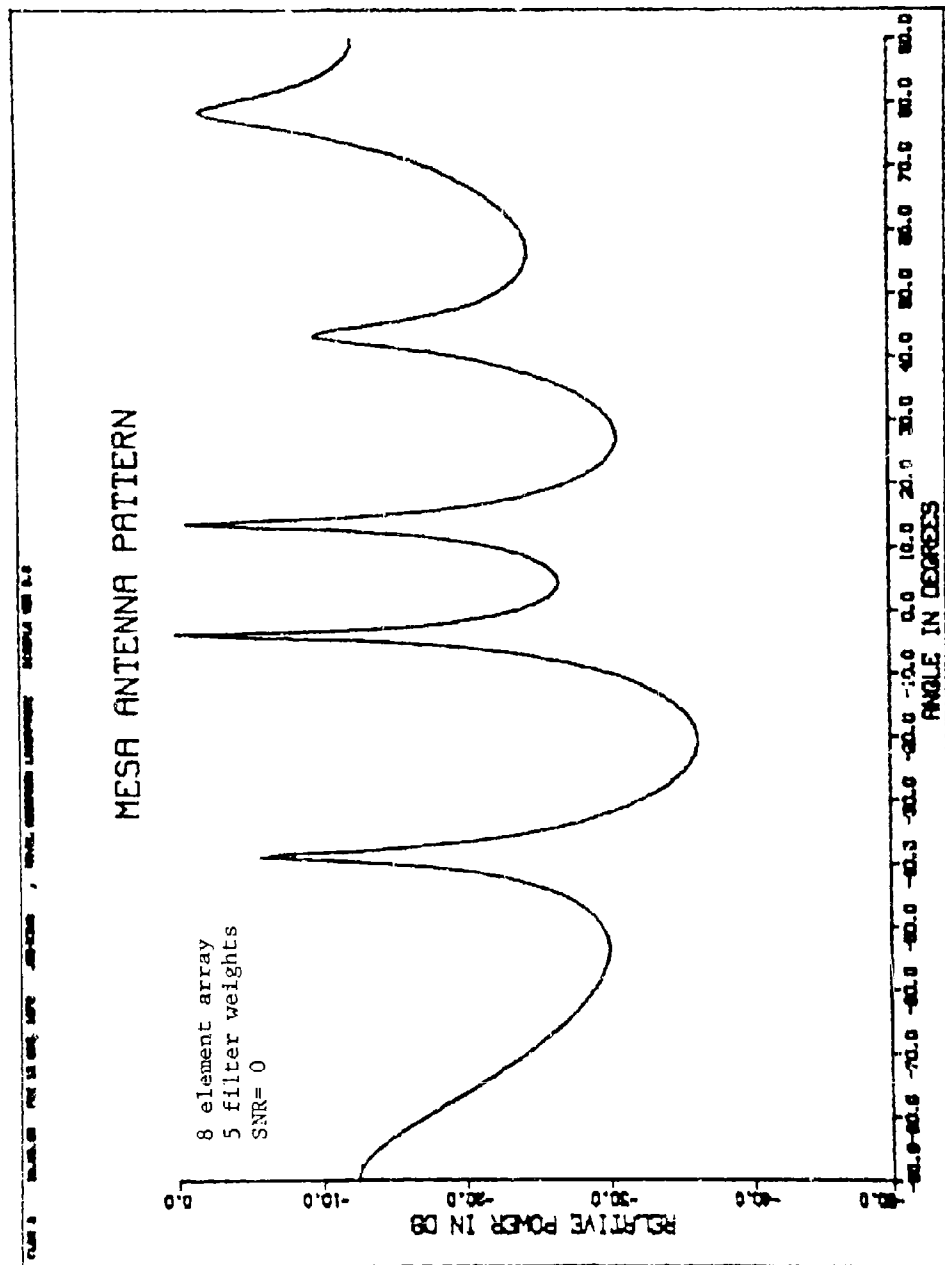


Fig. 2 - MESA snapshot, no signal, IR=5

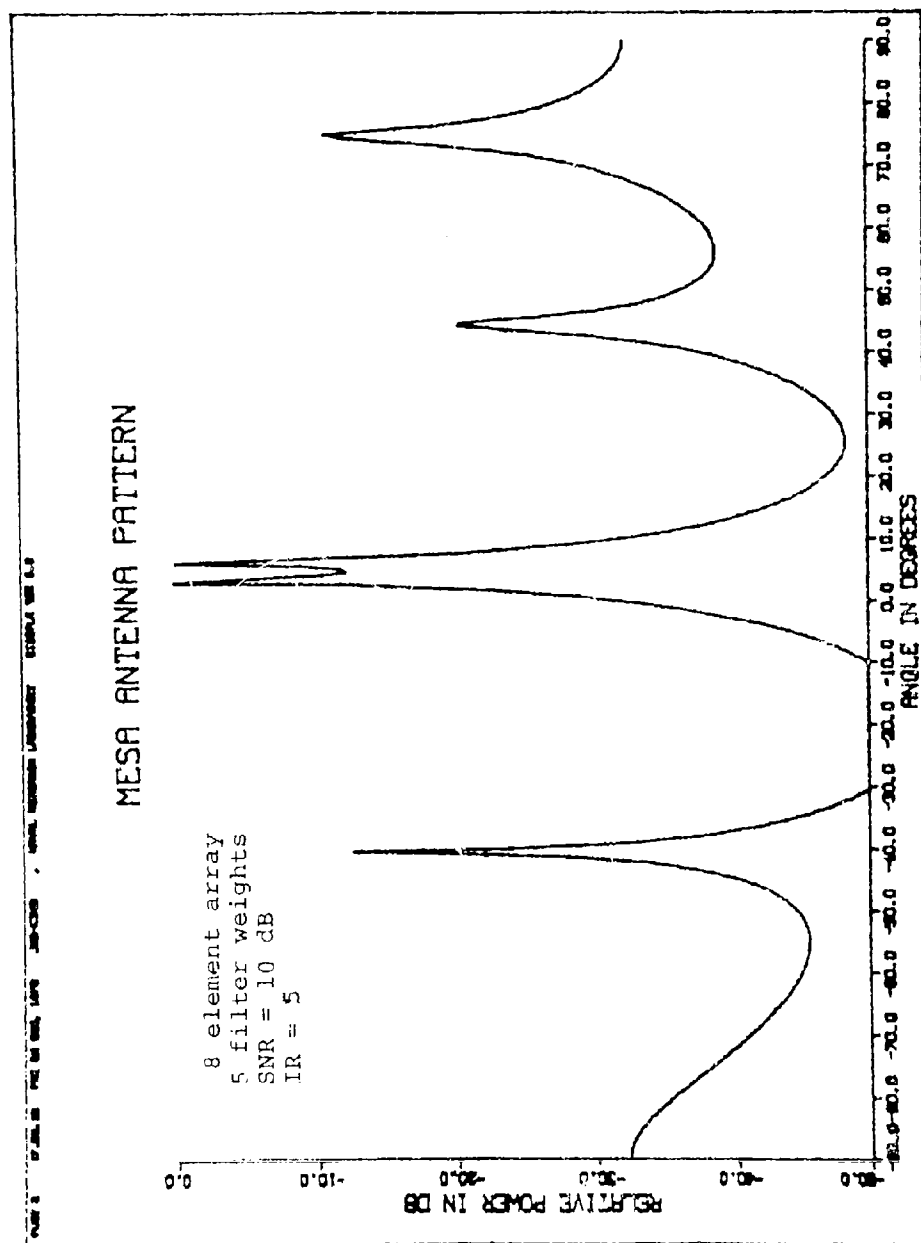


Fig. 3 - MESA snapshot, one signal

last filter weight is shown in Fig. 4 for one signal incident at +5 degrees and a SNR of 10 dB. Peak splitting is eliminated in the example of Fig. 4 with an average of only two filter weights ($L=2$) and utilizing a total of only 16 data points. The 16 data points include the same complex noise data set used in the example of Fig. 2 ($IR=5$). The signal is very prominent in the averaged MESA pattern of Fig. 4, although the signal peak is slightly displaced at an angle of +4.5 degrees denoting an inaccuracy of 0.5 degrees. Further averaging beyond $L=10$ provides little or no improvement. The averaged MESA antenna pattern for $L=10$, which is shown in Fig. 5, has nearly white noise. The noise peaks are very subdued and are almost eliminated, consequently very little improvement is possible. But the signal peak, which is considerably sharpened, remains at +4.5 degrees with an inaccuracy of 0.5 degrees.

Resolution capability is demonstrated by the averaged MESA antenna pattern of Fig. 6, where two signals with a SNR of 13 dB each signal, each element, are just resolved. Best resolution, which is depicted in Fig. 6, is achieved for $N=7$ and $L=20$. The two signals as detected in Fig. 6 are located closer together at angles of 0.5 and 4.5 degrees. The technique of averaging filter weights is a simple and fast stabilization technique which results in good resolution and detection capability for a relatively small number of repetitive calculations utilizing 160 ($L \cdot M$) data points.

B. Averaged Prediction Errors

An averaged MESA antenna pattern may also be computed by averaging the forward and backward prediction errors as defined by eqns. (5) and (6). Prediction errors for filter sizes 1 - N are all calculated in the Burg technique, however best results are achieved by averaging only the set of prediction errors for the specified filter size N as follows:

$$F_n^N = \frac{1}{L} \sum_{k=1}^L \left[F_n^N(k\Delta t) \right]_k \quad \text{for } (N \leq n \leq M)$$

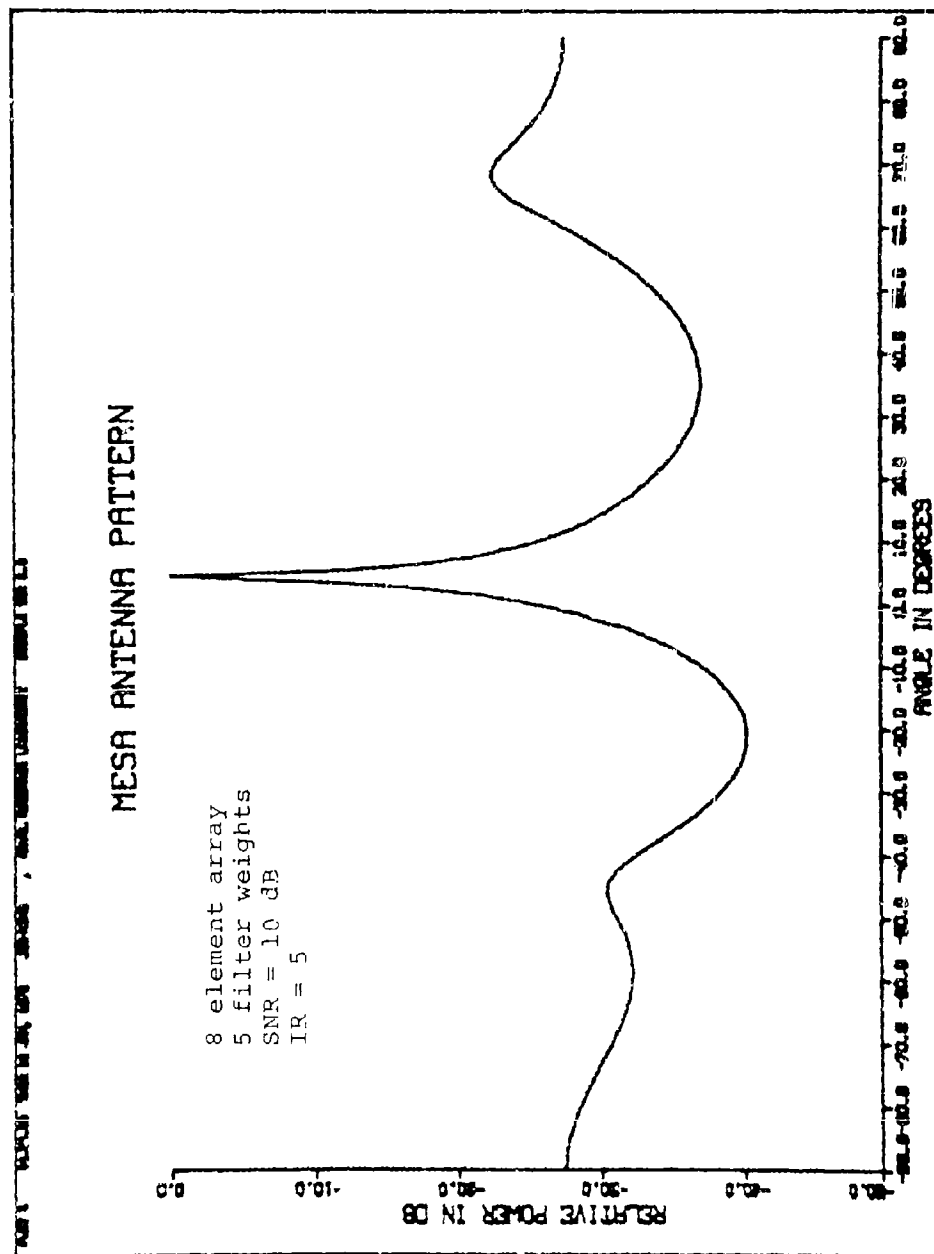


Fig. 4 - One signal, averaged filter weights, $L=2$

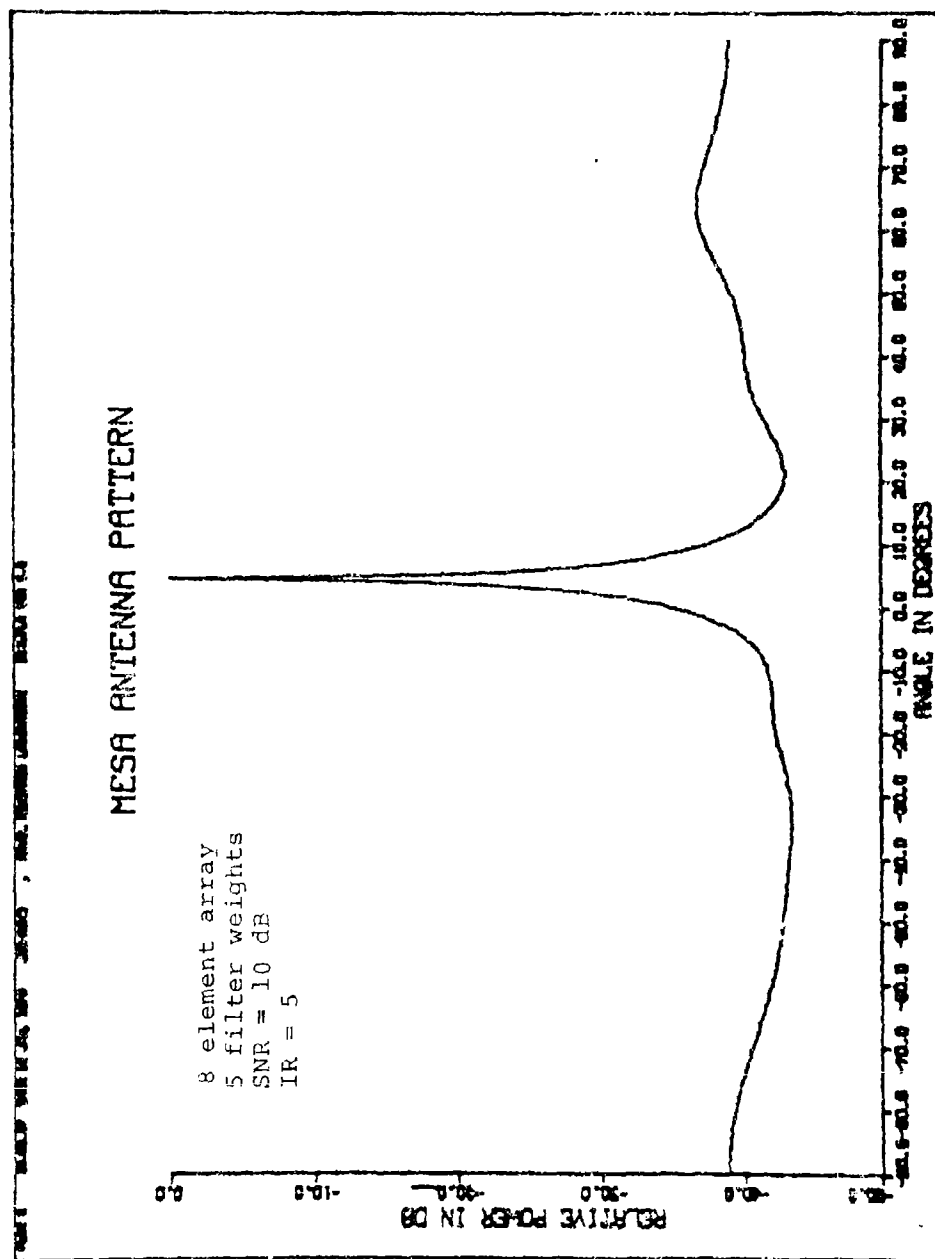


Fig. 5 - One signal, averaged filter weights, L=10

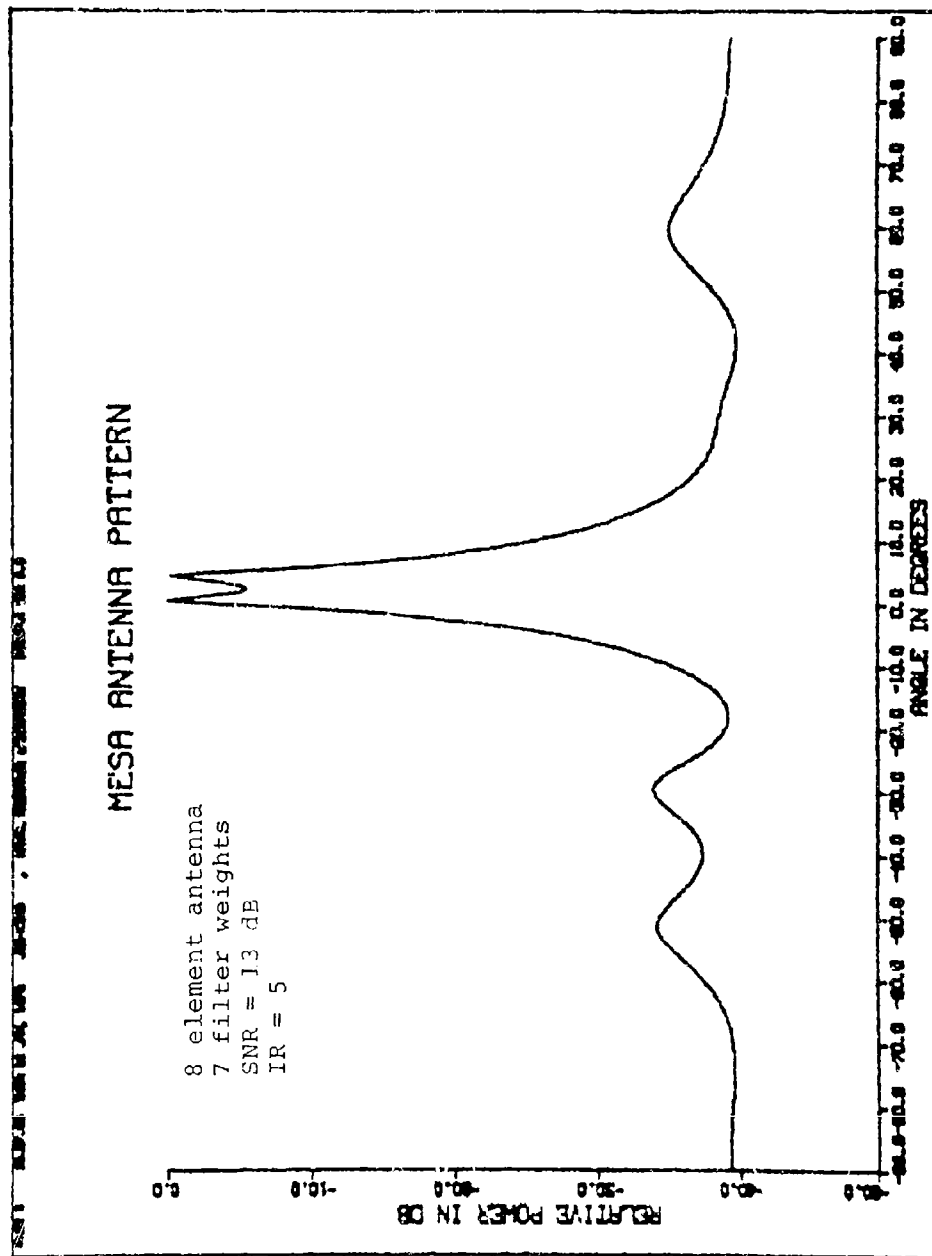


Fig. 6 - Two signals, averaged filter weights, $L=20$

$$B_n^N = \frac{1}{L} \sum_{k=1}^L \left[B_n^N(k\Delta t) \right]_k \quad \text{for } (1 \leq n \leq M-N)$$

Both prediction error averaging and filter weight averaging are comparatively simple and fast averaging techniques, but the two averaged antenna patterns are quite dissimilar.

An averaged MESA antenna pattern computed by averaging the prediction errors is shown in Fig. 7 where the split peak (obtained for $L=1$, Fig. 3) is eliminated by averaging with only one additional data set ($L=2$). The result of further averaging is shown for $L=10$ in Fig. 8. The filter size ($N=5$) and the complex data set for $IR=5$ are the same as used in all previous examples of averaged MESA patterns. It is evident by observation of Figs. 7 and 8 that averaging of prediction errors does not whiten the noise and does not enhance the SNR, but peak splitting is eliminated. In Fig. 8 the signal peak is located at +4 degrees for an error of one degree. Further averaging beyond $L=10$ does not improve the antenna pattern for one signal and an 8 element array.

Prediction errors are averaged in Fig. 9 for two signals incident at 0 and +6 degrees. The two signals are well resolved and the SNR is improved for $L=30$. One signal is accurately located at 0 degrees, while the second signal which is located at +4.5 degrees is in error by 1.5 degrees. The SNR is significantly improved, more so than for the single signal of Figs. 7 and 8.

C. Averaged Covariance Matrix

While not so obvious, the equations of the Burg technique do contain elements of the covariance matrix. These elements may be averaged and incorporated into the Burg technique equations without altering the utilization or the characteristics of the Burg technique. The only independent filter weight \hat{r}_{N+1}^{N+1} , which is defined by eqn. (4) of the Burg technique, is a function of the forward and backward prediction errors, F_{N+1}^N and B_I^N .

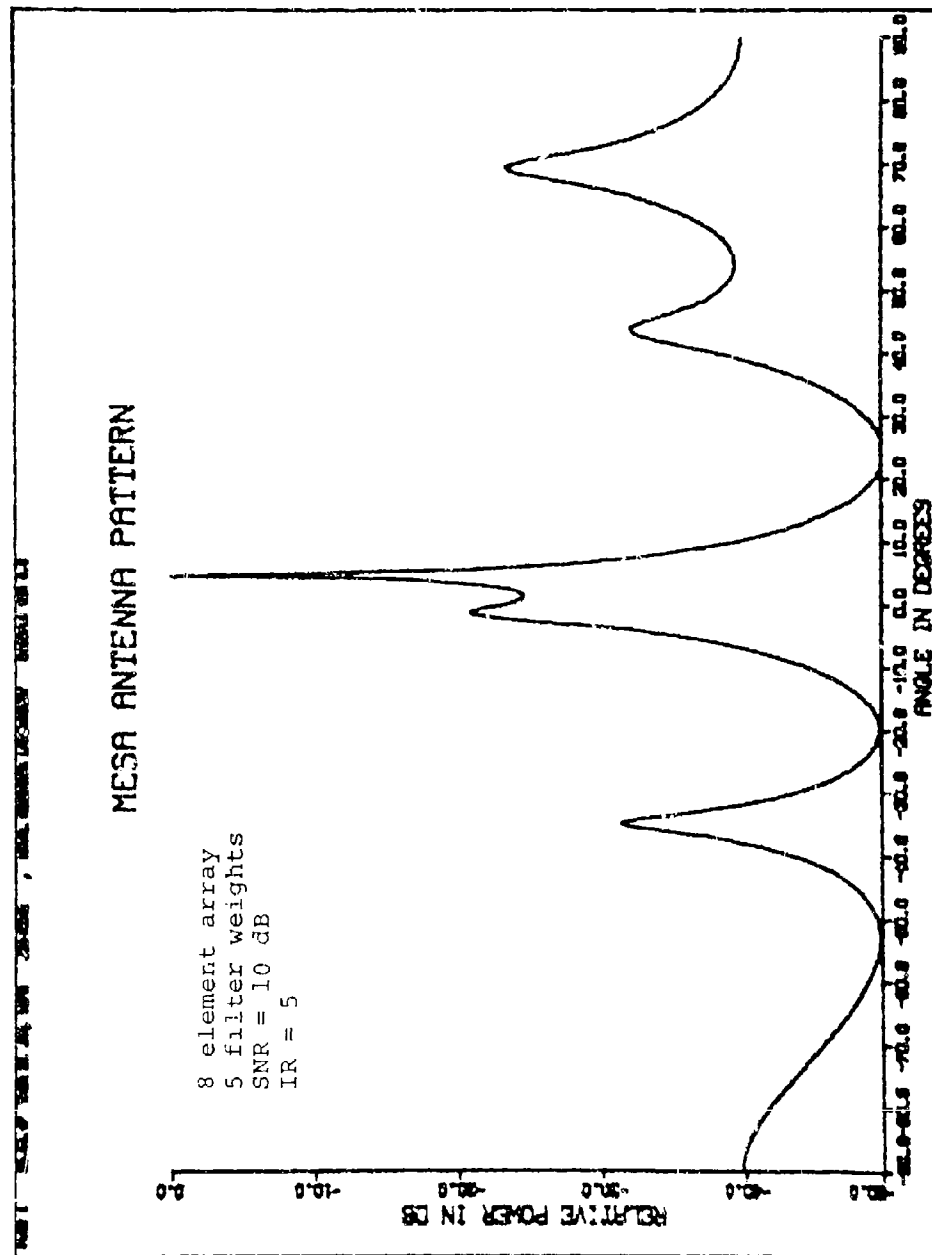


Fig. 7 - One signal, averaged prediction errors, $L=2$

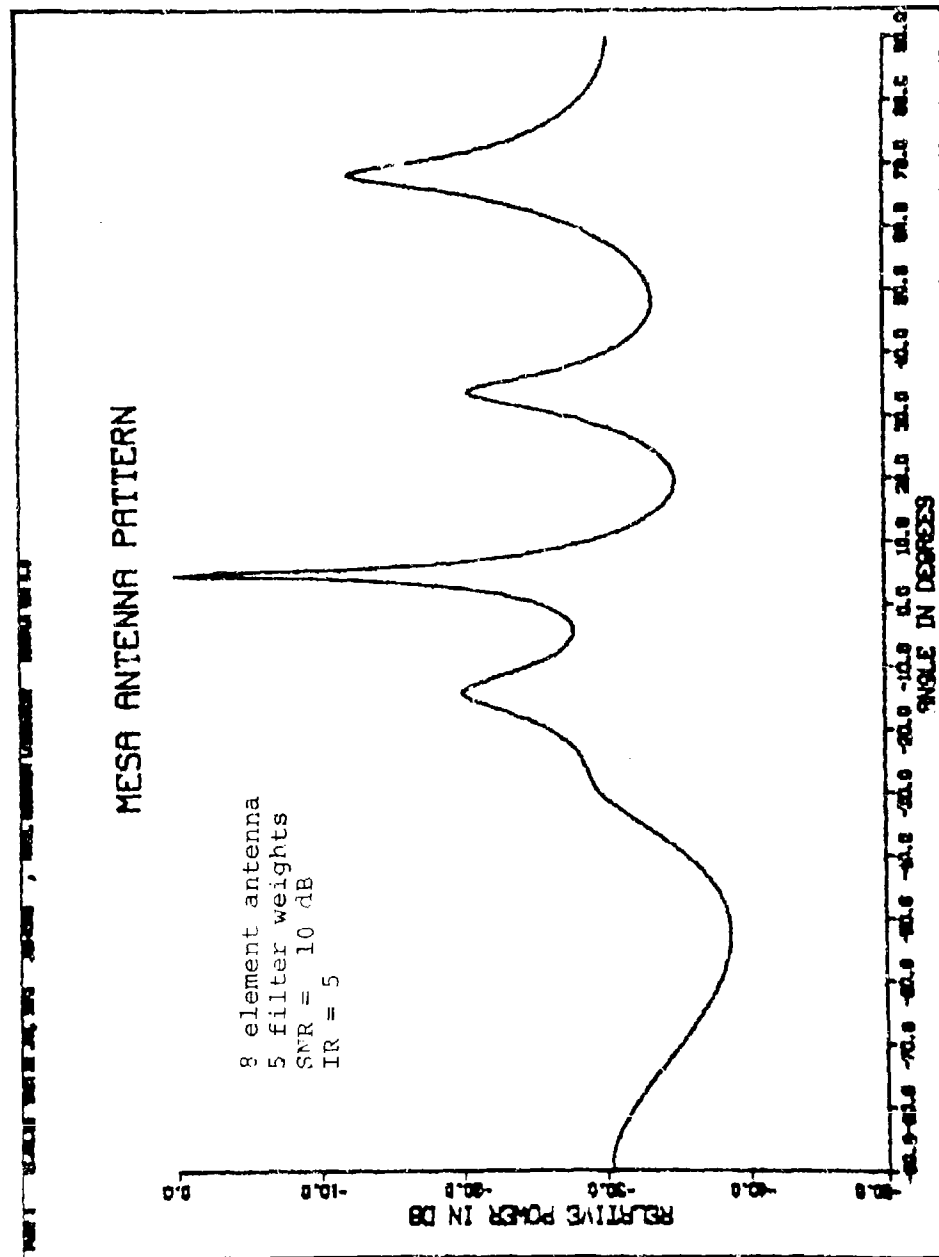


Fig. 8 - One signal, averaged prediction errors, $L=10$

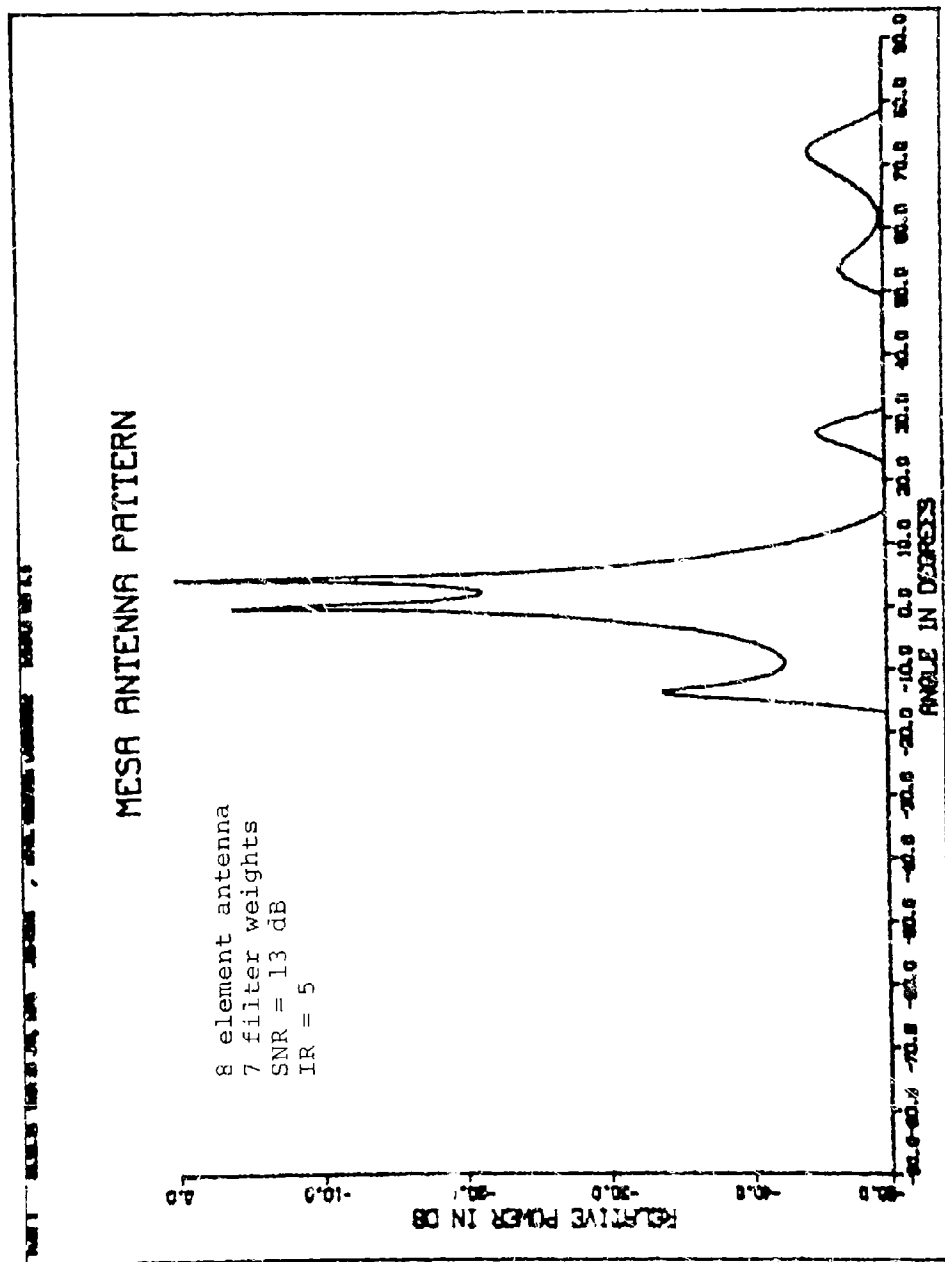


Fig. 9 - Two signal, averaged prediction errors, $L=30$

Products of the prediction errors may be considered as functions of the covariance matrix elements by considering the original definition as follows:

Forward prediction error

$$F_{N+I}^N = \sum_{n=1}^N \gamma_n^N X_{n+I-n+1} \quad (7)$$

Backward prediction error

$$B_I^N = \sum_{n=1}^N (\gamma_n^N)^* X_{I+n-1} \quad (8)$$

where $\gamma_1^N = 1.0$

The last filter weight γ_{N+1}^{N+1} of eqn. (4) may be expressed as the ratio of two functions, TOP and BOTM, as follows:

$$\gamma_{N+1}^{N+1} = -2 \text{ TOP/BOTM}$$

where

$$\text{TOP} = \sum_{I=1}^{M-N} F_{N+I}^N (B_I^N)^* \quad (9)$$

$$\text{BOTM} = \sum_{I=1}^{M-N} \left[(F_{N+I}^N)^2 + (B_I^N)^2 \right] \quad (10)$$

Insertion of the prediction error definitions eqns. (7) and (8) into eqns. (9) and (10) and re-ordering the summations yields the desired functional form as follows:

$$\text{TOP} = \sum_{I=1}^{M-N} \left[\sum_{M=1}^N \gamma_M^N X_{N+I-M+1} \sum_{n=1}^N \left((\gamma_n^N)^* X_{1+n-1} \right)^* \right]$$

$$TOP = \sum_{m=1}^N \sum_{n=1}^N \gamma_m^N \gamma_n^N r(N-M-n+2)$$

where

$$r(N-m-n+2) = \sum_{I=1}^{M-N} X_{I+N-m+1} X_{I+n-1}^* \quad (11)$$

$$BOTM = \sum_{I=1}^{M-N} \left[\sum_{m=1}^N \gamma_m^N X_{I+N-m+1} \sum_{n=1}^N (\gamma_n^N)^* X_{N+I-n+1}^* + \sum_{m=1}^N (\gamma_m^N)^* X_{N+m-1} \sum_{n=1}^N \left((\gamma_n^N)^* X_{I+n-1} \right)^* \right]$$

$$BOTM = \sum_{m=1}^N \sum_{n=1}^N \gamma_m^N (\gamma_n^N)^* r(n-m) + \sum_{m=1}^N \sum_{n=1}^N (\gamma_m^N)^* \gamma_n^N r(m-n)$$

where

$$r(n-m) = \sum_{I=1}^{M-N} X_{N+I-m+1} X_{N+I-n+1}^* \quad (12)$$

$$r(m-n) = \sum_{I=1}^{M-N} X_{I+m-1} X_{I+n-1}^* \quad (13)$$

It is apparent that the autocorrelation coefficients defined by eqns. (11), (12) and (13) may be averaged as follows:

$$\bar{r}(N-m-n+2) = \sum_{I=1}^{M-N} \frac{1}{L} \sum_{k=1}^L X(k\Delta t)_{N+I-m+1} X(k\Delta t)_{I+n-1}^* \quad (14)$$

$$\bar{r}(m-n) = \sum_{I=1}^{M-N} \frac{1}{L} \sum_{k=1}^L X(k\Delta t) X^*(k\Delta t) \quad (15)$$

$$\bar{r}(m-n) = \sum_{I=1}^{M-N} \frac{1}{L} \sum_{k=1}^L X(k\Delta t) X^*(k\Delta t) \quad (16)$$

The autocorrelation coefficients (eqns. (11), (12) and (13)) are elements of the covariance matrix for the data set X_1, X_2, \dots, X_M . The averaged covariance matrix elements given by eqns (14), (15) and (16) may be utilized to compute the last filter weight Γ_{N+1}^{N+1} and an averaged MESA antenna pattern.

The results due to averaging of the covariance matrix are observed in Fig. 10 where the split peak shown in Fig. 3 is eliminated with only one additional data set ($L=2$). Also the noise is considerably whiter which greatly improves the SNR. Further averaging provides little additional improvement as noted by Fig. 11, where for $L=10$ the noise appears slightly whiter and the SNR is slightly enhanced over the results shown in Fig. 10.

Two signals located at 0 and +6 degrees are well resolved in Fig. 12 with covariance matrix averaging, for $L=10$ and an input SNR of 13 dB each signal. The background noise is substantially reduced although it is not as white as the noise that appears in Fig. 11. Averaging of the covariance matrix elements is, as demonstrated, an excellent averaging and stabilization technique.

D. Averaged MESA Snapshots

Individual MESA antenna patterns, which are referred to as "snapshots" (e.g. Fig. 1a, 1b), may be averaged in order to obtain a stable antenna pattern. This method has been utilized (14) successfully using optimal filter sizes. However, if the optimal filter size cannot be determined, a fixed filter size may be selected

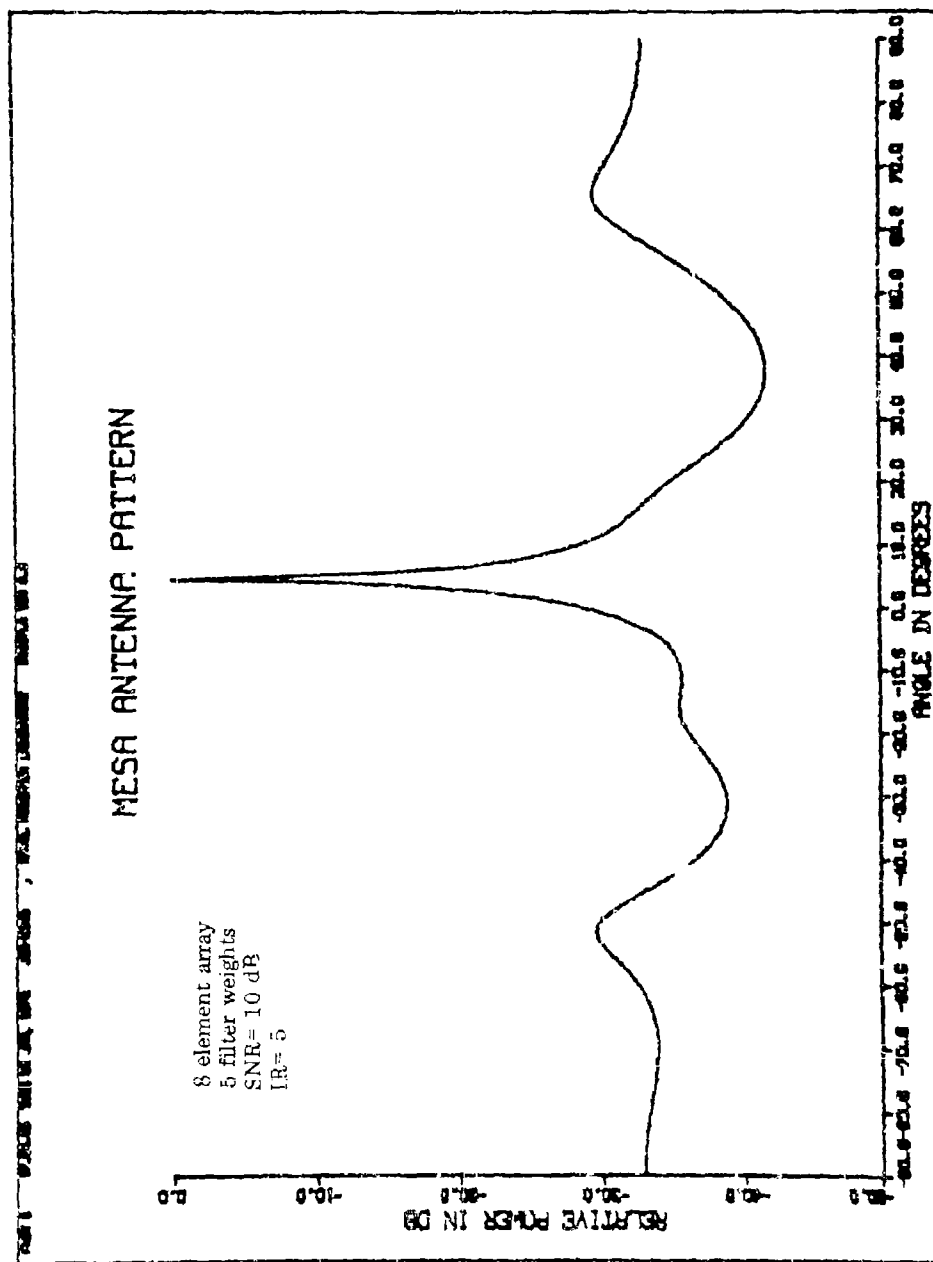


Fig. 10 - One signal, averaged covariance matrix, $L=2$

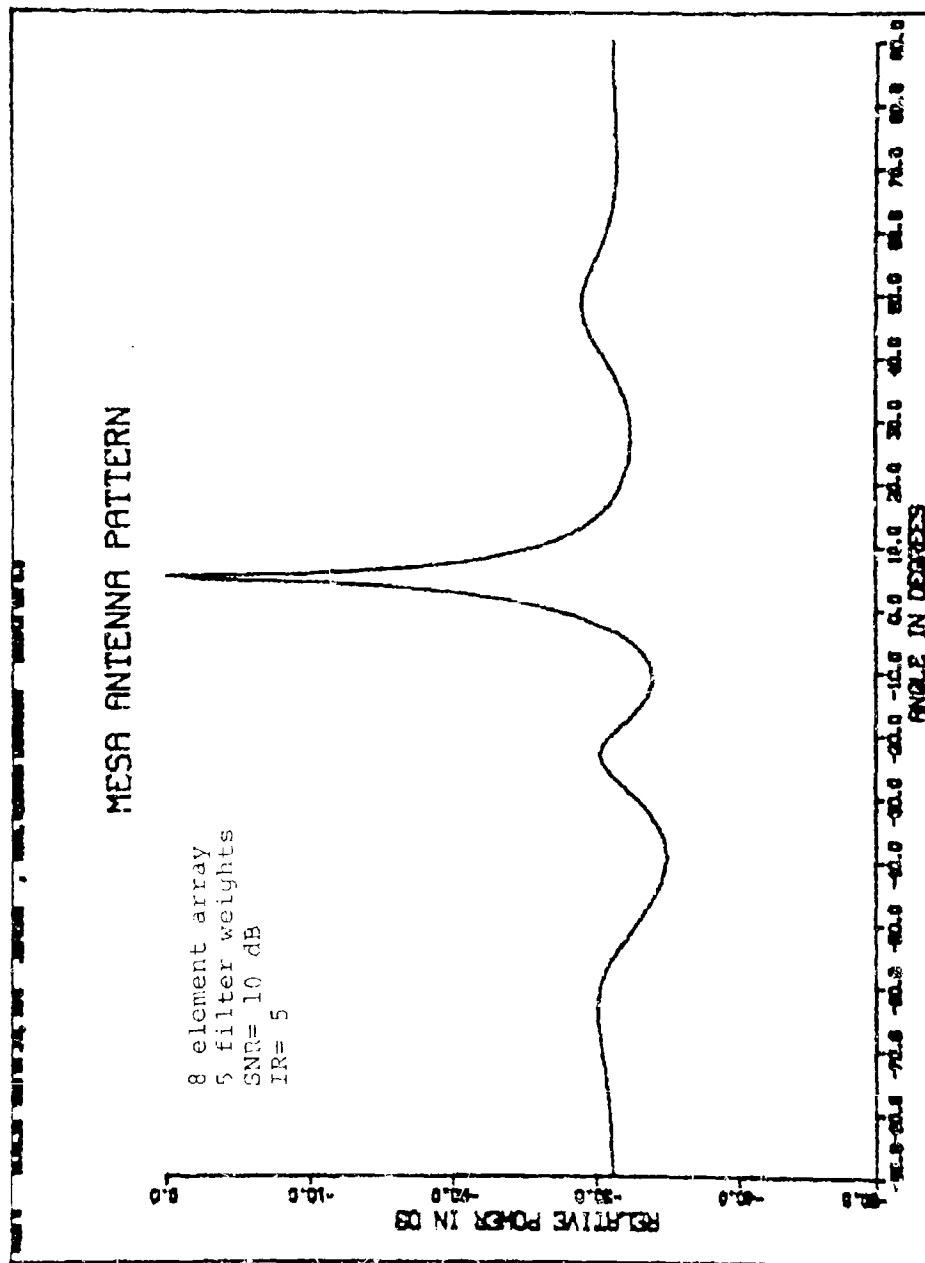


Fig. 11 - One signal, averaged prediction errors, $L=10$

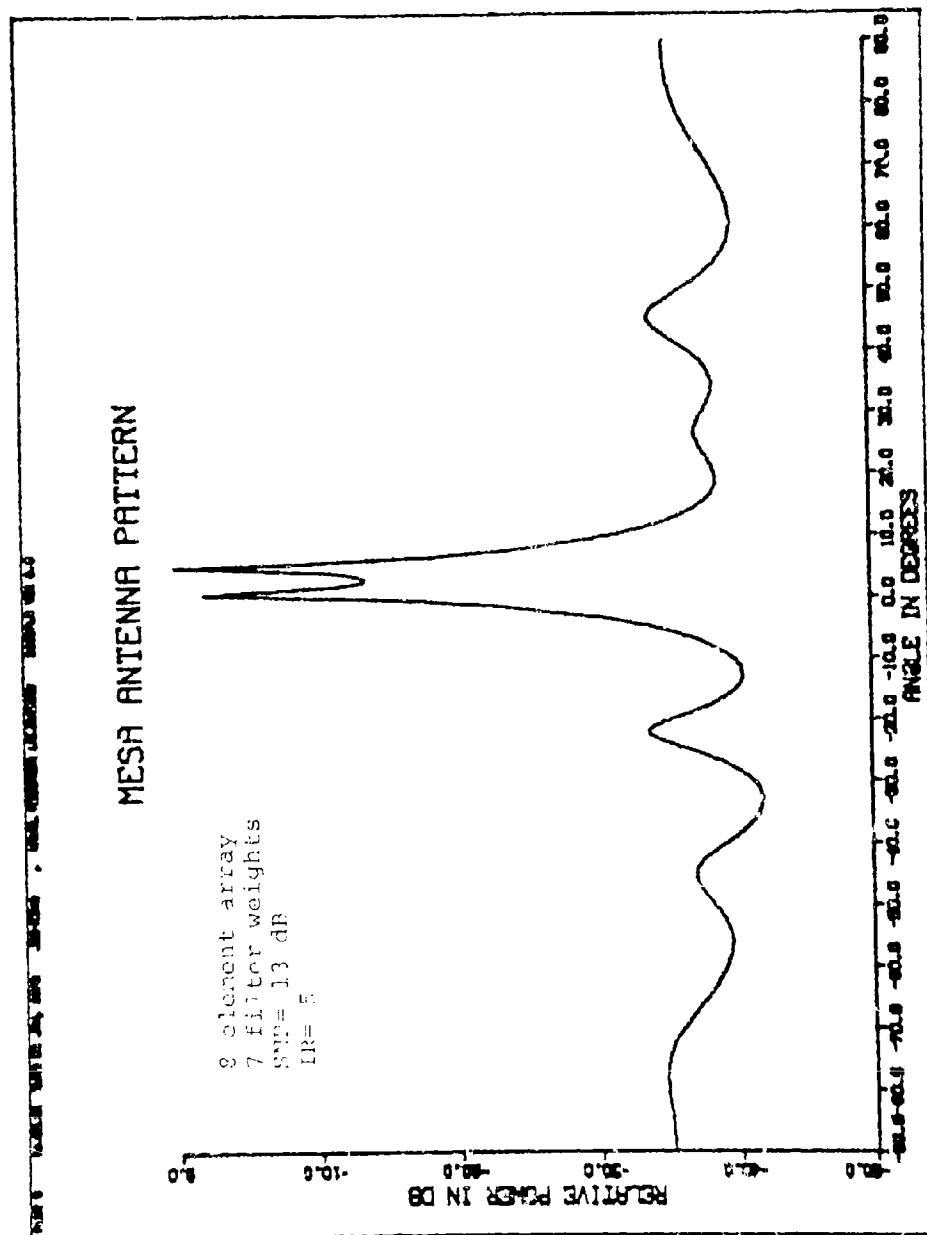


Fig. 12 - Two signal, averaged prediction errors, $L=10$

for computing all the individual MESA snapshot antenna patterns. The best resolution is always achieved using the largest possible filter size ($N=M-1$). However, the larger filter sizes are also the most unstable. Consequently, while an average of many MESA snapshots improves stability, the resultant stable pattern may not be a very accurate antenna pattern.

Averaging results for two filter sizes ($N=5$ and $N=7$) are demonstrated in the three following examples. A simple average of two MESA snapshots ($L=2$) is shown in Fig. 13 for one signal incident at 5 degrees with a SNR of 10 dB. The split peak that occurs for $L=1$ (Fig. 3) is still present in the average of two snapshots. However, there is improvement in the SNR. There are of course twice the number of peaks (10) as expected for two MESA snapshots having five filter weights ($N=5$) each. The consequence of further averaging is demonstrated in Fig. 14 where 30 antenna patterns (computed for a signal incident at 5 degrees with a SNR of 10 dB) are averaged. There is further improvement in the signal peak definition and accuracy; the signal is located at +4 degrees, for an error of one degree. The SNR is improved substantially.

In Fig. 15 the resultant average of MESA antenna patterns for two signals incident at 0 and +6 degrees is disappointing as the two signal peaks are not very well defined. Instead there are four strong peaks, two of which are in error. There is of course improvement in the SNR, but the resolution characteristics are very poor. In the example of Fig. 15, averaged MESA snapshots all have the maximum number (7) of filter weights. Better results have been achieved (14) using an optimal filter size, however the optimal filter size can only be computed if the incident signal angles are known.

VI. ADAPTIVE FILTER WEIGHTS

While the MESA technique is inherently adaptive, other adaptive methods which have been demonstrated (17, 18) have simple procedures for updating the filter weights. One such procedure (12)

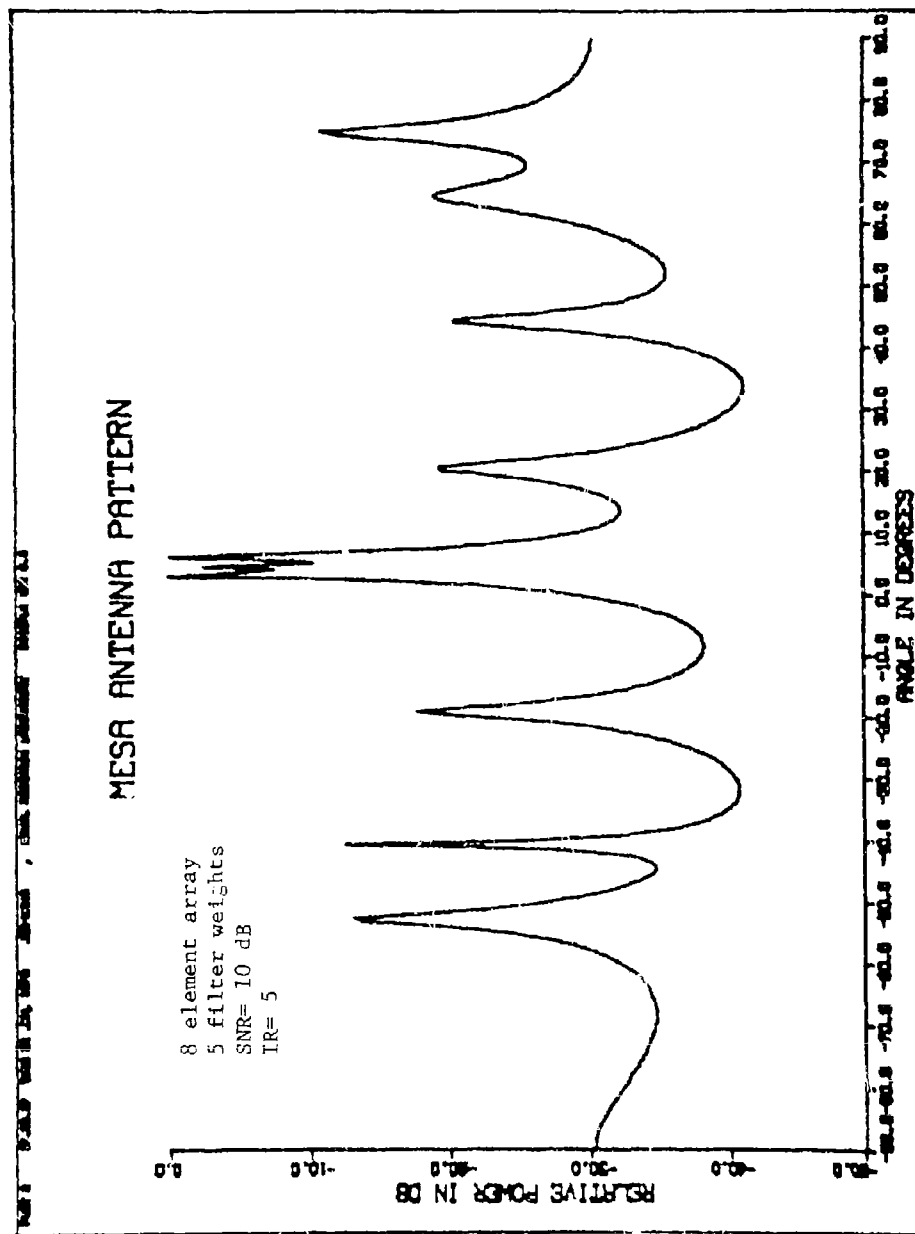


Fig. 13 - One signal, averaged patterns, L=2

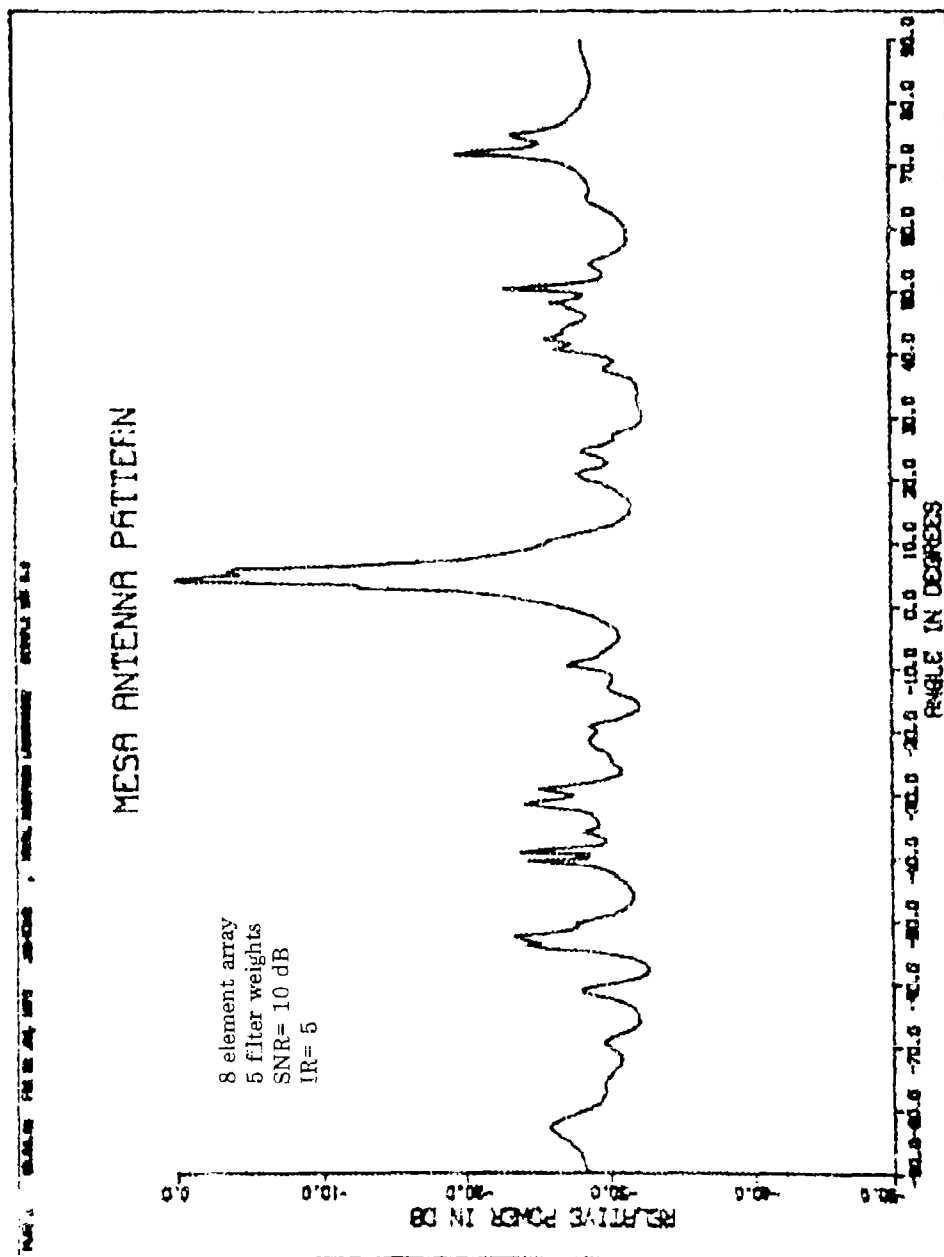


Fig. 14 - One signal, averaged patterns, L=30

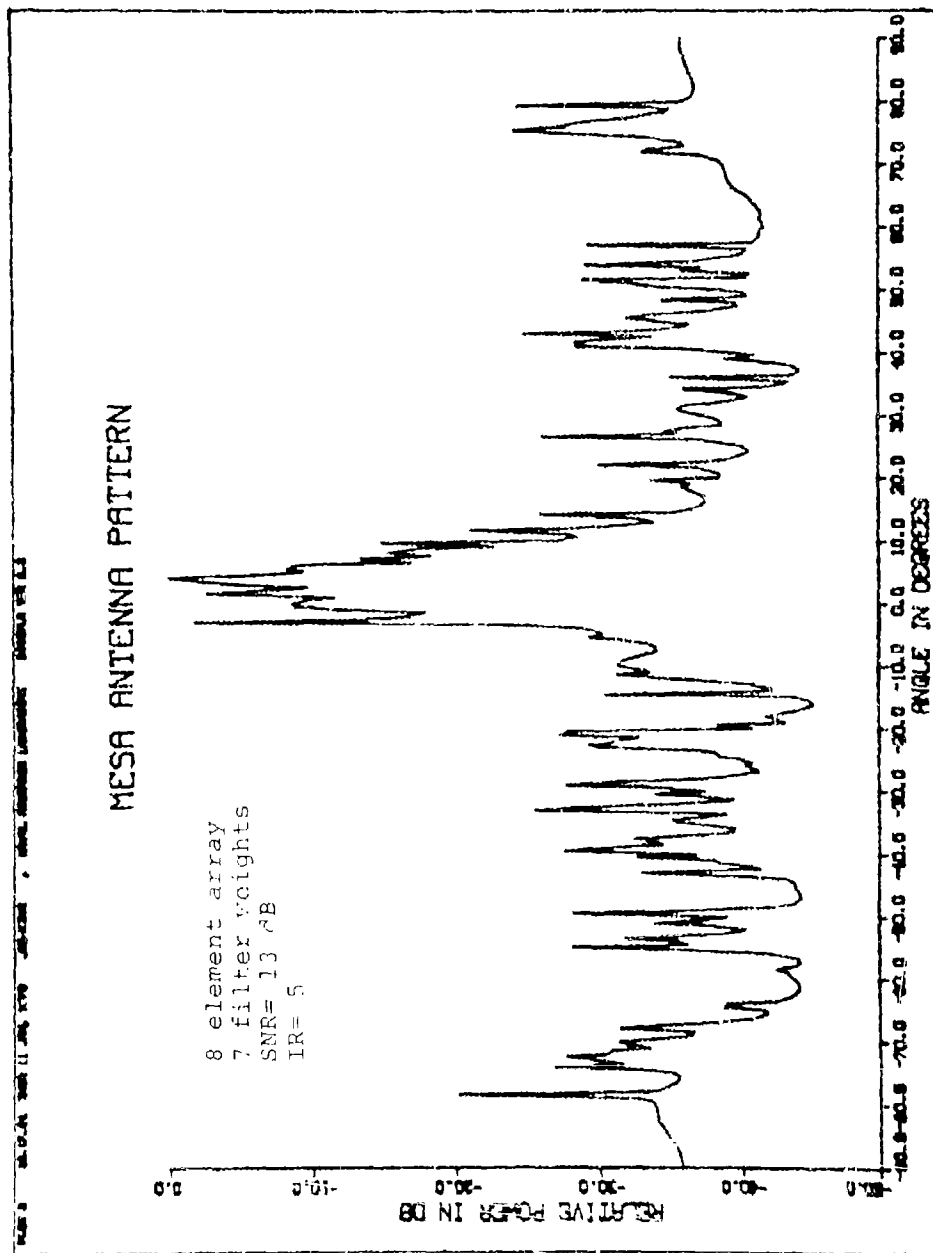


Fig. 15 - Two signal, averaged patterns, $L=30$

increases the filter weights in proportion to the correlation of the prediction error with the data set. For example, a filter weight $W(k)$ computed at time $k\Delta t$ may be updated at a later time $(k+1)\Delta t$ to give $W(k+1)$ as follows:

$$W(k+1) = W(k) + \mu \sum_{n=1}^M e_n(k) X_n^*(k) \quad (17)$$

where the correlation is taken over all computed prediction errors $e_n(k)$. The prediction errors are defined as follows:

$$e_n(k) = X_n(k) - \hat{X}_n(k) \quad (18)$$

for data samples $X_n(k)$ and predicted values $\hat{X}_n(k)$. The proportionality constant is denoted by the convergence parameter μ .

In order to incorporate this procedure into the MESA technique, a first set of filter weights is computed in the usual manner as defined by eqns. (3) and (4). Subsequent filter weights $\Gamma_n^N(k+1)$ may then be computed according to eqn. (17) as follows:

$$\Gamma_n^N(k+1) = \Gamma_n^N(k) + \mu \sum_{n=1}^{M-N} e_n^N(k) X_n^*(k) \quad (19)$$

where the prediction error is actually the sum of the forward and backward prediction errors over all possible $(M-N)$ errors as follows:

$$e_n^N(k) = F_{n+N}^N(k) + B_n^N(k) \quad (20)$$

However, with use of the Burg technique, only the last filter weight Γ_N^N , need be computed with eqn. (19), since all other filter weights

($n < N$) are dependent upon r_N^N according to eqn. (3).

As the prediction error is whitened, the additive adaptive component is reduced, since the correlation of a whiter prediction error with the data set is smaller. Consequently, the adaptive filter weights may converge to become a whitening filter.

The result of updating MESA filter weights is illustrated in Fig. 16 where an "adapted" MESA antenna pattern is shown for one signal incident at +5 degrees, SNR=10 dB, and $L=2$. The "adapted" pattern for $L=2$ is of course quite similar to the computed MESA snapshot ($L=1$) shown in Fig. 3, since the filter weights have been modified only once. The split peak is still present for $L=2$ in Fig. 16, but with further adaption the split peak is eliminated as shown in Fig. 17 for $L=10$. However, the SNR is not improved, although three noise peaks have been reduced. As observed in Fig. 17 the noise has remained peaked even after ten adaptations. Obviously the adaption method does not tend to whiten the noise, and consequently the results are most disappointing.

In another application of the adaptive method, two signals incident at 0 and +6 degrees are resolved in ten adaptations ($L=10$) as shown in Fig. 18, where the SNR is 13 dB for each signal. One signal is located accurately at +6 degrees while the other signal is located at +1.5 degrees with an error of 1.5 degrees. The SNR is improved with respect to the original ($L=1$) MESA snapshot of Fig. 3. However, the noise is not whitened in the adaptive process as had been anticipated.

The results from using adaptive filter weights with MESA are very disappointing, and in addition the value of a convergence parameter must be specified. In the three preceding examples of the adaptive technique the value of the convergence parameter μ is quite critical. If μ is too small, there is little improvement in the computed antenna pattern, and if μ is too large, there may be considerable distortion of the signal peak.

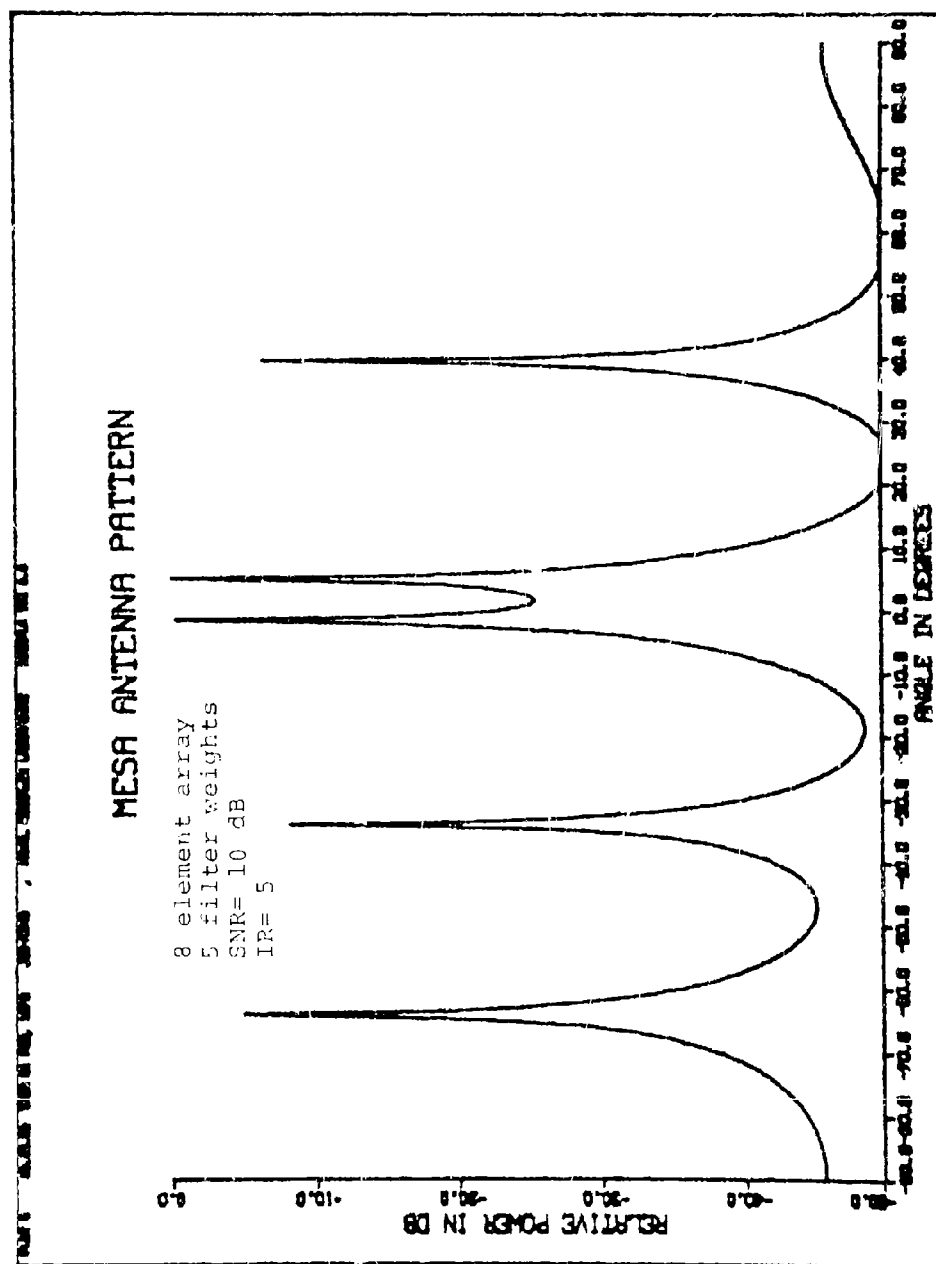


Fig. 16 - One signal, adaptive filter weights, $L=2$

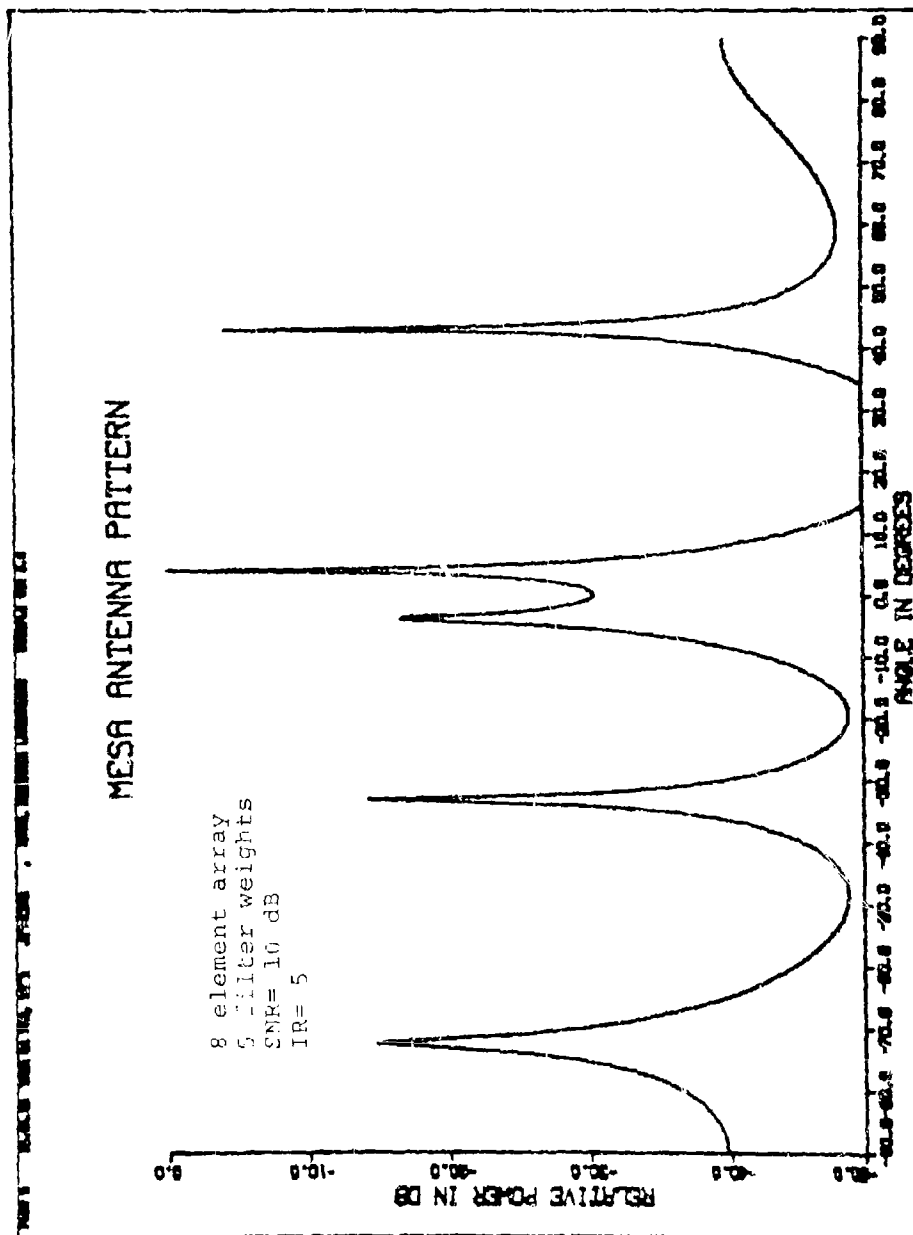


Fig. 17 - One signal, adaptive filter weights $L=10$

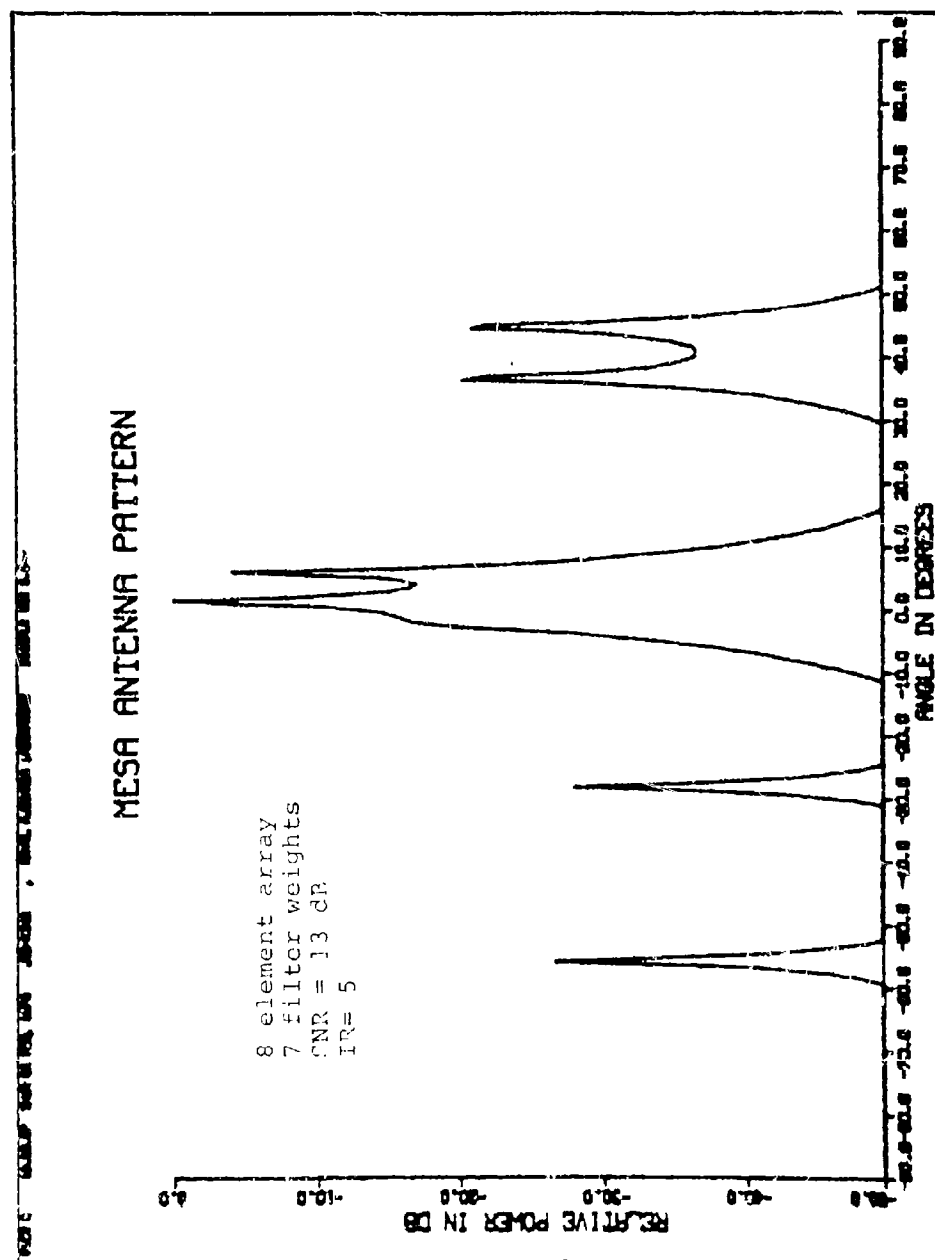


Fig. 18 - Two signals, adaptive filter weights, L=10

VII. RESOLUTION

Of the five stabilization methods examined, only two appear to preserve and enhance the desirable MESA characteristic of whitening the noise. The resolution capability of both whitening, stabilization methods is demonstrated in one example of two signals separated by four degrees, at -2 and $+2$ degrees, with equal SNR values of 20 dB each antenna element.

A stabilized antenna pattern computed by averaging the covariance matrix is shown in Fig. 19, where the two signals are not resolved, but only one signal peak is detected at $+0.5$ degrees. However both signals are identified in Fig. 20, where the antenna pattern is computed by averaging the filter weights using a short average of $L=5$. The same short average is used in computing both antenna patterns in Figs. 19 and 20 since further averaging, which does appear to improve signal detection, only serves to reduce the resolution capability. However, some averaging is necessary in order to obtain a stable, reliable antenna pattern. The noise is whiter in Fig. 19, but the resolution is best in Fig. 20. While the two characteristics appear to be somewhat incompatible, it is necessary that good resolution be achieved with stable, reliable antenna patterns.

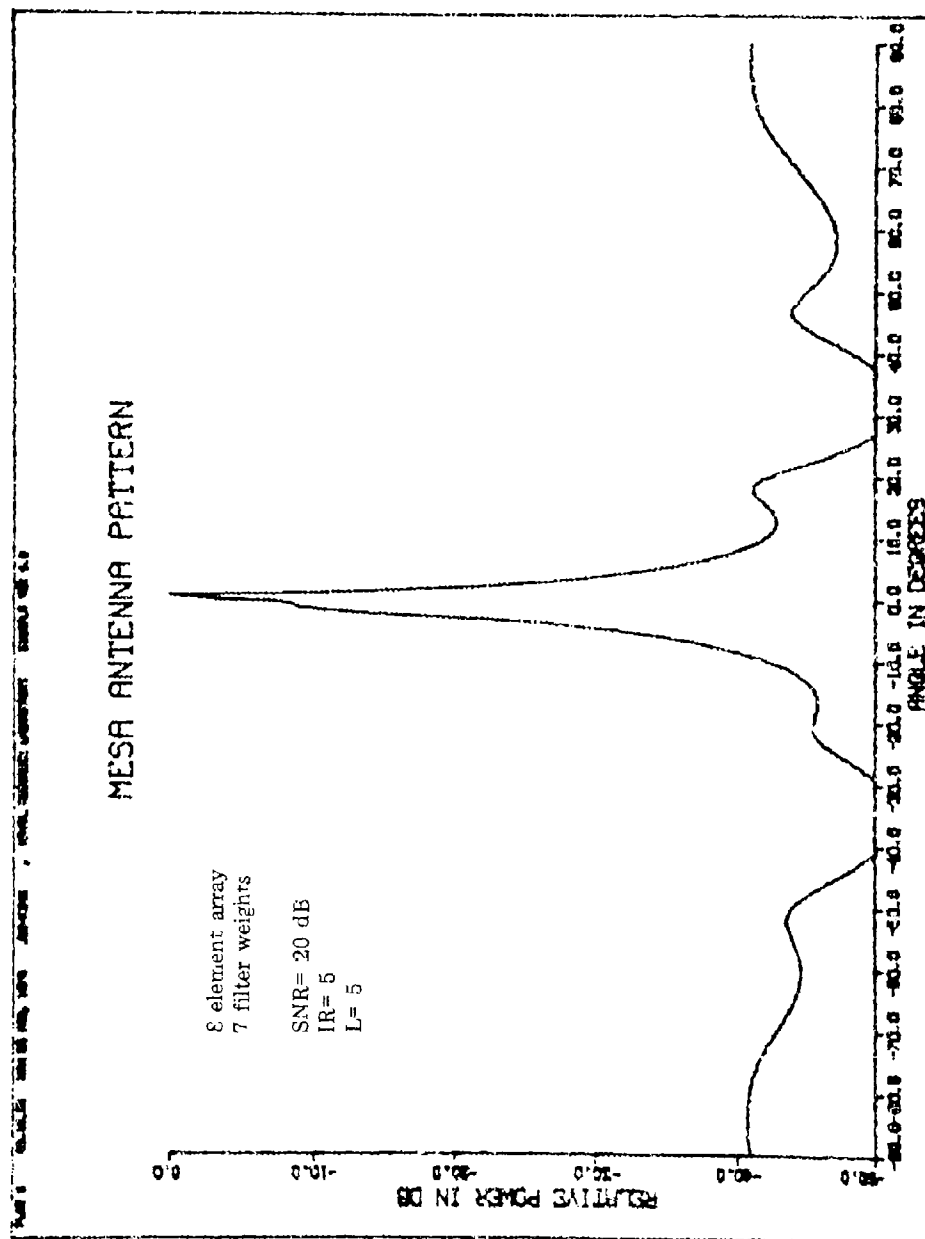


Fig. 19 - Two unresolved signals, averaged covariance matrix

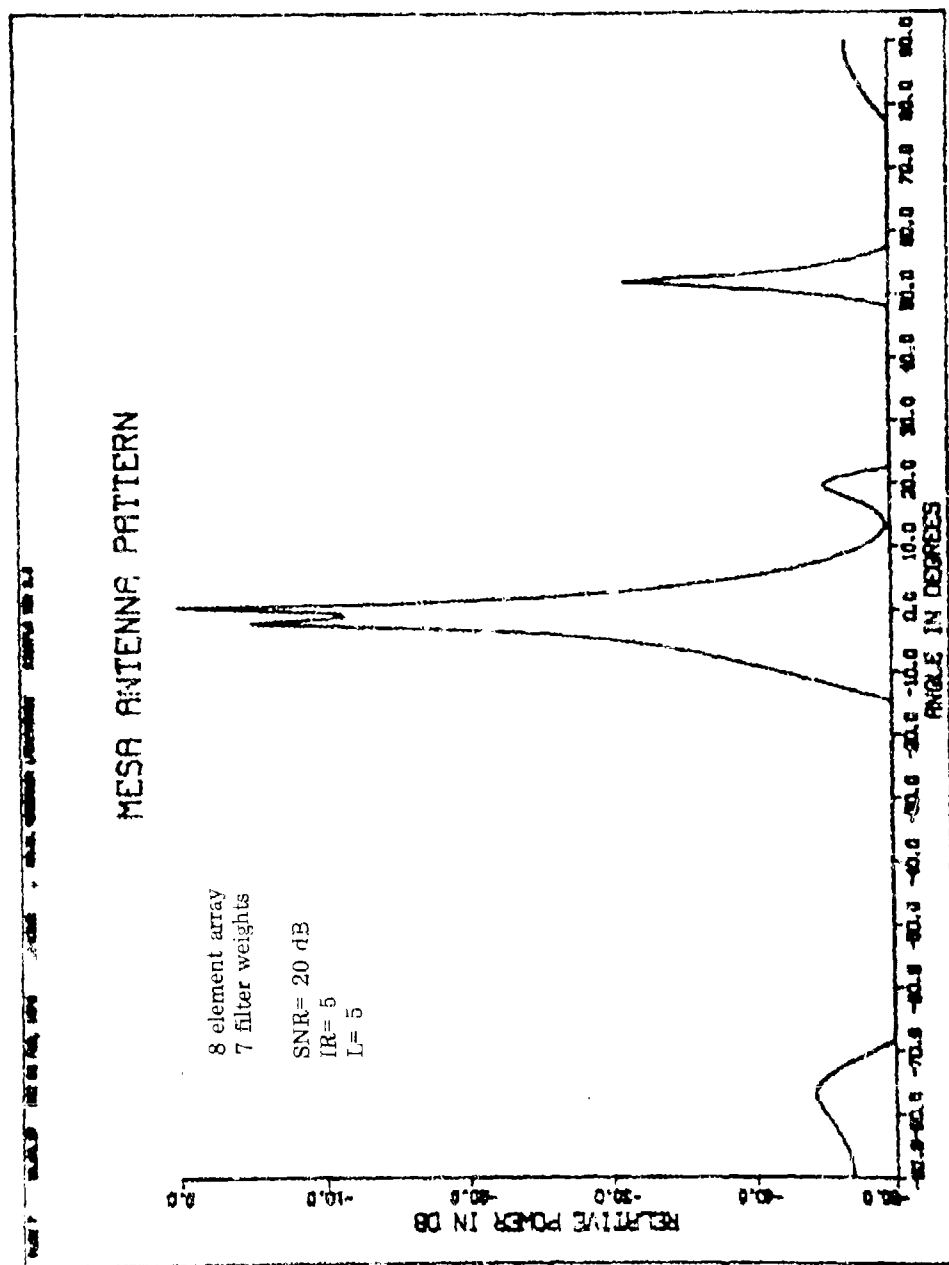


Fig. 20 - Two resolved signals, averaged filter weights

VIII. CONCLUSIONS

Split signal peaks, which are a common occurrence in MESA snapshot patterns, are shown to be a consequence of noise interference. Such noise interference is virtually eliminated with use of the proposed stabilization methods.

Of the five stabilization techniques examined, two have excellent characteristics, one other is only somewhat satisfactory, and two were very disappointing. An average of filter weights and an average of the covariance matrix are both very useful stabilization methods. Both methods serve to whiten the noise and greatly improve the SNR. In addition, split signal peaks were not observed with use of either averaged filter weights or averaged covariance matrix elements. Further testing of these two averaging methods is clearly justified. Hopefully, resolution and SNR properties of these two excellent averaging and stabilization techniques will be specifically determined in future research efforts.

It is doubtful that any of the other three examined stabilization methods are worthy of further consideration. Neither the averaged prediction errors nor the adaptive filter weights served to whiten the noise, and the averaged MESA patterns proved to be most unstable.

In the one example of two signals separated four degrees the MESA antenna pattern computed by averaging filter weights provided the best signal resolution. However, many such examples need to be accumulated in order to determine the resolution characteristics of the recommended MESA stabilization methods.

REFERENCES

1. Burg, John P., (1975), "Maximum Entropy Spectral Analysis", Ph.D. Thesis, Stanford Univ., #75-25,499 Univ. Microfilms Intl., Ann Arbor, Mich.
2. Parzen, E., (1969), "Multiple Time Series Modeling", in Multivariate Analysis - II, edited by P. R. Kirshnaiah, pp. 389 - 409, Academic Press, New York
3. Box, G. E., and Jenkins, G. M., (1970), Time Series Analysis Forecasting and Control, Holden-Day, San Francisco, Calif.
4. Yule, G. U., (1927), "On a Method of Investigating Periodicities in Distrubed Series with Special References to Wolfers Sunspot Numbers", Phil. Trans. Roy. Soc. London, Ser. A, Vol. 226, pp. 267-298
5. Fisher, R. A. (1912), "On an Absolute Criterion for Fitting Frequency Curves", Messenger of Math, Vol. 41, p. 155
6. Makhoul, John (1975), "Linear Prediction: A Tutorial Review", Proc. IEEE, Vol. 63, No. 4, pp. 561 - 580, (April, 1975)
7. Nuttall, Albert H., (1976), "Spectral Analysis of a Univariate Process with Bad Data Points, Via Maximum Entropy and Linear Predictive Techniques", NUSC Tech. Rept. 5303, Naval Underwater Systems Center, New London, Conn.
8. Lacoss, R. T. (1971), "Data Adaptive Spectral Analysis Methods", Geophysics, Vol. 36. No. 4 (Aug. 1971), pp. 661 - 675
9. Gerchberg, R. W. (1974), "Super-resolution through Error Energy Reduction", Optica Acta, Vol. 21, No. 9 pp. 709-720 (1974).
10. Papoulis, Sept., (1975), "A New Algorithm in Spectral Analysis and Band Limited Extrapolation", IEEE Trans. on Circuits and Systems, CAS-22, No. 9, pp. 735-742 (1975)
11. Cadzow, James A., (1978, "Improved Spectral Estimation from Incomplete Sampled - Data Observations", RADC Spectrum Estimation Workshop, Griffiss Air Force Base, New York.

12. Widrow and Hoff, "Adaptive Switching Circuits", IRE 1960 WESCON Conv. Rec., Part 4, pp. 96 - 104.
13. Van den Bos, A. (1971) "Alternative Interpretation of Maximum Entropy Spectral Analysis", IEEE Trans. on Information Theory, IT-17, pp. 493 - 494.
14. King, W. R., (1979) "Maximum Entropy Wavenumber Analysis", submitted to NRL for publication, Jan. 1979. Naval Research Laboratory, Washington, D. C.
15. King, Swindell and O'Brien, (1974), "Final Report on Development of a Curvilinear Ray Theory Model and Maximum Entropy Spectral Analysis", Texas Instruments.
16. Fougere, Zawalick and Radoski, (1976), "Spontaneous Line Splitting in Maximum Entropy Power Spectrum Analysis", Physics of the Earth and Planetary Interiors, Vol. 12, pp. 201 - 207 (1976)
17. Griffiths, L. J. (1969), "A Simple Adaptive Algorithm for Real-Time Processing in Antenna Arrays", Proc. IEEE, Vol. 57, No. 10, pp. 1696 - 1704 (Oct. 1969).
18. Applebaum, S. P., (1966), "Adaptive Arrays", Syracuse Univ. Res. Corp., Rept. SPL TR 66-1, (Aug. 1966).

BROADBAND SIGNAL DETECTION WITH THE SCOT AND SCOT-PET

1.0 INTRODUCTION

1.1 Background

The crosscorrelation technique is useful for detecting broadband radar pulses. However, it is well known that the crosscorrelation technique is adversely affected by narrowband interference or narrowband signals transmitted by radar surveillance systems. Consequently, the crosscorrelation peak (due to the broadband signal) may be obscured by a sinusoidal modulation of the cross-correlation function caused by the presence of strong narrowband components.

Other signal processing techniques may not be so adversely affected by the presence of narrowband signal components. Carter, et al. (1) have provided one snapshot example, where a broadband signal in the presence of three narrowband signals is not detected by the crosscorrelation function, but is readily detected with the smoothed coherence transform (SCOT).

The SCOT is the Fourier transform of a cross-power spectral function, which has a frequency dependent normalization. The normalization serves to whiten the crosspower spectra and thereby minimize the effect of narrowband signal interference. While the SCOT may provide improved broadband signal detection, it may be possible to improve the SCOT, as defined by Carter, et al., by estimating the crosspower function with use of the prediction error transform (PET). King (2) has demonstrated that the

autocorrelation function of broadband signals may be more accurately evaluated using the PET.

1.2 Comparative Evaluation

In order to compare and evaluate the SCOT, SCOT-PET, and the cross-correlation function, a set of receiver operating characteristic (ROC) curves are computed using data simulated for two time dependent function $x(t)$ and $y(t)$. For each function the simulated data contains a coherent, white, broadband signal, incoherent, white broadband noise, and four coherent, narrowband non-harmonic signals.

2.0 THEORY

2.1 Crosscorrelation

The crosscorrelation function may be defined in the time domain by a convolution integral, or in the frequency domain by the Fourier transform. Since it is convenient in this investigation to simulate sensor data in the frequency domain, the crosscorrelation function is defined as follows:

$$\phi_{xy}(\tau) = \int_{-\infty}^{\infty} G_{xy}(f) e^{i2\pi f\tau} df \quad (1)$$

where $G_{xy}(f)$ is the crosspower spectral density function. The crosscorrelation may be normalized by the following equation:

$$\Psi_{xy}(\tau) = \frac{\phi_{xy}(\tau)}{\sqrt{\phi_x(0)\phi_y(0)}} \quad (2)$$

where

$$\phi_x(\tau) = \int_{-\infty}^{\infty} G_x(f) e^{i2\pi f\tau} df \quad (3)$$

$$\phi_y(\tau) = \int_{-\infty}^{\infty} G_y(f) e^{i2\pi f\tau} df \quad (4)$$

where $\phi_x(\tau)$ and $\phi_y(\tau)$ are the autocorrelation functions for the respective signals $x(t)$ and $y(t)$ and $G_x(f)$ and $G_y(f)$ are the auto power spectra evaluated for the respective signals $x(t)$ and $y(t)$. The normalized crosscorrelation as defined by eqn. (2) is evaluated for comparison with the SCOT, which is also a normalized function.

2.2 Smoothed Coherence Transform (SCOT)

The SCOT is defined by Carter et al. (1) as follows:

$$C(\tau) = \int_{-\infty}^{\infty} W(f) \gamma(f) e^{i2\pi f\tau} df \quad (5)$$

where $W(f)$ is a weighting function of choice, and $\gamma(f)$ is the crosspower spectral density function with a frequency dependent normalization. The spectral function is defined as follows:

$$\gamma(f) = \frac{G_{xy}(f)}{\sqrt{G_x(f)G_y(f)}} \quad (6)$$

where $G_{xy}(f)$, $G_x(f)$ and $G_y(f)$ are the crosspower and auto-power spectral density functions evaluated for the respective

signals $x(t)$ and $y(t)$. For the applications considered in this investigation all power spectral density functions are defined in the frequency domain.

2.3 The SCOT-PET Function

The autocorrelation function may be represented by the prediction error transform (PET) as demonstrated by King (2) and in a similar manner the crosscorrelation and SCOT functions may also be represented by PET. Actually, PET is simply an inverse Fourier transform, which has a derivation based upon a prediction error function. When applied to SCOT, the cross-spectral function $\gamma(f)$ is estimated or predicted with a discrete convolution filter, and a prediction error is defined in the frequency domain. The maximum entropy power spectra has a similar PET representation based upon a prediction error defined in the time domain.

The PET may be a useful representation of a function that is derivable from a Fourier transformation. The PET representation is useful only if the transformed function (such as $\gamma(f)$) is known over a limited region in the time or frequency domains. In order to derive the PET the transformed function must also be a predictable (non-random) function or have predictable components.

The cross-power spectral function $\gamma(1)$ has a predictable, periodic modulation given by

$$e^{i2\pi fT}$$

where T is the time delay between two broadband signals $X(t)$ and $X(t+T)$ which have a common, coherent, broadband component. If the periodic modulation is well defined in a low noise environment over a sufficient spectral interval, then the Fourier transform of the modulating component, $\exp(i2\pi fT)$, is a well defined, detectable SINC function centered about T in the time domain. However,

if noise or other interfering components are present in the cross power spectral function $\gamma(f)$, then the SCOT function, which is defined by the Fourier Transform, may not provide a well defined SINC function representative of the coherent, broadband signal component. When interference or noisy components are present, or when the cross-power spectral function $\gamma(f)$ is known only over a limited bandwidth, then the periodic modulation component of $\gamma(f)$ may be better defined with use of the prediction filter a_n as follows:

$$\hat{\gamma}_f = \sum_{n=1}^N a_n \gamma_{f-n} \quad (7)$$

where γ_f is the discrete representation (N components) of the function $\gamma(f)$. A prediction error e_f may be defined by the expression

$$e_f = \gamma_f - \hat{\gamma}_f \quad (8)$$

and a new filter b_n^N , the prediction error filter, may be introduced as follows:

$$e_f = \sum_{n=0}^N b_n^N \gamma_{f-n} \quad (9)$$

If it is recalled that the SCOT, $C(\tau)$, is defined as the Fourier transform of $\gamma(f)$, then the Fourier transform of eqn. (9) results in the following expression:

$$E_N = C(\tau) \sum_{n=0}^N b_n^N e^{-i2\pi n(\Delta f)} \quad (10)$$

where E_N is the Fourier transform of e_f . The SCOT function is defined by solving eqn. (10) as follows:

$$C(\tau) = \frac{E_N}{\sum_{n=0}^N b_n^N e^{-i2\pi n(\Delta f)}} \quad (11)$$

The SCOT, as defined by eqn. (11), is the inverse of the Fourier transform of the prediction error filter b_n^N . The inverse Fourier transform solution is called the prediction error transform, because its derivation is a result of the definition and application of the prediction error filter.

The prediction error filter coefficients, b_n^N , may be evaluated by squaring and minimizing the error given by eqn. (9). The solutions for the coefficients b_n^N and the constant E_N have been formulated by King (3) with use of the Burg technique. The solution agrees with that obtained by Burg (4), who found the unknown coefficients by maximizing the entropy. Solutions for E_N and b_n^N are a set of iterative equations listed as follows:

$$E_1 = r_0^2 \quad (12a)$$

($r_0^2 \equiv$ zero delay autocorrelation coefficient
of data set γ_f consisting of M data samples)

$$E_{N+1} = E_N \left[1 + (b_{N+1}^{N+1})^2 \right] \quad (12b)$$

$$b_1^N = 1.0 \quad (13a)$$

$$b_{N+1}^{N+1} = \frac{\sum_{j=1}^{M-N+1} (\beta_j^N)^* \alpha_{j+N}^N}{\sum_{j=1}^{M-N+1} \left[(\beta_j^N)^2 + (\alpha_{j+N}^N)^2 \right]} \quad (13b)$$

$$b_n^{N+1} = b_n^N + b_{N+1}^{N+1} (b_{N-n+2}^N)^* \quad (13c)$$

The forward prediction errors α_j^N , and the backward prediction errors β_j^N are defined as a function of the known, cross-power spectral data set γ_f as follows:

$$\alpha_{j+1}^1 = \gamma_{j+1} \quad (14a)$$

$$\alpha_j^{N+1} = b_{N+1}^{N+1} \beta_{j-N}^N + \alpha_j^N \quad (14b)$$

$$\beta_j^1 = \gamma_j \quad (15a)$$

$$\beta_j^{N+1} = (b_{N+1}^{N+1})^* \alpha_{j+N}^N + \beta_j^N \quad (15b)$$

3.0 DATA SIMULATION

Since the crosscorrelation, SCOT, and SCOT-PET functions must necessarily be evaluated in succession and repeatedly in order to plot a set of ROC curves, it is wise to simulate data in the frequency domain if possible, so as to prevent repeated transformations of data sets otherwise simulated in the time domain. Both the cross-correlation and SCOT functions require a representation of the crosspower spectral function $G_{xy}(f)$. The spectral function $G_{xy}(f)$ may be expressed very simply by assuming that the broadband and narrowband signal components are steady state signals such that

$$G_{xy}(f) = G_B(f) e^{i2\pi fT} + G_N e^{i2\pi fT} \quad (16)$$

where $G_B(f)$ is the autopower spectra of the coherent broadband component and G_N is the autopower of the coherent narrowband component and the time delay between the functions $x(t)$ and $y(t)$ is T seconds. Since it is assumed that the signals $x(t)$ and $Y(t)$ both contain incoherent, broadband components,

the respective autopower spectral functions $G_x(f)$ and $G_y(f)$ are given by:

$$G_x(f) = G_I(f) + G_B(f) + G_N \quad (17)$$

$$G_y(f) = G_I(f) + G_B(f) + G_N$$

where the incoherent broadband components $G_I(f)$ is assumed to be of equal power for both $x(t)$ and $y(t)$.

The signal component spectra may take any form over a given bandwidth, but in order to establish a standard for future ROC curve comparisons, all broadband spectra (incoherent and coherent) are defined to be uniform (white) spectra over an arbitrary bandwidth. By assuming white broadband spectra, the whitening effect of frequency dependent normalization (used in the SCOT function) is minimized. Consequently, the improvement in signal detection, provided by the SCOT, is a minimal improvement due only to the normalization of the narrowband components.

The broadband spectral components are assumed to have signal amplitudes with Gaussian distributions such that,

$$G_I(f) = \sigma_I^2 \ln(1/R_I) \quad (18)$$

$$G_B(f) = \sigma_B^2 \ln(1/R_B) \quad (19)$$

where R_I and R_B are uniformly distributed random numbers. Values are assigned by arbitrarily letting

$$\sigma_I = 1.0$$

and by defining a broadband power SNR as follows:

$$\begin{aligned} \text{BBSNR} &= 10 \log(\sigma_B^2/\sigma_I^2) \\ \text{BBSNR} &= 10 \log(\sigma_B^2) \end{aligned} \quad (20)$$

Similarly, a narrowband SNR is defined with respect to unit power so that,

$$\text{NBSNR} = 10 \cdot \text{Log}(G_N) . \quad (21)$$

It remains only to specify values of the cross-correlation normalization functions $\phi_x(o)$ and $\phi_y(o)$ as follows:

$$\begin{aligned} \phi_x(o) &= \int_{-1}^1 \left[G_I(f) + G_B(f) \right] df + G_N \\ \phi_x(o) &= 2 \left[G_I + G_B \right] + G_N, \end{aligned} \quad (22)$$

where the spectral components are arbitrarily defined to exist over a spectral band from -1 to +1. Since identical component power levels are assumed in both signals $x(t)$ and $y(t)$,

$$\phi_y(o) = \phi_x(o) \quad (23)$$

The crosspower spectral functions $G_{xy}(f)$, $\phi_{xy}(f)$ and the autopower functions $G_x(f)$, $G_y(f)$, $\phi_x(o)$, $\phi_y(o)$ are all specified by the preceding equations for given values of BBSNR and NBSNR. The crosscorrelation, SCOT, and SCOT-PET are Fourier or Prediction Error transforms of the defined crosspower and autopower spectral functions as defined by eqns. (2), (5), (6) and (11). A set of ROC curves may be constructed by re-evaluating the cross-correlation, SCOT, and SCOT-PET functions repeatedly, and counting the false-alarm peaks and signal peaks above specific threshold values.

4.0 EXAMPLES OF CROSSPOWER FUNCTIONS

The complex, crosspower spectral function $\gamma_{xy}(f)$ is computed and plotted in Figs. 1, 2 and 3. The spectral function consists of white, broadband, coherent and incoherent

components and four equal power narrowband components. The magnitude function $|\gamma_{xy}(f)|$ is observed in Fig. 1 for 128 computed points, and for a broadband SNR = 1.55 dB, and a narrowband SNR = 20 dB. The real part of $\gamma_{xy}(f)$ is shown for 128 computed points and the same SNR values in Fig. 2. The real part of $\gamma_{xy}(f)$ is also shown in Fig. 3 for 128 computed points, but with the BBSNR = -20 dB and the NBSNR = 10 dB.

The low frequency modulation observed in Fig. 2 is not real, but is rather due to a sampling rate which is inadequate for display purposes, although it is adequate for computational purposes. The higher frequency component

$$e^{i2\pi fT}$$

is well defined in Fig. 2, but not so visible in Fig. 3 due to the large difference in BBSNR. Of course when the BBSNR is reduced as in Fig. 3, the four narrowband components are more visible.

5.0 EXAMPLES OF CROSSCORRELATION, SCOT, AND SCOT-PET TIME FUNCTIONS

The normalized crosscorrelator time function (in decibel units) is shown in Fig. 4 for a time delay of -0.3 sec., BBSNR = -20 dB, and four narrowband components of 10 dB each. The broadband signal peak is visible at the time delay of -0.3 sec., but only slightly above the largest clutter peaks. The SCOT time function (in decibel units) computed for the same SNR values (as used in Fig. 4) has a more prominent signal peak as observed in Fig. 5. The signal peak height is the only noticeable difference between the crosscorrelator and SCOT time functions. The clutter patterns for each time function are identical, because the broadband signal and noise spectra are uniform (white) spectral distributions. The clutter patterns would

be very different if the broadband spectra were not uniformly (non-white) distributed, because the SCOT has a frequency dependent normalization. Consequently, the detection characteristics of the SCOT and SCOT-PET functions are expected to improve significantly for non-white broadband spectral functions.

The SCOT-PET time function, which is computed for the same SNR parameters used in Figs. 4 and 5, is shown plotted in decibels in Fig. 6. The signal peak is even more prominent at the time delay of -0.3 sec., and fewer clutter peaks are observed than in the two previous time functions. Based upon the three detector time functions shown in Figs. 4 - 6, the SCOT-PET time function appears to offer the best signal detection capability.

6.0 ROC CURVES

6.1 Construction Based Upon 100 Time Functions

One set of time functions is insufficient evidence to form judgment, so a set of receiver operating characteristic (ROC) curves are constructed based upon 100 sets of computed time functions. The results are shown in Figs. 7, 8 and 9. The ROC curves are constructed for false alarm probabilities between .01 and 1.0. Lower values of the false alarm probability would require that many more correlation, SCOT, and SCOT-PET time functions would necessarily be computed. While the range of false alarm probabilities investigated are not necessarily of practical value, they are adequate for comparing the three different detectors. The set of three ROC curves are constructed for a BBSNR = -25 dB and a NBSNR = 10 dB (for each of four NB signals). The crosscorrelation, SCOT, and SCOT-PET ROC curves are shown in Figs. 7, 8 and 9 respectively. Of the three ROC curves shown the SCOT has the best detection probabilities. Of course the lower false alarm probabilities

are usually of more interest in underwater acoustics applications, but only for detection probabilities above 0.5. The SCOT-PET ROC curve has the lowest false alarm probability for the detection probability of 0.5.

The constructed ROC curves are more reliable in regions of high false alarm probabilities due to the high density of data collected in those regions. Consider that data points with a detection probability of 1.0 are based upon 100 signal detections whereas a data point representing a detection probability of 0.01 is based upon only one detected signal.

6.2 Other BBSNR Values

Two other sets of ROC curves are constructed for BBSNR values of -40 dB and -20 dB to illustrate the similarities and differences of the three broadband signal detectors with changing BBSNR values. Again, four narrowband signals having NBSNR = 10 dB each are employed in constructing the ROC curves. In order to minimize computing time and costs, these and other ROC curves are constructed from only 25 sets of time functions. However, these ROC curves are presented only to indicate trends due to parameter variation. In Fig. 10 the crosscorrelator, SCOT and SCOT-PET ROC curves are shown on the same graph for a BBSNR = -40 dB. The crosscorrelator and SCOT ROC curves are nearly identical for all false alarm probabilities, whereas the SCOT-PET ROC curve has shifted toward higher false alarms. Detection performance has deteriorated significantly for the SCOT and even more so for the SCOT-PET. However, the detection performance has changed only slightly for the crosscorrelator. Apparently, the SCOT approaches the crosscorrelator performance and the SCOT-PET performance deteriorates toward lower detection probabilities with decreasing BBSNR values.

The set of ROC curves constructed for BBSNR = -20 dB is shown in Fig. 11. The SCOT-PET ROC curve clearly indicates

superior detection performance at lower false alarm probabilities, although the SCOT is also considerably better than the crosscorrelator for lower false alarm probabilities. Again the crosscorrelator ROC curve has changed only slightly toward an improved detection performance. It is apparent that for the BBSNR values investigated, the crosscorrelator detection performance is inadequate for applications requiring a low false alarm probability. But both the SCOT and SCOT-PET may have useful detection characteristics in regions of low false alarm probabilities for BBSNR values of -25 dB or lower. However, this investigation does not examine detection performance capability in regions of low false alarms.

6.3 Partially Coherent Broadband Noise

All previous discussions and examples have assumed that the broadband noise (occurring in the signals $x(t)$ and $y(t)$) is incoherent. But complete incoherence is unlikely in most radar clutter environments. For example, low level partially coherent, directional, broadband signals may be present in the atmospheric clutter or in receiver channels. Therefore, a set of ROC curves are shown in Fig. 12 for a BBSNR = -25 dB and four narrowband components having a NBSNR = 10 dB each. The ROC curves of Fig. 12 indicate that the detection performance of all three detectors has deteriorated, but by very different amounts. The SCOT-PET has suffered the most performance deterioration, while the crosscorrelator has only suffered a slight deterioration. While the SCOT detection performance is diminished by the noise partial coherence, the SCOT detection performance remains superior to that of the crosscorrelator.

7.0 SUMMARY

The broadband signal detection performance of the

crosscorrelator, SCOT, and the SCOT-PET have been compared for an environment containing four strong, interfering, narrowband signal components, and strong, independent, broadband noise. Under such conditions, the crosscorrelator exhibits poor, but stable detection performance, whereas the SCOT and SCOT-PET appear to have useful detection characteristics in regions of low false alarm probabilities. However, the SCOT and SCOT-PET detection performance is inhibited by increasing noise levels and increasing noise coherence. The SCOT-PET has the best detection performance for low and incoherent noise conditions, but the SCOT detection performance becomes superior as noise levels and noise coherence increases.

Unfortunately, the constructed ROC curves do not indicate the actual detection performance of the SCOT and SCOT-PET in regions of very low false alarm probabilities. Most detector applications require very low false alarm probabilities. However, the constructed ROC curves do show that the SCOT and SCOT-PET have application in the presence of strong, narrowband signal components, which very severely degrade the detection performance of the crosscorrelator.

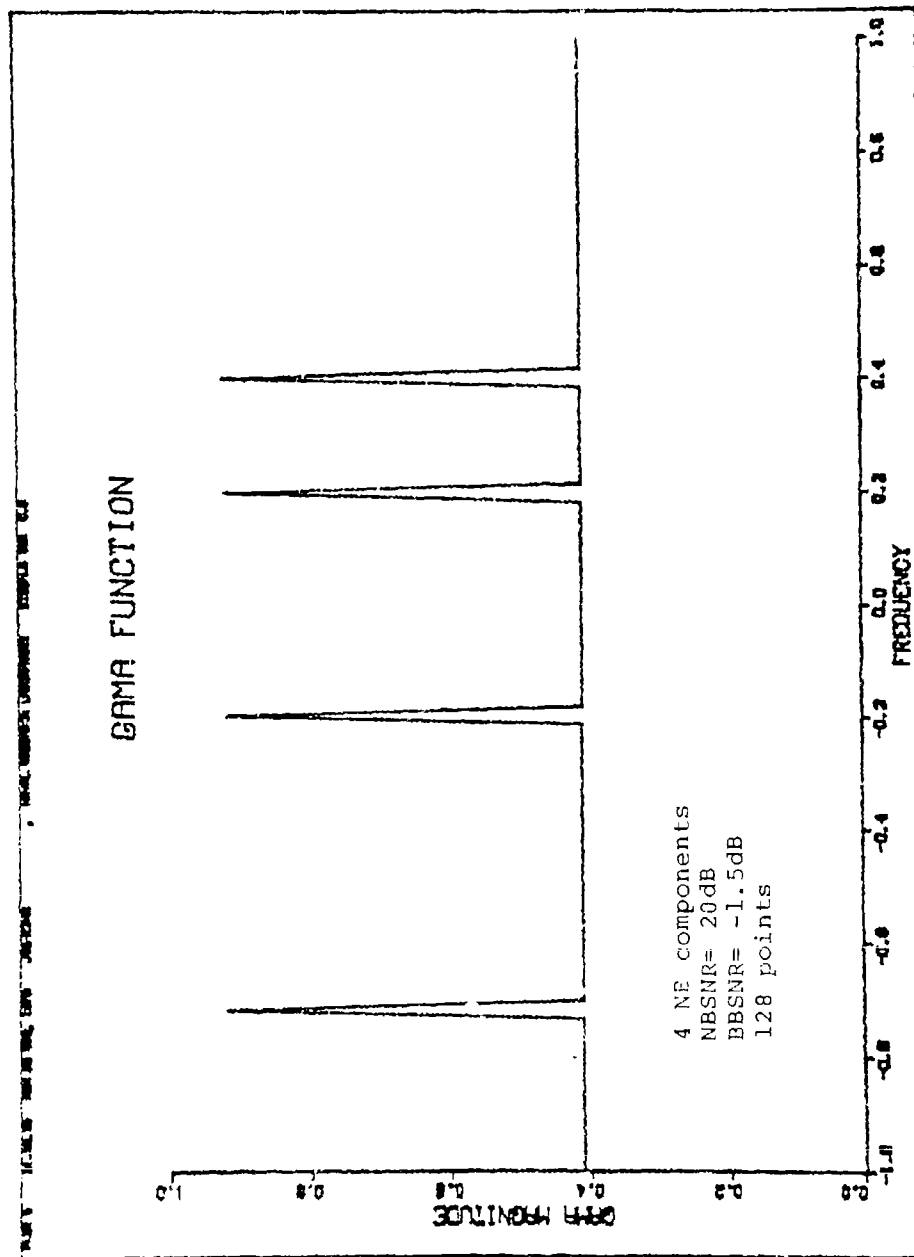
Both the SCOT and SCOT-PET will have even better detection capability in the presence of non-white, broad band noise. Also, the detection performance of the SCOT-PET may be improved further with use of larger filter sizes and when fewer cycles of the modulation component

$e^{j\omega t}$

are present. These initial conclusions indicate that the SCOT and SCOT-PET deserve serious consideration as broadband signal detectors, and that their detection characteristics should be investigated further.

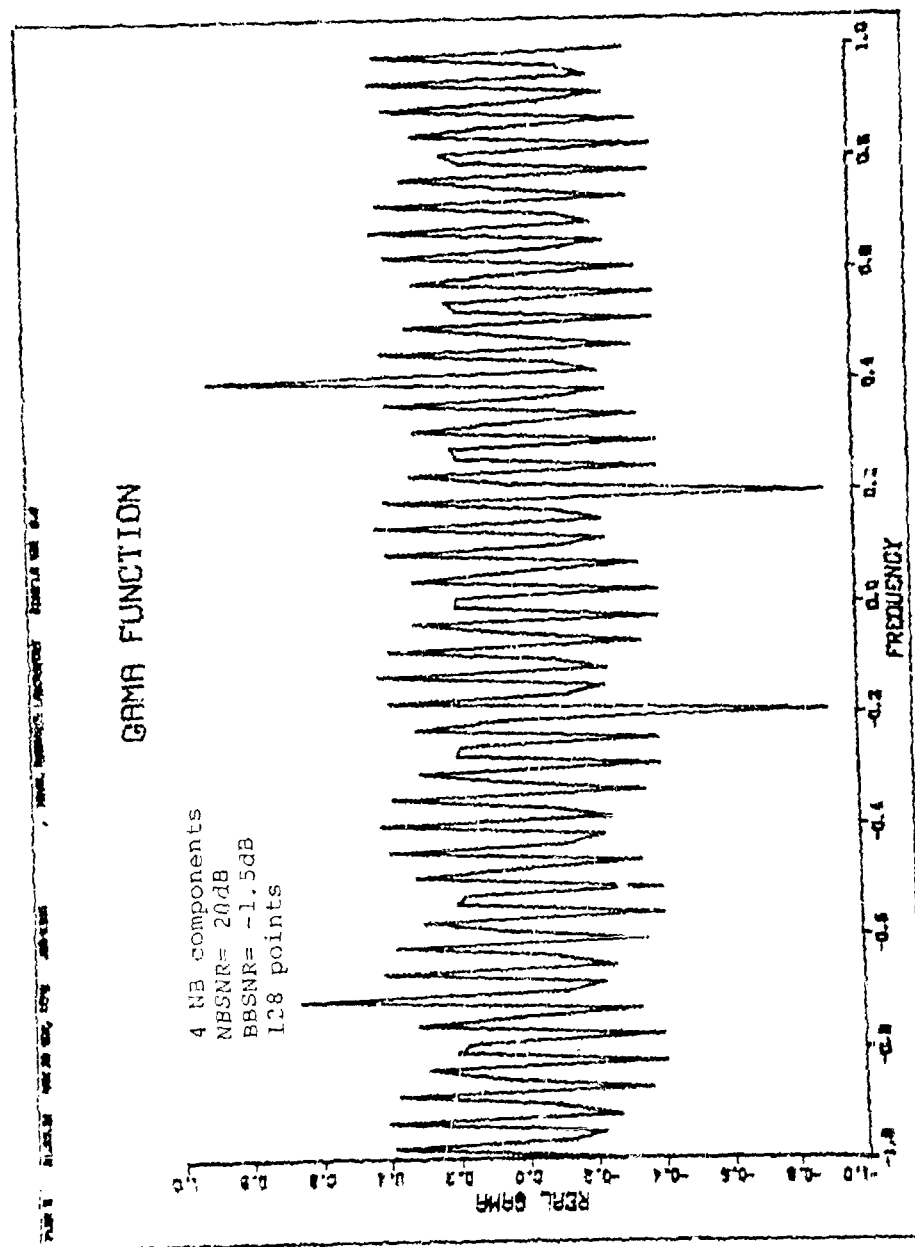
REFERENCES

1. Carter, Nuttall and Cable, "The Smoothed Coherence Transform", IEEE Proceedings, Vol. 61, No. 10, pp. 1497-1498, Oct. 1973.
2. King, W. R., "Applications for MESA and the Prediction Error Filter", Proceedings of the RADC Spectrum Estimation Workshop, Griffiss AFB, NY, DDC#A054650, Oct. 3-5, 1979.
3. King, W. R. "Maximum Entropy Wavenumber Analysis", NRL Report 8298, Naval Research Laboratory, Wash. D.C., March, 1979.
4. Burg, John P., "Maximum Entropy Spectral Analysis", PhD Thesis, Stanford Univ., #75-25, 499 Univ. Microfilms Intl., Ann Arbor, Mich.



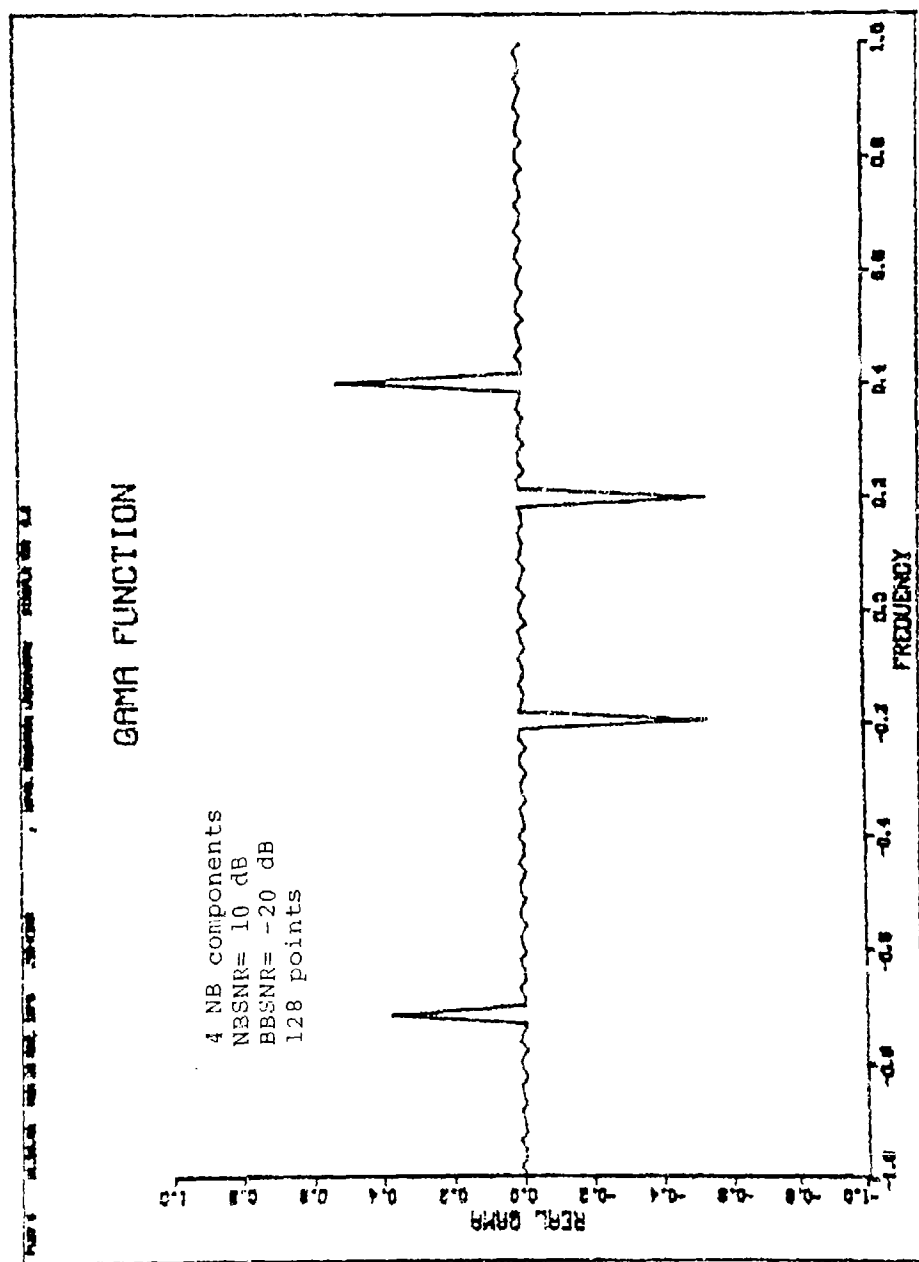
MAGNITUDE OF GAMA FUNCTION

Fig. 1



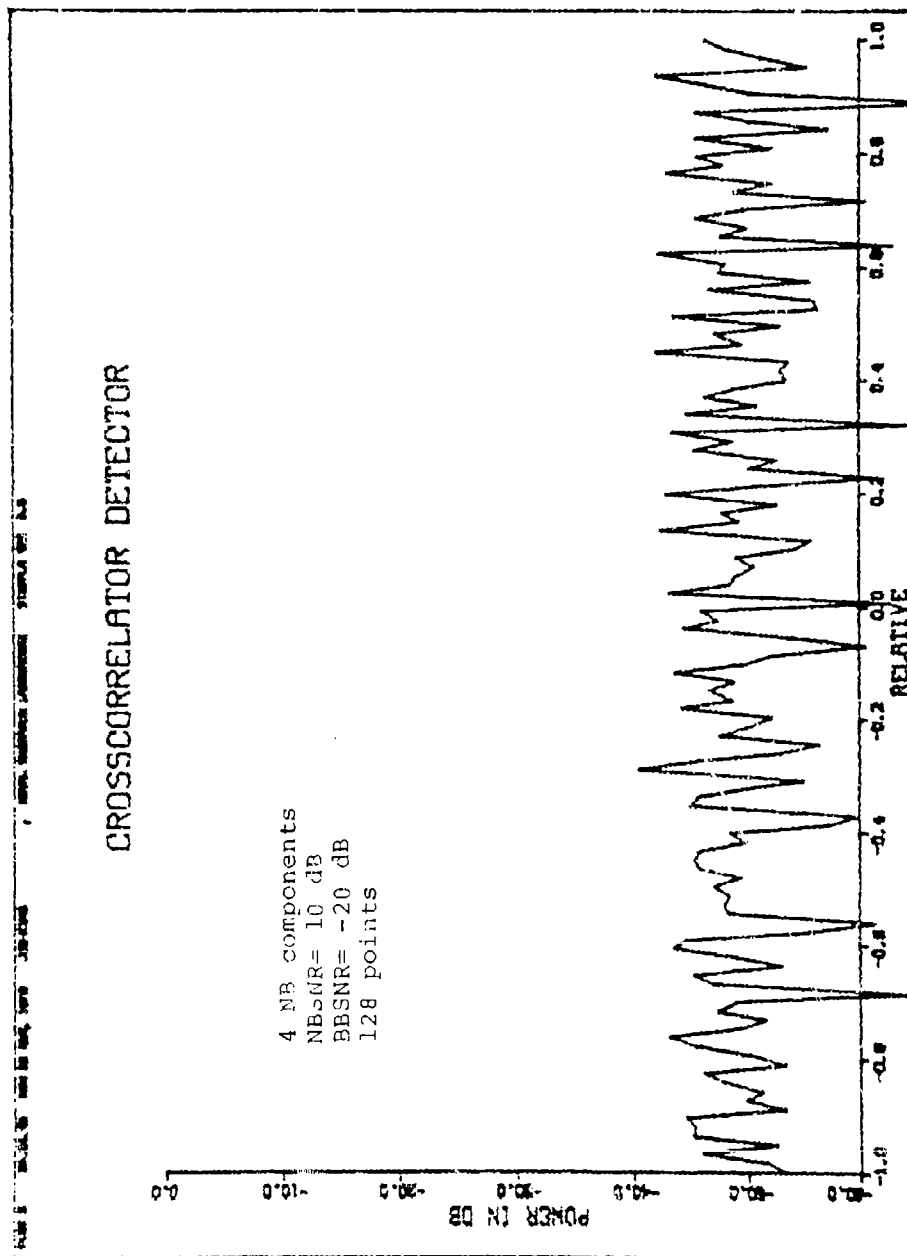
REAL PART OF GAMA FUNCTION

Fig. 2



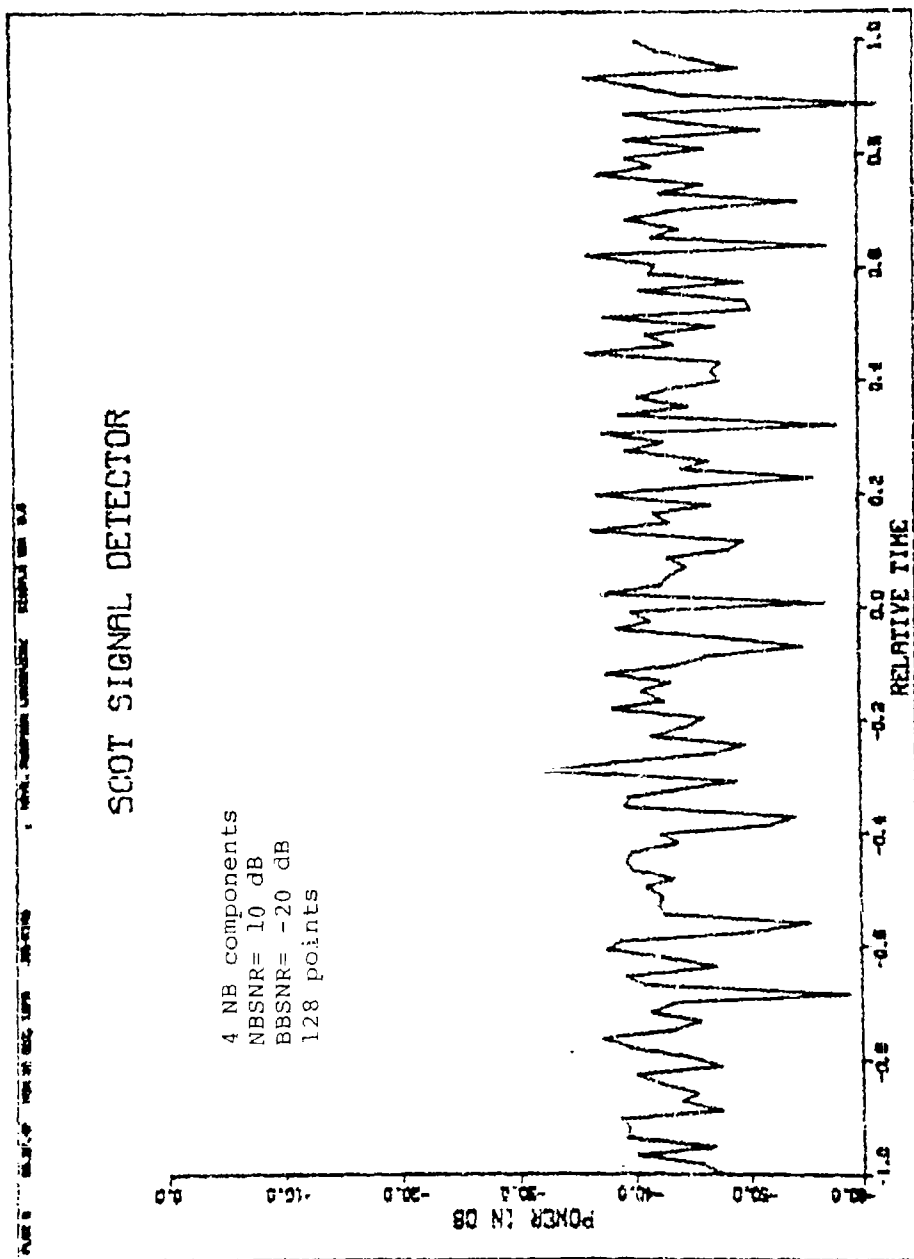
REAL PART OF GAMA FUNCTION

Fig. 3



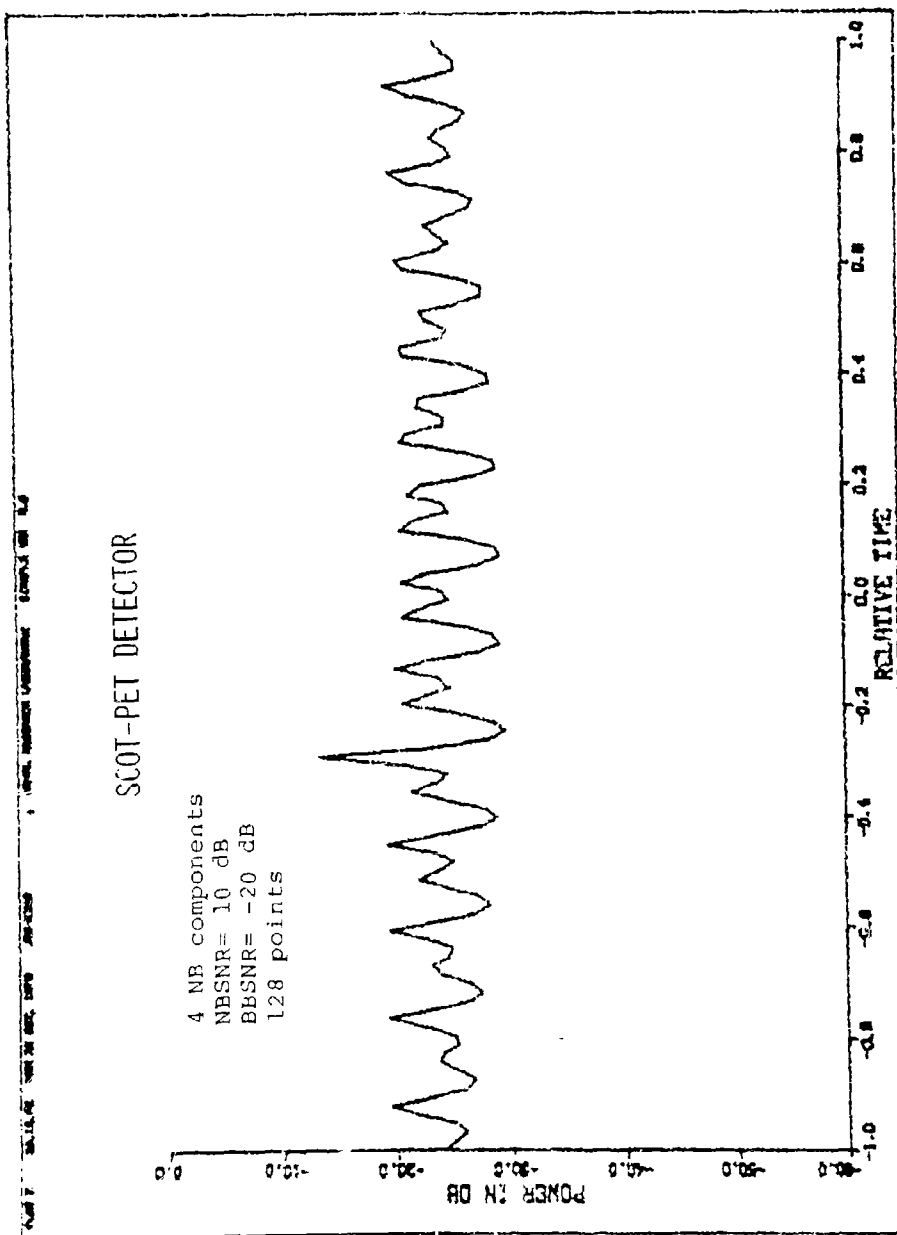
CROSSCORRELATOR TIME FUNCTION

Fig. 4



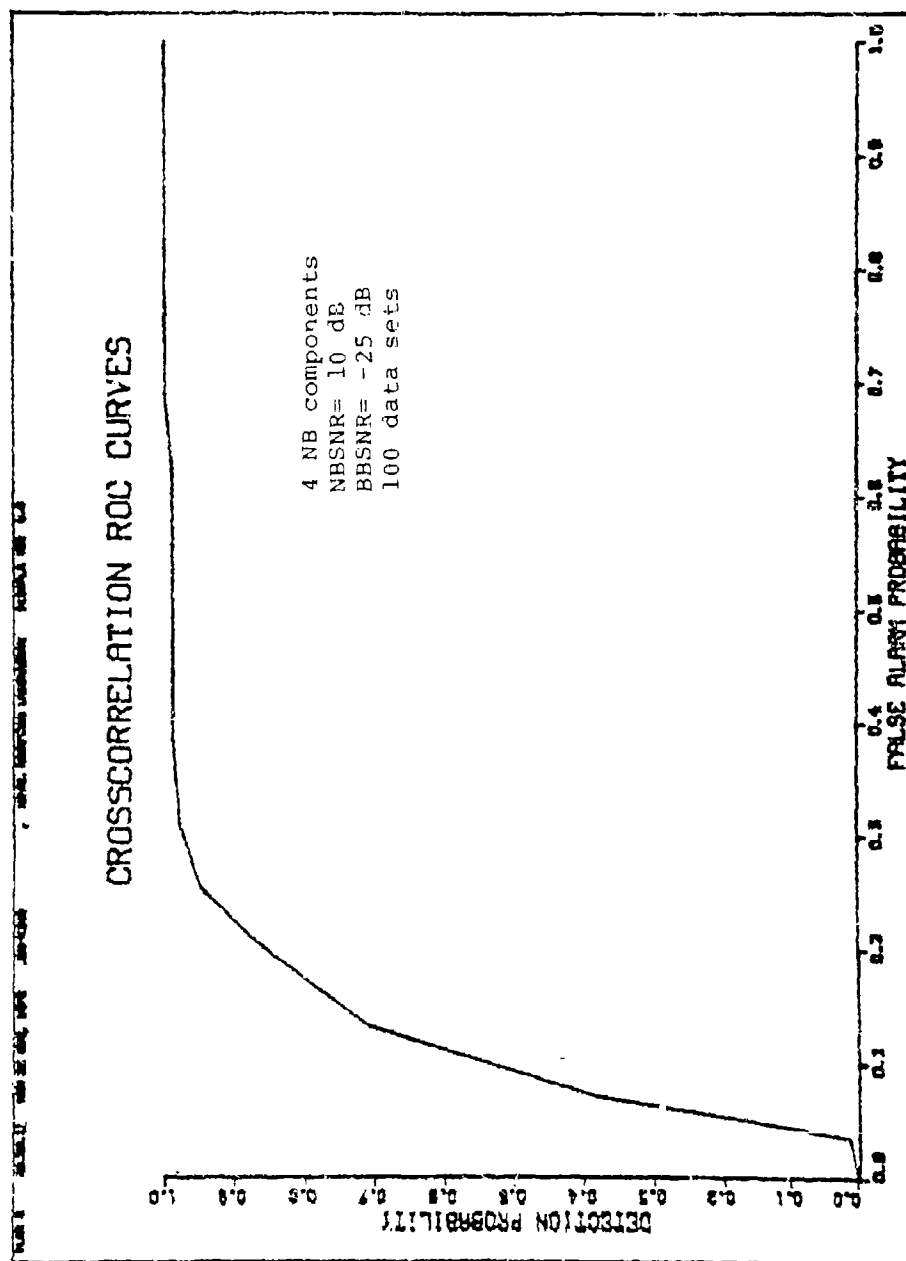
SCOT TIME FUNCTION

Fig. 5



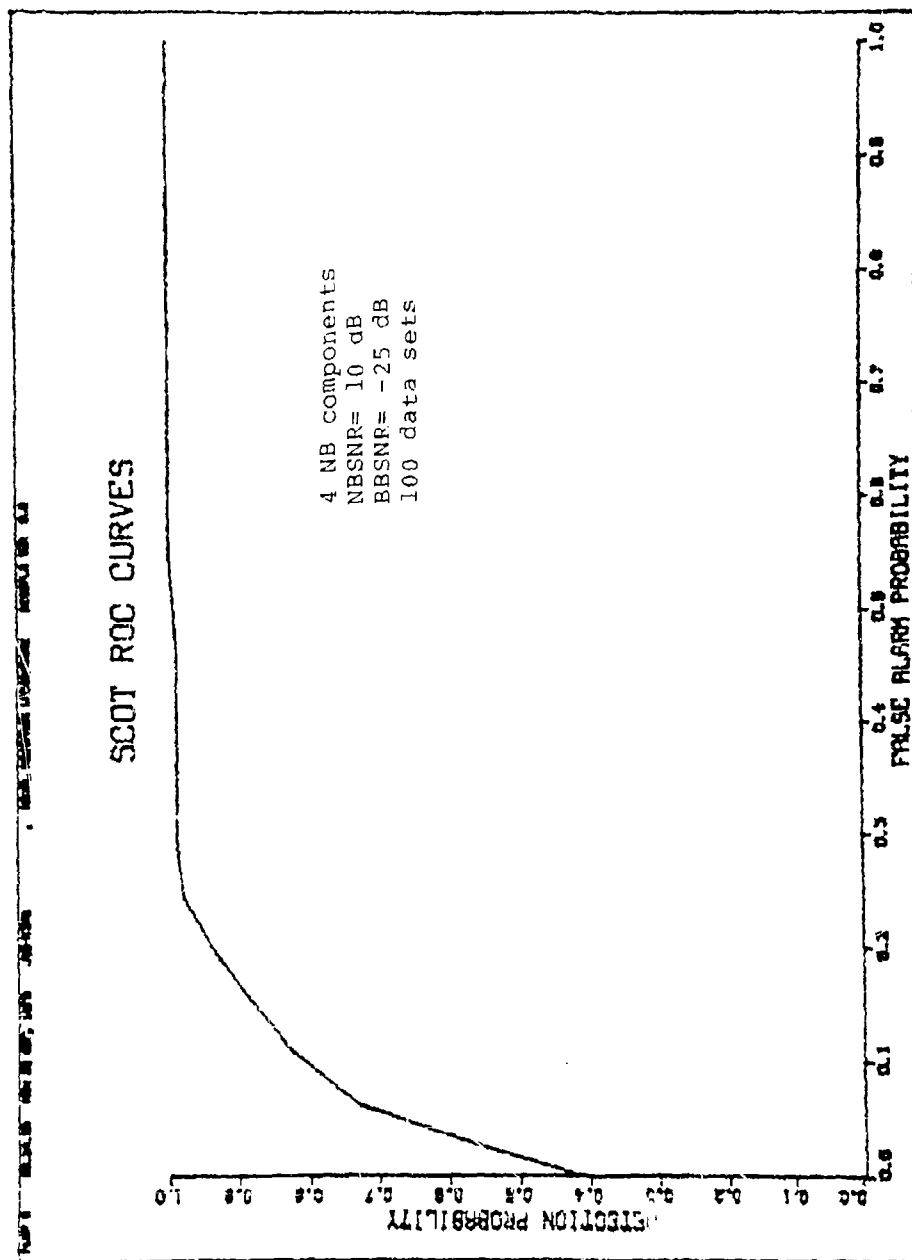
SCOT-PET TIME FUNCTION

Fig. 6



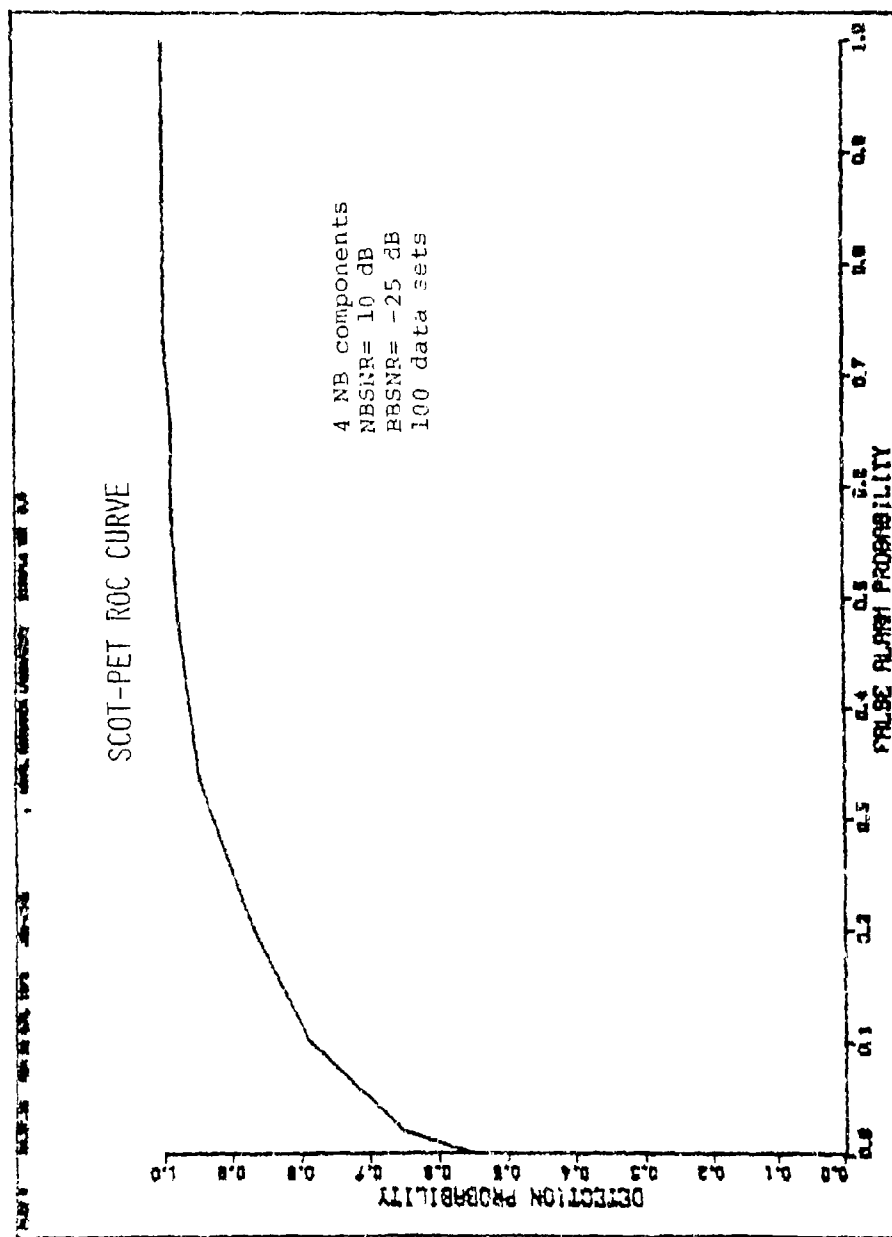
CROSSCORRELATOR ROC CURVE

Fig. 7



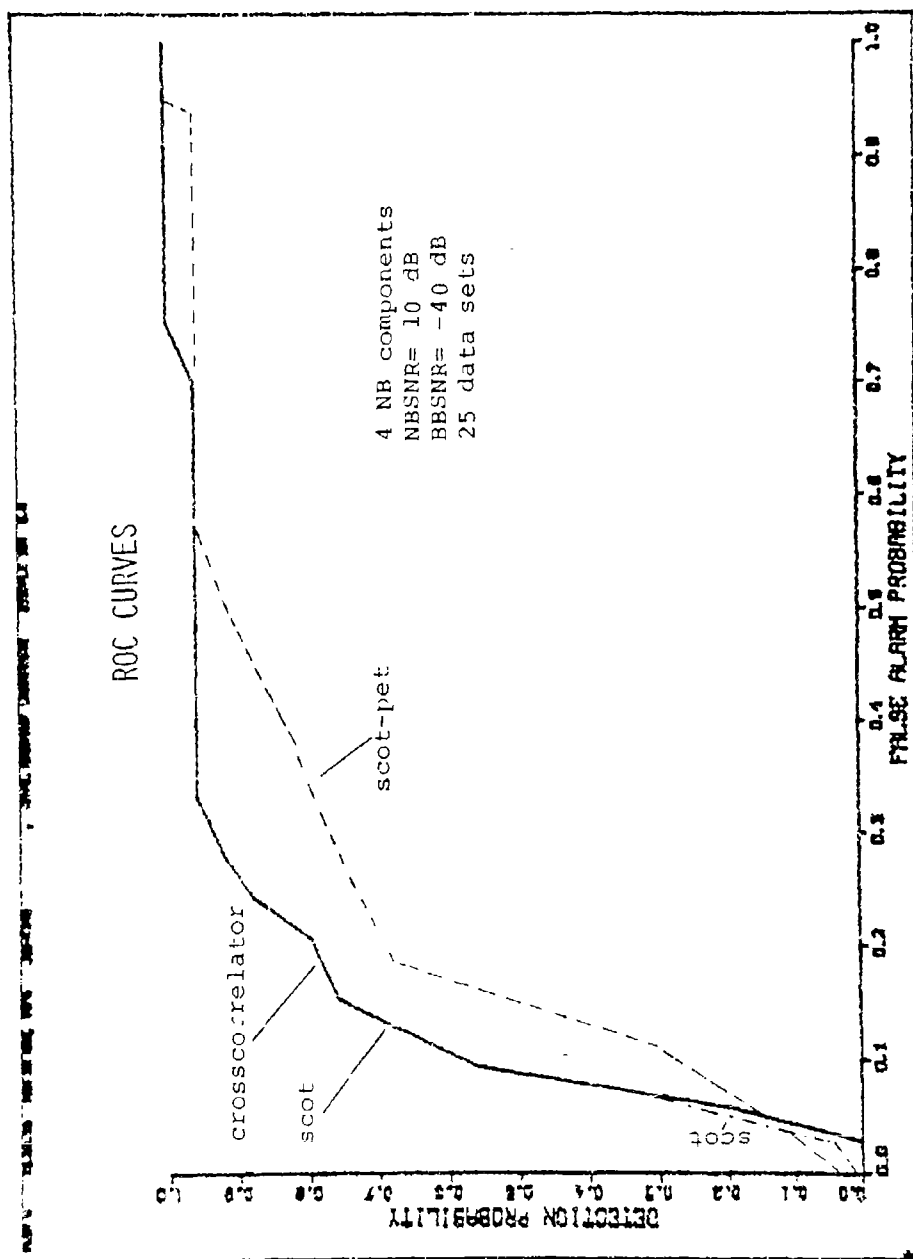
SCOT ROC CURVE

Fig. 8



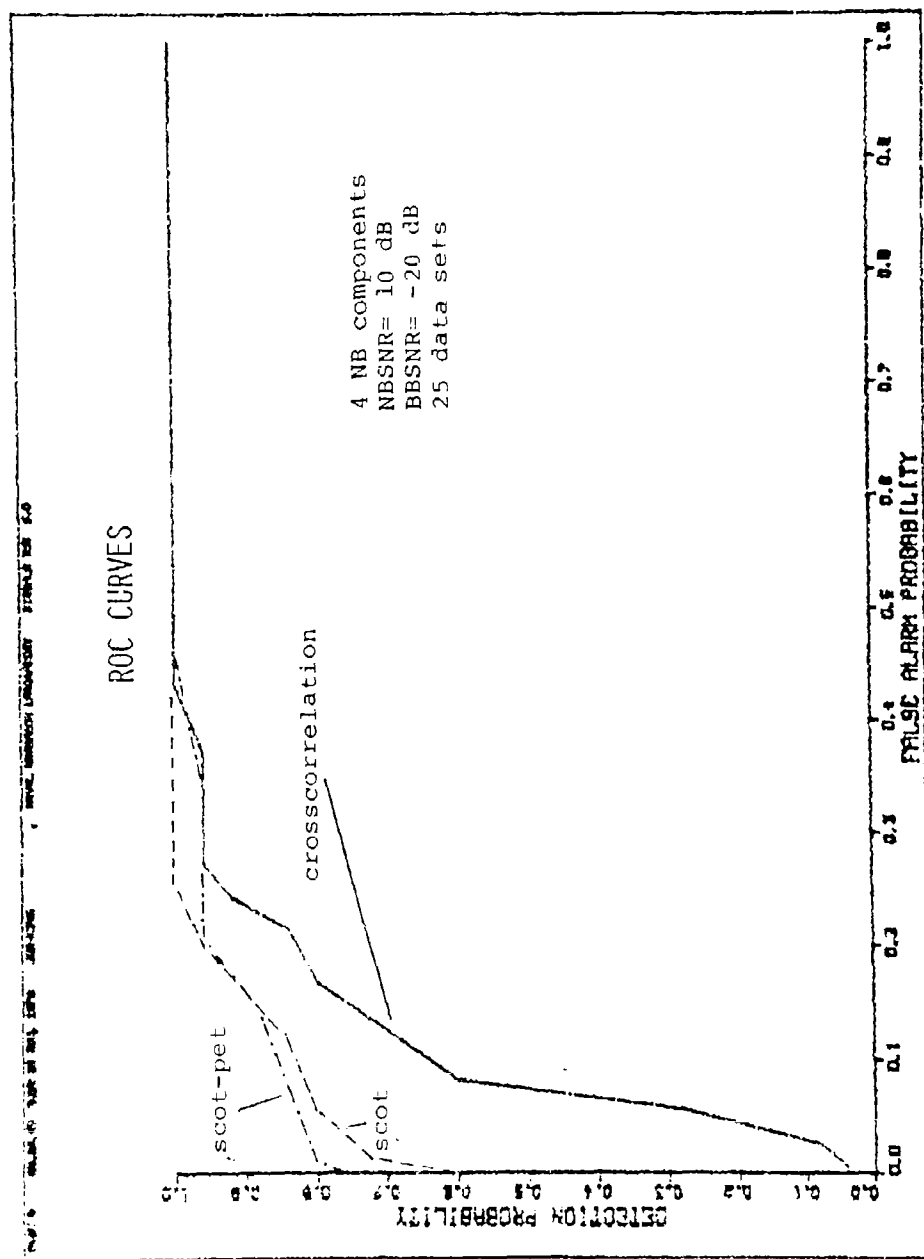
SCOT-PET ROC CURVE

Fig. 9



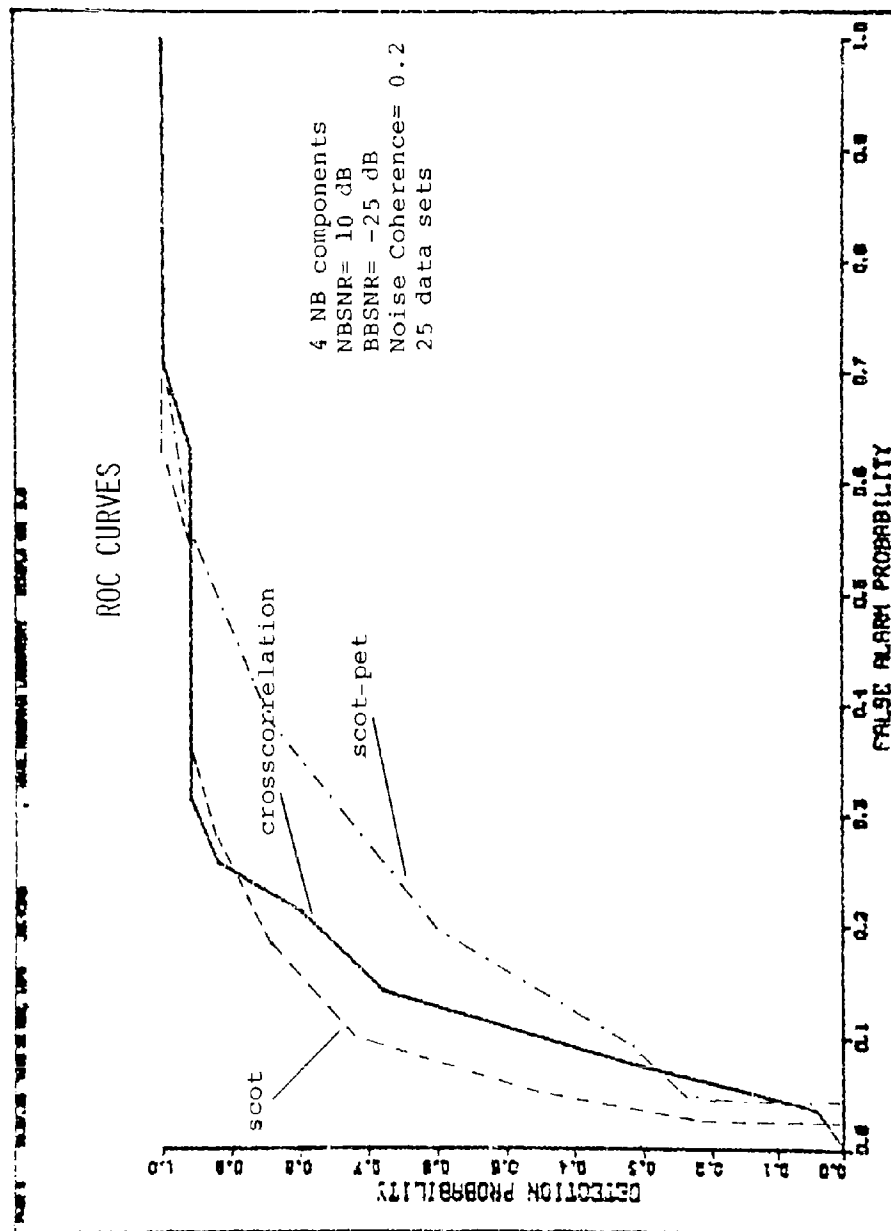
COMPARATIVE ROC CURVES

Fig. 10



COMPARATIVE ROC CURVES

Fig. 11



COMPARATIVE ROC CURVES

Fig. 12

RESOLUTION AND DETECTION CHARACTERISTICS OF THE MAXIMUM ENTROPY METHOD

1.0 Introduction

Investigations of the maximum entropy method (MEM) nearly always provide an examination of the technique and its properties with the use of simulated data. It is thought that this report describes one of the earliest investigations of MEM using actual radar signals that are received with a uniform, linear, antenna array. Stable MEM wavenumber spectra that are computed using the actual data apparently have the same high resolution that has been so often demonstrated with simulated data. Simulated data cannot include all the characteristics of actual radar data, which is usually strongly anisotropic in wavenumber and time variant. Therefore, tests of the MEM that use actual radar data are most significant in demonstrating the usefulness and accuracy of MEM.

Since the MEM is effective in whitening a spectra, it may be useful for detecting radar signals that are often obscured by powerful but anisotropic radar clutter. The MEM is demonstrated to indeed be a likely candidate for further study as a detector of weak radar signals present in a doppler radar receiver.

2.0 Radar Data

The MEM and MLM techniques are applied to actual radar data that is collected by a 14 sensor linear array within a laboratory environment. Two sources, each having power levels of 43 dB above the averaged background radiation, are located at 18 and 22 degrees from the 0 degree radial which is normal to the linear array. The sensor array and radar sources are both located within an anechoic room which substantially reduces specular wall reflections. However,

the non-specular reflections which are detected by the array make up a highly colored background wavenumber spectrum. Receiver noise and sensor phase distortion are present, but are unknown spectral quantities.

The 14 sensor array data is collected as (I-Q pair) data so that 14 complex numbers or 28 channels of data are collected and recorded. The radar signals are short duration pulses so that each set of 14 complex numbers represent one spatial snapshot. A total of 1024 snapshot data are recorded.

A phased array antenna pattern has a mainlobe beamwidth of 13.4 degrees (at the -3 dB levels) for a 14 sensor, 7.5 wavelength array. Consequently, two sources separated by only 4 degrees are not resolved with a conventional summed, phased array, antenna pattern.

2.1 The Maximum Entropy Method (MEM)

Two methods of obtaining stable MEM wavenumber spectra are employed for analyzing the array radar data. One method employs averaged covariance matrices and the other method utilizes averaged prediction error filter weights. Both methods provide stable MEM wavenumber spectra with sufficient resolution to identify the two closely adjacent sources. Both averaging methods are described and demonstrated in an earlier progress report dated 1, Nov. 1979 (1). The MEM algorithm employed in this analysis utilizes the Burg technique, which substantially reduces the computing effort required of the conventional matrix equation formulation. The Burg technique is also described in detail in the earlier progress report (1).

2.2 The Maximum Likelihood Method (MLM)

For comparison purposes, the MLM is also used to analyze the array data. The MLM is evaluated using a prediction error formulation proposed by Burg (2), which is similar

to the MEM spectral formulation. Because of the similarity in formulation, the same prediction error filter weights are computed and used for both the MEM and MLM formulation. The Burg technique is also employed in evaluating the MEM. The MLM formulation is as follows:

$$P_N(k) = \frac{N}{\sum_{n=1}^N P_n^{-1} \Gamma_n(k)} \quad (1)$$

$$\text{where } P_{n+1} = P_n \left[1 - (\gamma_{n+1}^{n+1}) (\gamma_{n+1}^{n+1})^* \right] \quad (2)$$

$$P_1 = r_0^2 \text{ (autocorrelation of data samples)}$$

$$\Gamma_n(k) = \sum_{s=1}^n \gamma_s^n e^{iks(\Delta x)} \quad (3)$$

γ_s^n are prediction error filter weights

$k = (2\pi/\lambda) \sin(\theta)$ (wavenumber component)

θ = signal angle of incidence

λ = signal wavelength

2.3 Results of Analysis

The MEM and MLM wavenumber spectra for the first data snapshot (first set of 14 complex numbers) are shown in Figs. (1) and (2) respectively. The MEM spectra of Fig. (1)

is typical of such single snapshot spectra in that it contains many very sharp peaks of varying magnitude. In such spectra it is often difficult to determine which peaks represent signals. However, there are three large peaks in the MEM snapshot spectra that are at azimuth angles in the vicinity of the two signal incidence angles. The two signals are located at angles of 18 and 22 degrees. More accurate and reliable MEM wavenumber spectra are obtained if particular MEM parameters are averaged over several sets of snapshot data. Subsequent MEM wavenumber spectra, which are shown, do incorporate averaging.

The MLM snapshot wavenumber spectra is shown in Fig. (2) where one large and prominent peak appears at an angle in the vicinity of the two actual signals. In only one snapshot of data the MLM spectra is observed to contain very weak extraneous side (noise) peaks, but does not indicate the presence of both signals. Averaging is incorporated in subsequent computed MLM spectra with the hope of improving resolution in the MLM spectra.

Other MEM and MLM wavenumber spectra are shown in Figs. (3) and (4) for which the covariance matrix is averaged over 6 sets of snapshot data. The MEM spectra of Fig. (3) does indicate the presence of two signals although one signal peak is about 10 or 12 dB smaller than the other. The side peaks are reduced in number and in magnitude in comparison with the MEM snapshot of Fig. (1). The averaging of the 6 covariance matrices has improved the accuracy and reliability of the MEM spectra, but the resolution remains insufficient. The MLM spectra, which is computed for the covariance matrix averaged over 6 sets of snapshot data, has not changed in any significant way in comparison with the snapshot spectra shown in Fig. (2).

The MEM wavenumber spectra, which is shown in Fig. 5, is computed using prediction error filter weights averaged over 6 sets of snapshot data. The MEM spectra of Fig. 5 does indicate the presence of two closely adjacent signals, but the

resolution capability appears inadequate to accurately identify the two signals. Side peaks are still quite numerous and large in magnitude when compared with the snapshot MEM spectra of Fig. (1).

Averaging does improve the resolution capability of the MEM. The MEM spectra is shown in Fig. (6) where the prediction error filter weights are averaged over 12 sets of snapshot data. In Fig. (6) the two signals are well resolved and accurately located at azimuths of 18 and 22 degrees. Also, side peak levels are reduced but are not suppressed as well as with the MLM. One signal peak (at 18 degrees) is about 1 dB below the other signal peak although both signals have the same power level.

In order to resolve the two signals with MEM spectra computed with averaged covariance matrices, further averaging is necessary. In Fig. (7) the two signals are resolved and accurately located by averaging the covariance matrix of an MEM spectra over 18 consecutive sets of snapshot data. However, as in Fig. (6), one signal peak is about 1.5 dB below the other signal peak. The MLM spectra computed using the same averaged covariance matrix is shown in Fig. (8). The two signals are not resolved in the MLM spectra, and are not resolved even with further averaging of the covariance matrix in which 27 sets of snapshot data are utilized.

3.0 Signal Detection

Because of the spectral whitening capability of the maximum entropy method, there is a large improvement in the ratio of SNR (out) to SNR (in). In order to demonstrate the detection capability of the MLM, a typical signal-to-clutter environment is simulated for a doppler radar receiver. Doppler radar clutter is simulated as shown in Fig. (9) where random phased clutter bands have power levels typical of ground, rain, and interference clutter. Such a clutter model has been

used previously by Sawyers (3) in his demonstration of adaptive filtering. A signal having a 0 dB SNR is located between the clutter at the frequency ratio of .375 as denoted by the arrow in fig. (9). The signal is detected as shown in fig. (10) by applying MEM to several sets of 32 data samples and using 24 filter weights. The strong clutter bands are very effectively whitened by MEM such that the largest background peak in fig. (10) is about 10 dB below the signal peak level. Similar results may be obtained for any signal location. For example, in fig. (11) a signal located at the center of the interference clutter (.65) is equally well detected again with MESA applied to consecutive sets of 32 data samples using 26 filter weights. In both fig. (10) and (11) the MEM filter weights are averaged over 30 consecutive sets of 32 data samples. While considerable averaging is used to achieve the results indicated in figs. (10) and (11), less averaging of fewer filter weights may also achieve satisfactory signal detection, but with less resolution capability.

4.0 Summary

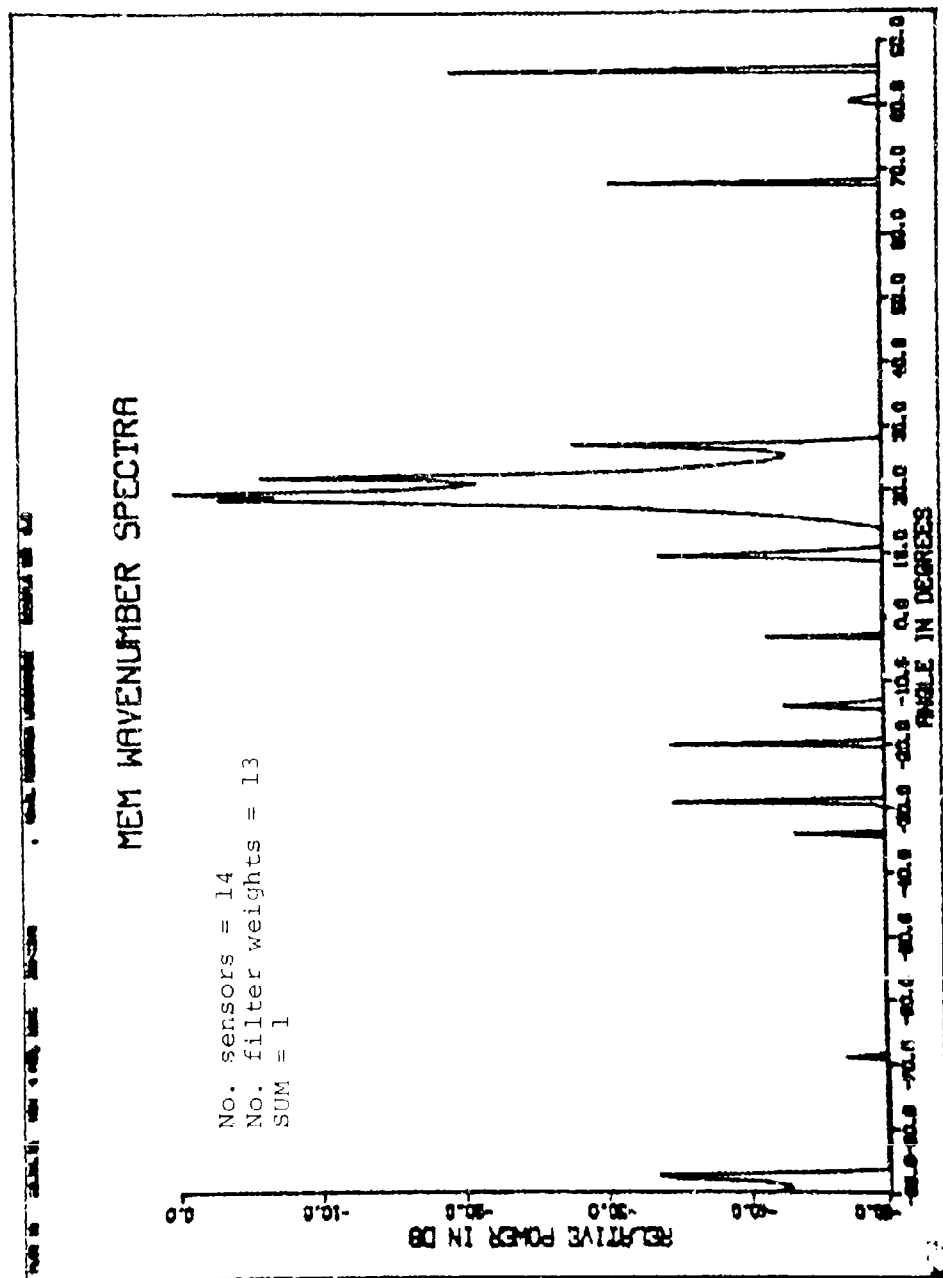
The maximum entropy method is effective in resolving signals located within the mainlobe of a conventional antenna pattern. However, the MEM is accurate and stable only if some form of parameter averaging is utilized. As demonstrated, the MEM as compared to the MLM has superior resolution, but the MLM appears to more effectively whiten the background (noise) spectra. Previous progress reports issued under this investigation contained MEM spectra which were computed using only simulated data. In this report all MEM spectra are obtained using actual radar signals received by a 14 sensor linear array. Previous simulated data contained simulated Gaussian, white noise, but in this report the collected radar data contains typical receiver and sensor noise and distortion. It is reassuring to know that the MEM is effective in resolving closely

adjacent signals mixed with either simulated white noise or with actual and typical electronic system noise spectra.

The results achieved with the MESA doppler radar detector are most promising. However, such exceptional results did require an average of over 32 sets of computed prediction error filter weights. Real time applications may not allow for such a large average. Because of the excellent spectral whitening characteristics that are exhibited by the MLM, perhaps the MLM is a more promising technique for real time doppler radar detection. Either MESA or MLM appear to offer considerable improvement in radar signal detection.

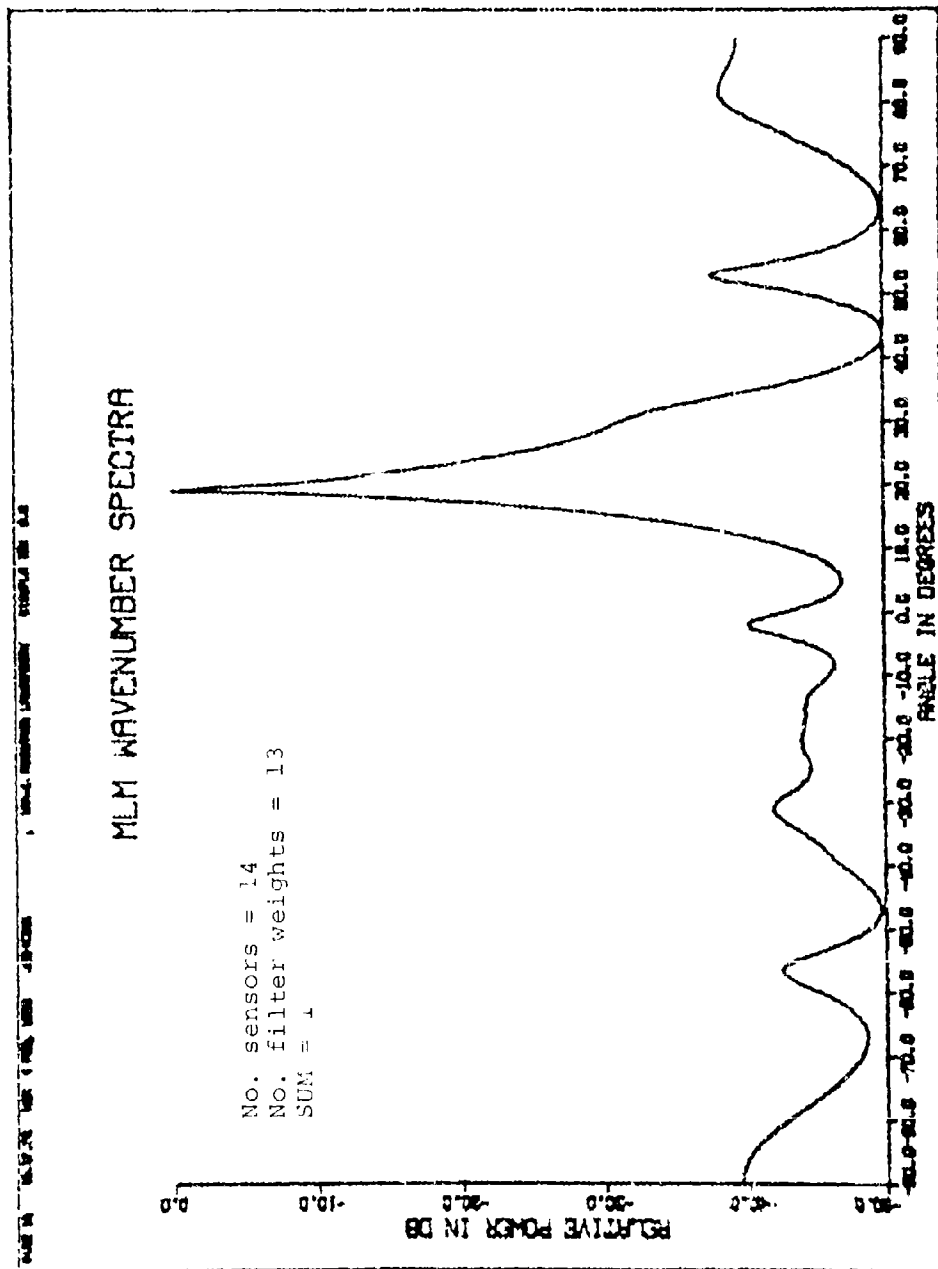
REFERENCES

1. King, William R., "Applications for MESA and the Prediction Error Filter", Proc. of the RADC Spectrum Estimation Workshop, pp. 273-288, 3-5 Oct. 1979
2. Burg, John P. "The Relationship between Maximum Entropy Spectra and Maximum Likelihood Spectra", Geophysics, Vol. 37, No. 2, p. 375-376, April, 1972
3. Sawyers, J. H., "The Maximum Entropy Method Applied to Radar Adaptive Filtering", Proc. of the RADC Spectrum Estimation Workshop, pp. 290-301, 3-5 Oct. 1979



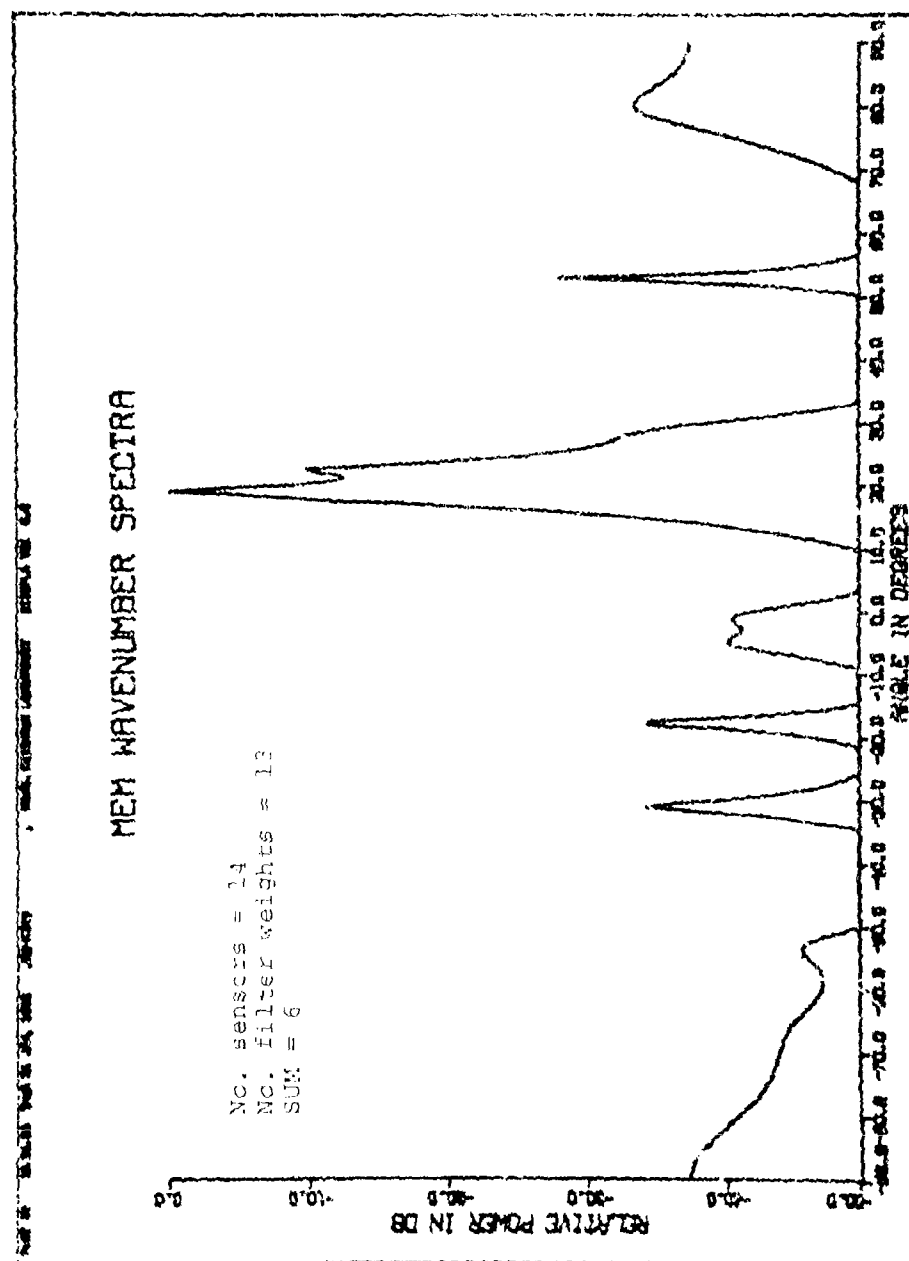
MESA SNAPSHOT WAVENUMBER SPECTRA

Fig. 1



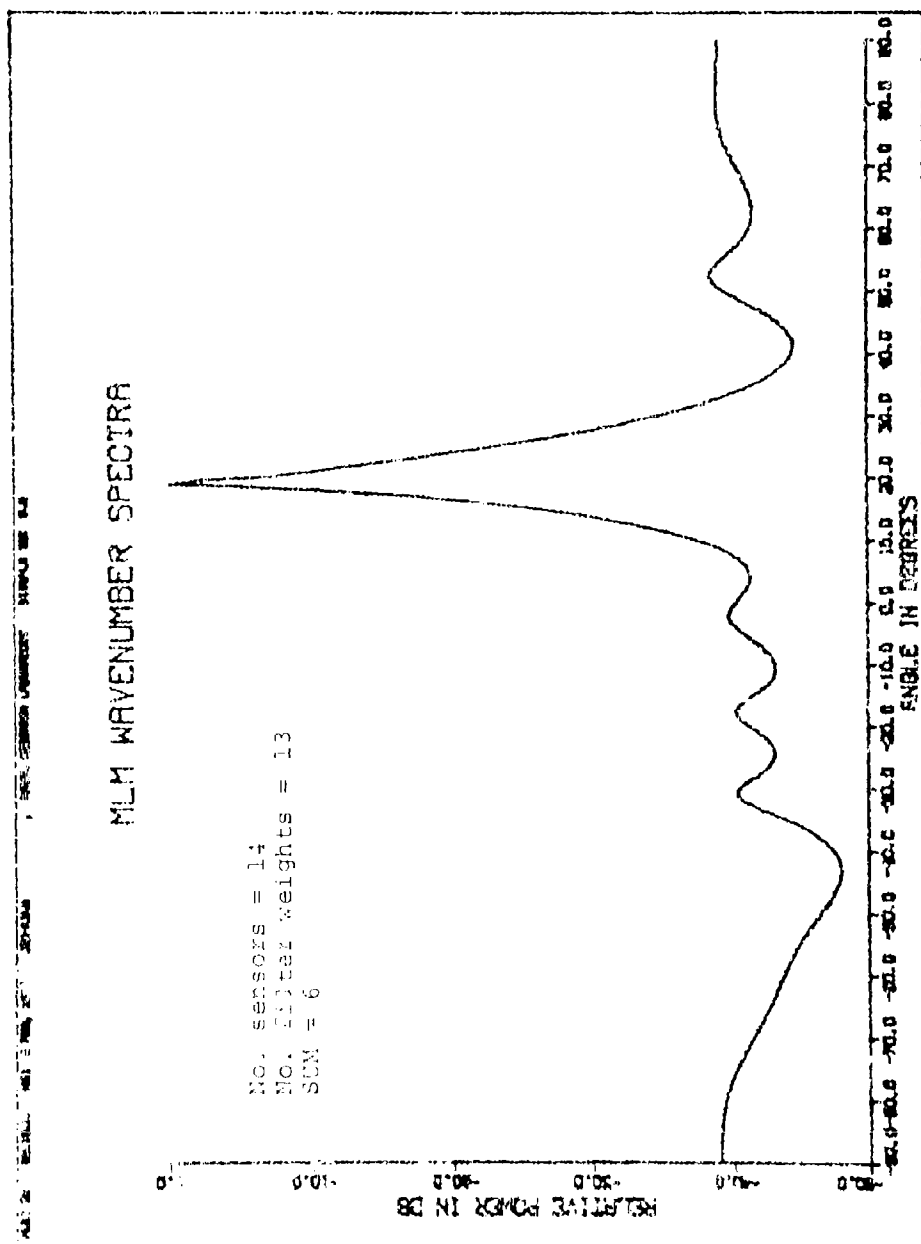
MLM SNAPSHOT WAVENUMBER SPECTRA

Fig. 2



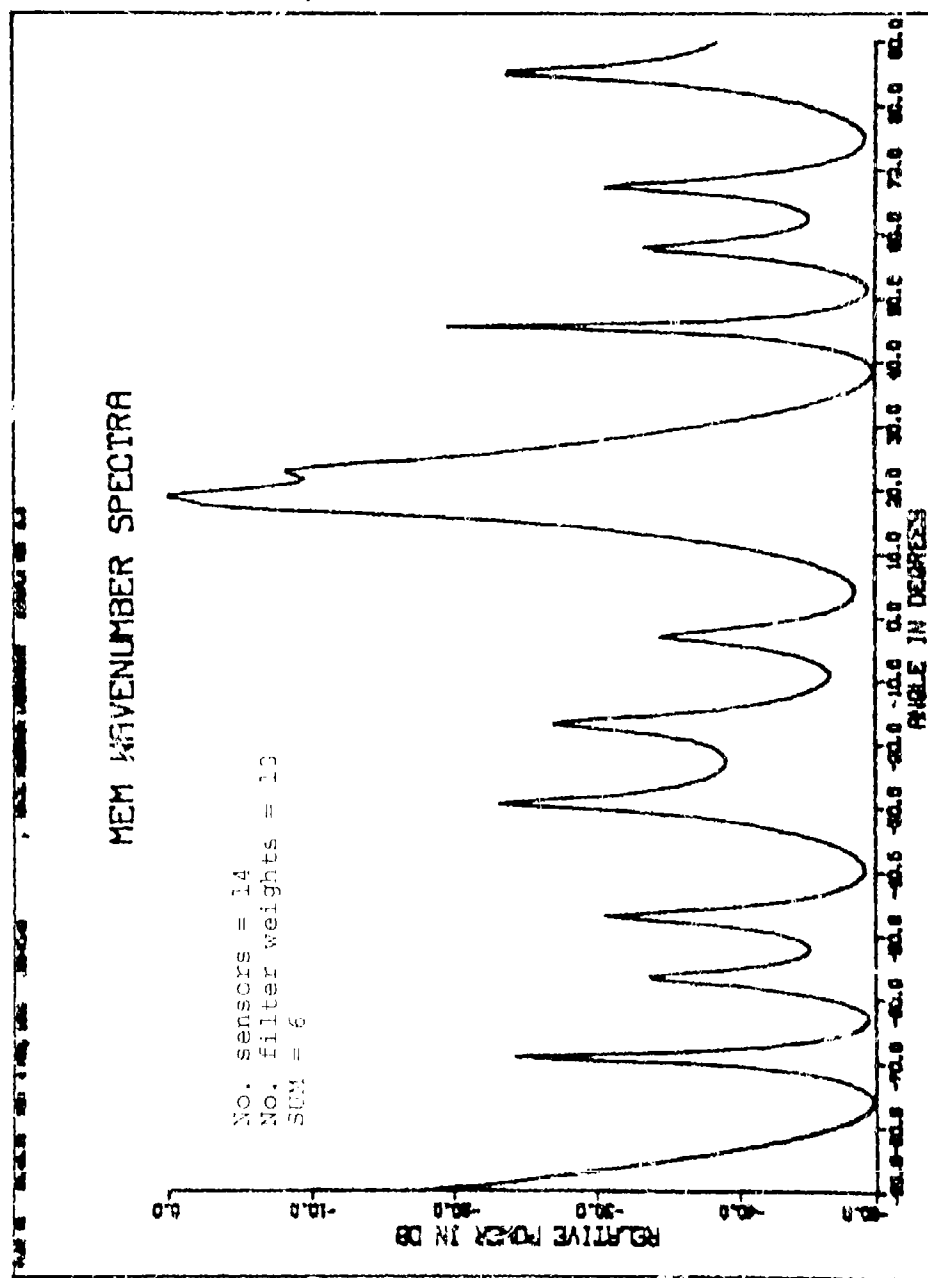
MEM WAVENUMBER SPECTRA (COVARIANCE MATRIX AVERAGED)

Fig. 3



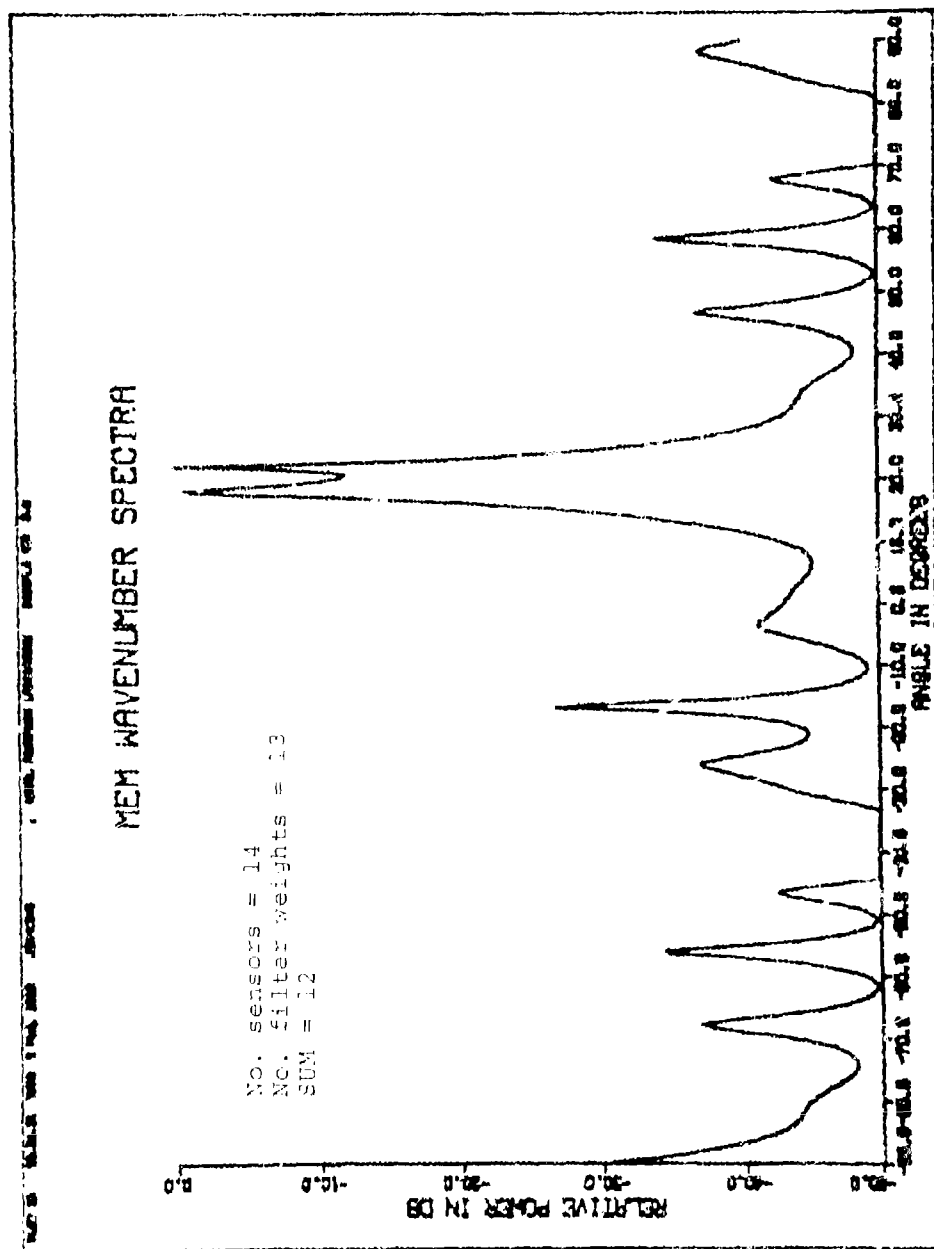
MLM WAVENUMBER SPECTRA (COVARIANCE MATRIX AVERAGED)

Fig. 4



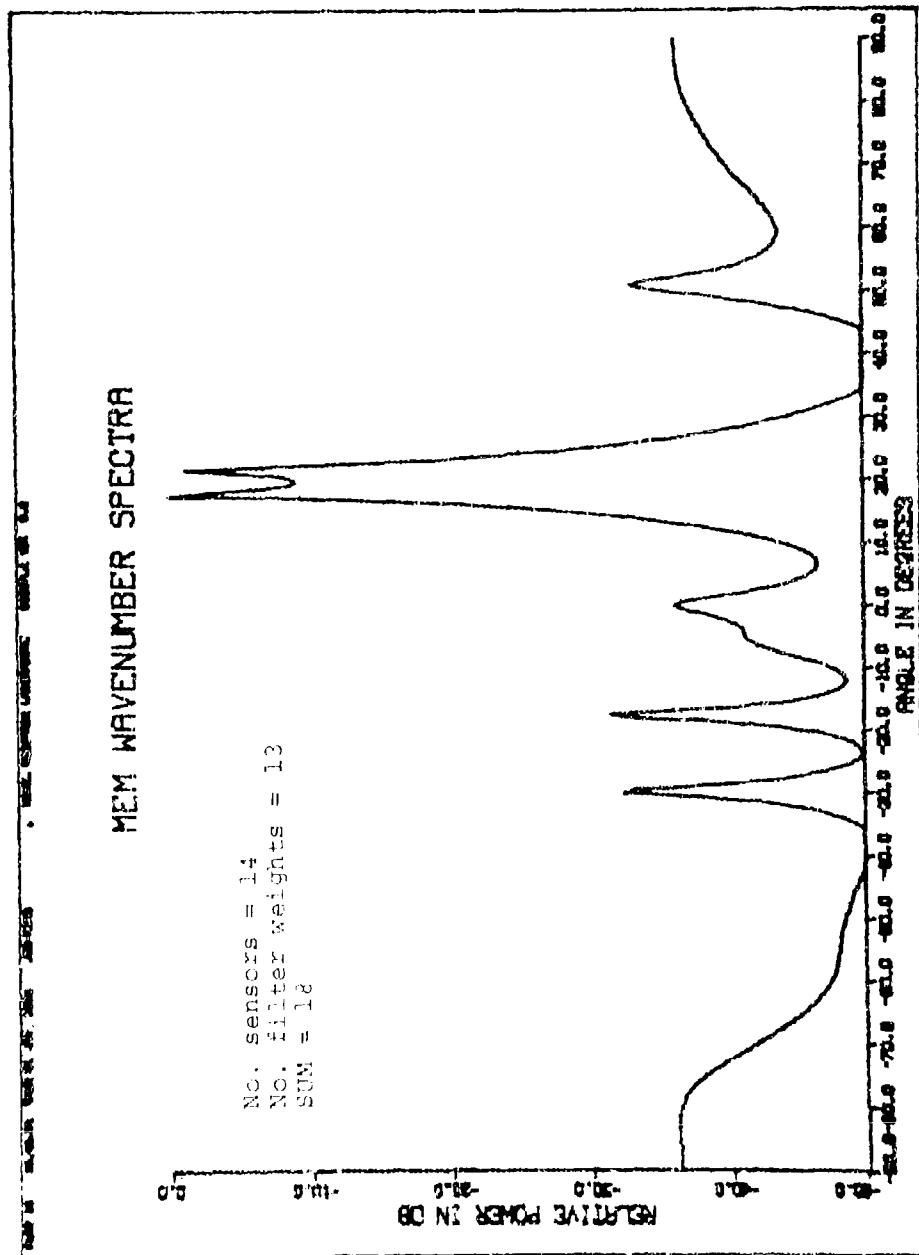
MEM WAVENUMBER SPECTRA (AVERAGED FILTER WEIGHTS)

Fig. 5



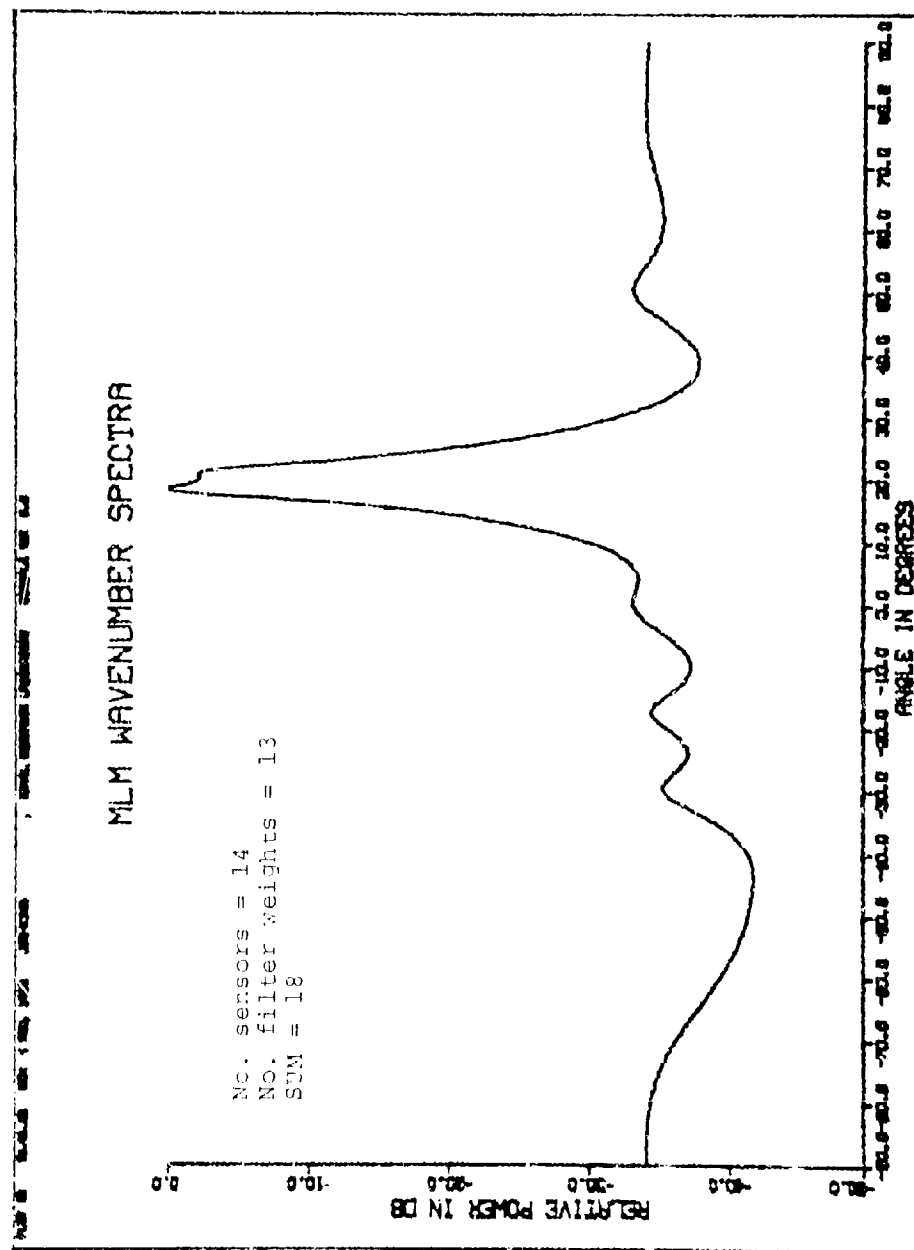
MEM WAVENUMBER SPECTRA (AVERAGED FILTER WEIGHTS)

Fig. 6



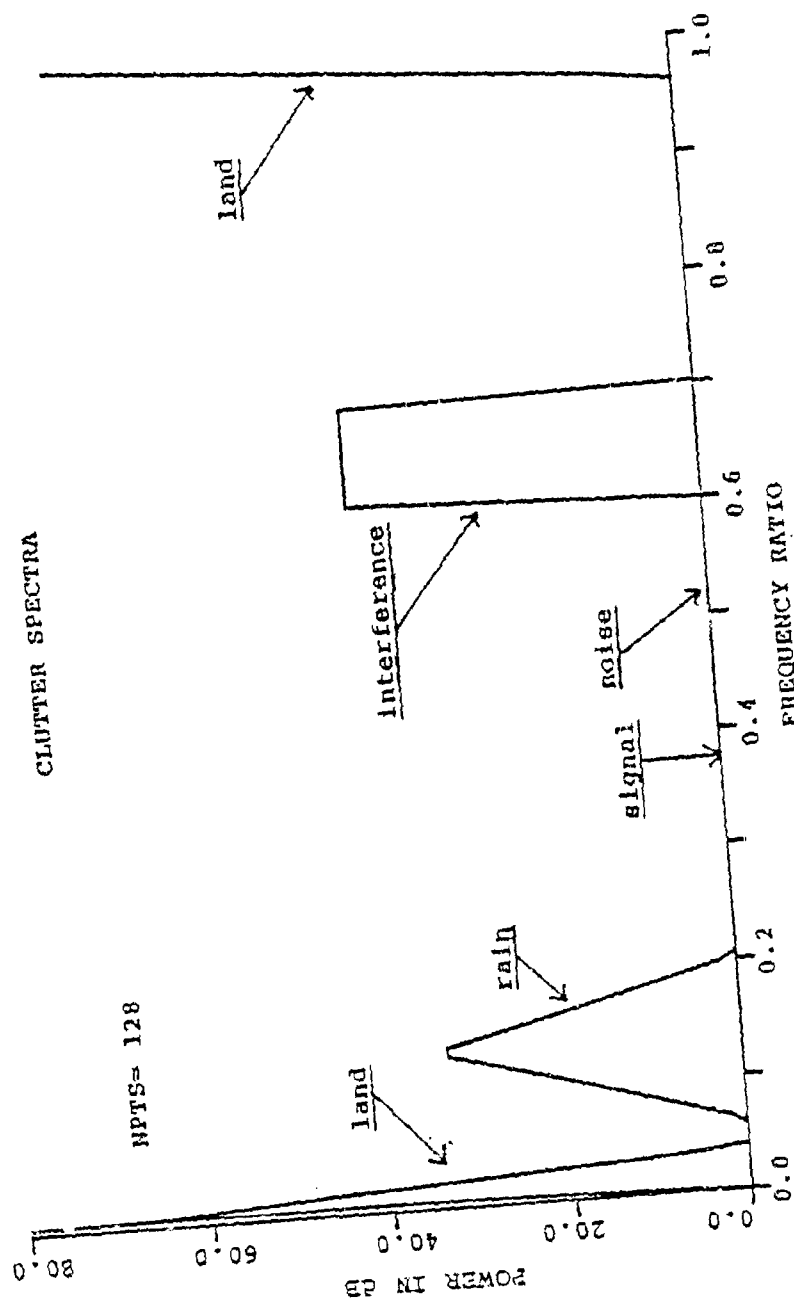
MEM WAVENUMBER SPECTRA (AVERAGED COVARIANCE MATRIX)

Fig. 7



MLM WAVENUMBER SPECTRA (AVERAGED COVARIANCE MATRIX)

Fig. 8



CLUTTER POWER SPECTRAL DENSITY

Figure 9

MESA DETECTOR

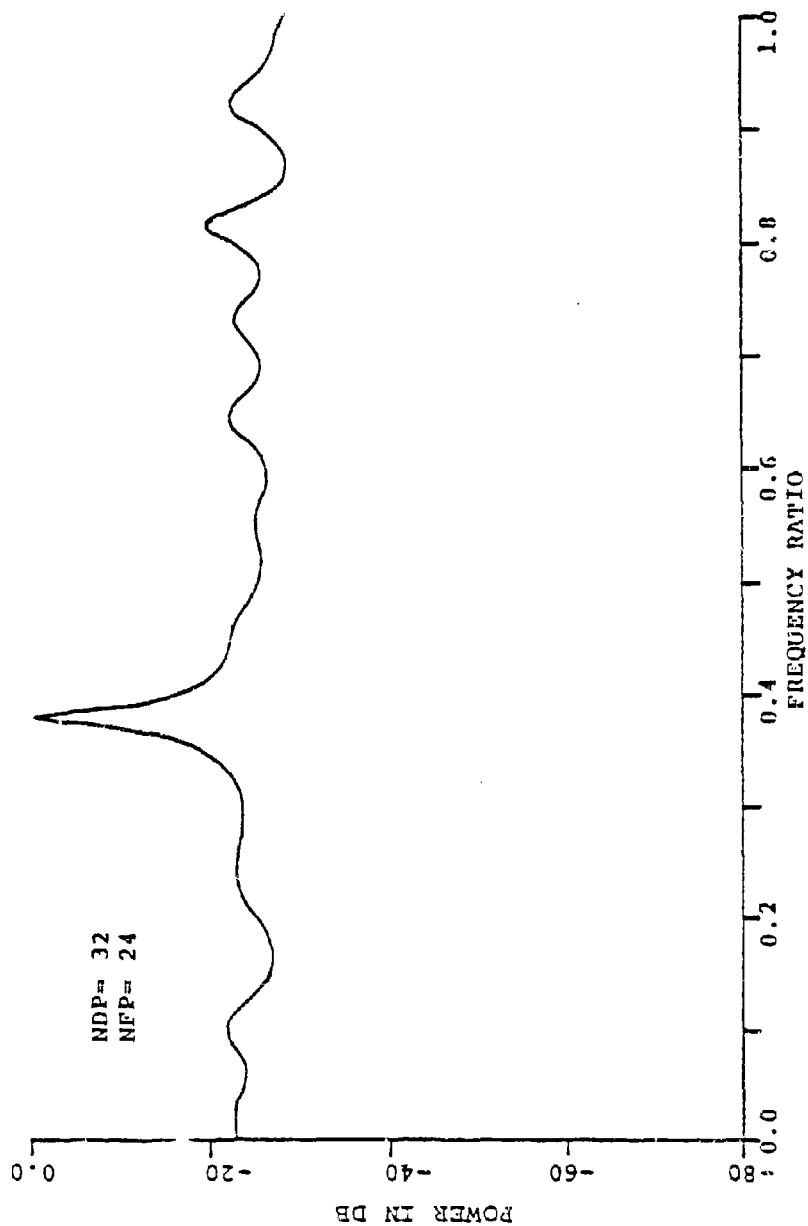


Figure 10

MESA DETECTOR

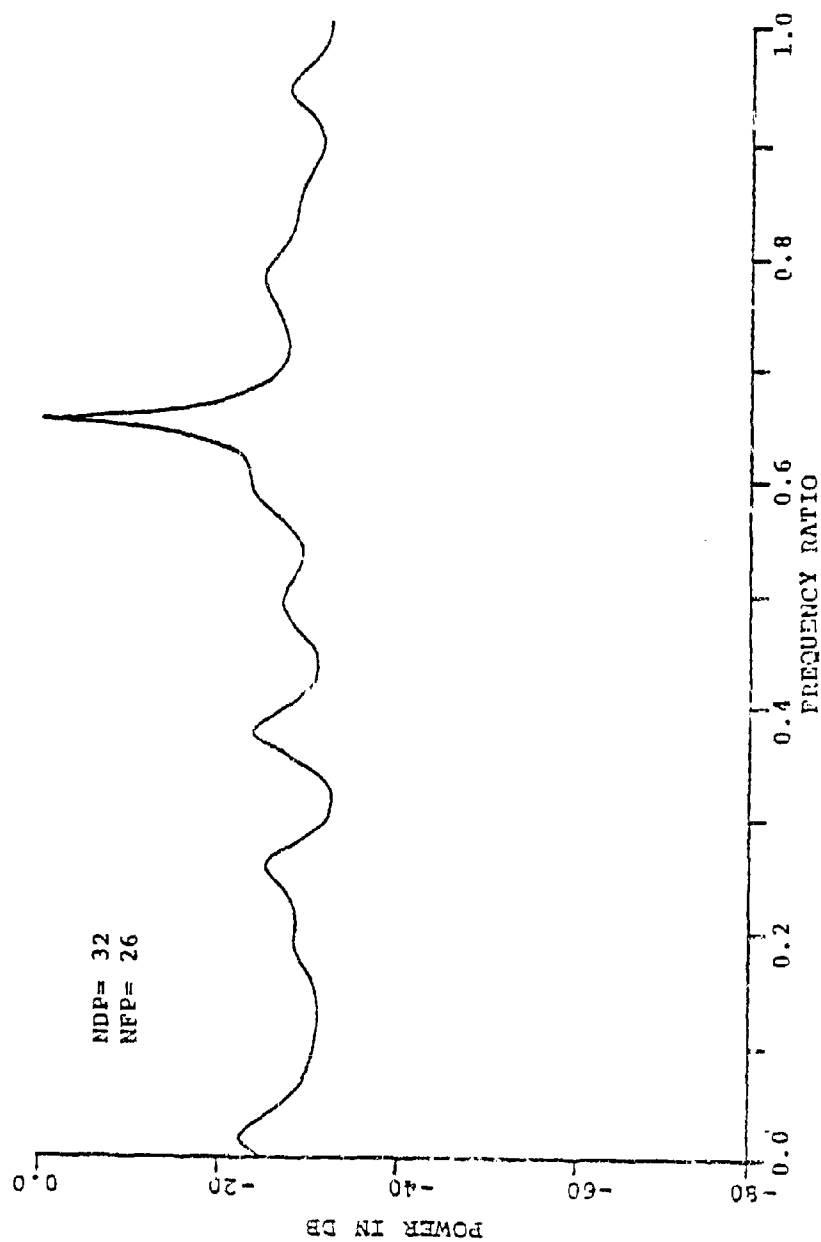


Figure 11

RANDOM DATA SAMPLING

Introduction

Random data sampling may sometimes be a useful sampling technique when estimating power spectra (1). For example, the cost of a large antenna array may be significantly lowered, by reducing the number of antennas (data samples) and intentionally undersampling through the use of a random distribution of antennas. Random data sampling may also be required if data samples necessarily have a random distribution. For example, radar antennas or acoustical sonobouys may be dropped from the air and permitted to fall freely to the ground or water, and land in a random planar distribution.

With use of random data sampling, the side lobes of a Fourier power spectra have a random distribution in both number and location. However, the typical Fourier spectral characteristics such as resolution and side lobe levels may be retained in an average of many such Fourier power spectra computed using random sampling. Useful Fourier power spectra also result from random data sampling even with very sparse (undersampled) data sets.

It is questionable whether random data sampling is effective when the maximum entropy method (MEM) is used to compute an estimated power spectra. Examples of both the Fourier and MEM power spectra are computed using random data sampling to demonstrate the effectiveness of random data sampling with these two power spectra estimation techniques.

Examples of Fourier Antenna Patterns

Fourier antenna patterns may be computed by taking the spatial Fourier transform of signals incident to an antenna array. The Fourier transform of N spatial data points y_n is as follows:

$$X(k) = \frac{1}{N} \sum_{n=1}^N y_n e^{-ikx_n} \quad (1)$$

where y_n is the measured data and k is the signal wavenumber defined as follows:

$$k = (2\pi/\lambda) \sin(\theta)$$

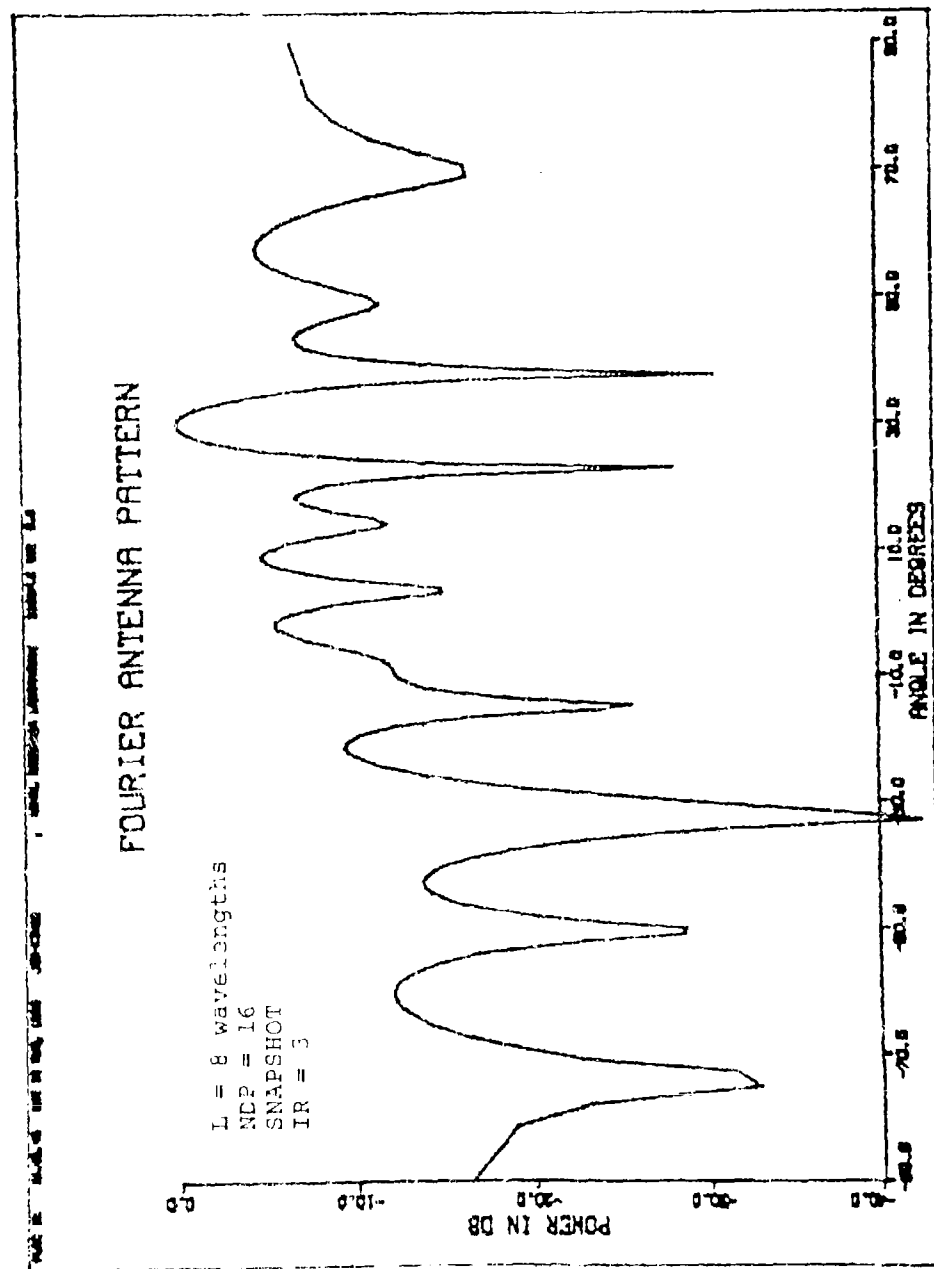
$$y_n = A e^{ik_0 x_n} + \eta e^{i\phi}$$

for $k_0 = (2\pi/\lambda) \sin(\theta_0)$

The amplitude, wavelength, and angle of the incident signal is respectively given by A , λ , and θ . The noise amplitude η has a Gaussian distribution, and the noise phase ϕ has a white distribution. The N array antennas are distributed at positions x_n along a one dimensional axis. In a randomly distributed antenna array the positions x_n are located with equal probability along a line of length L according to a white distribution function.

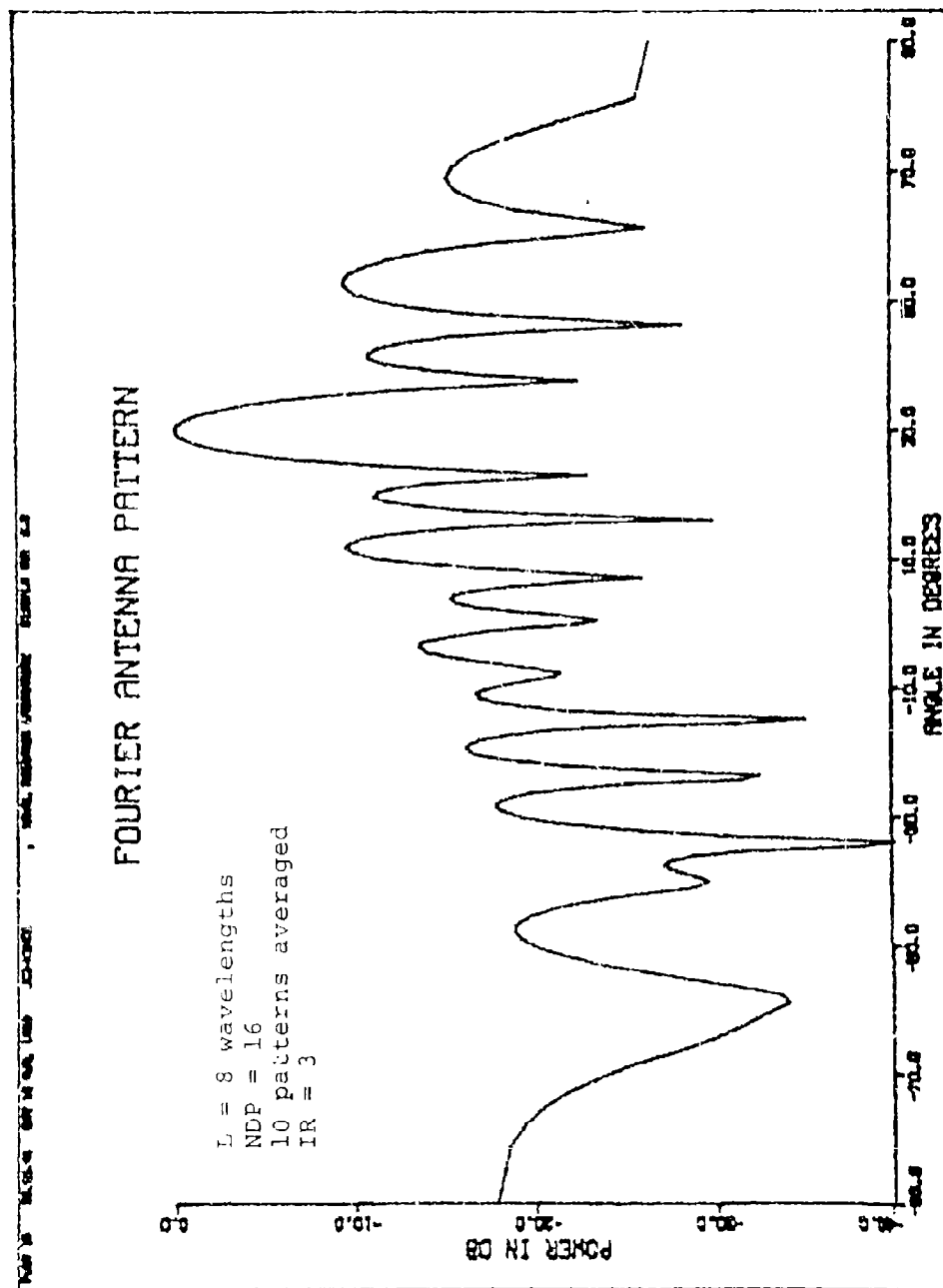
The resulting Fourier antenna patterns, computed using random sampling are shown in Figs. 1-3. In the first example of Fig. 1 a signal is detected with 16 randomly distributed antennas located in a straight line array having a total length of 8 wavelengths. Side lobe structure is noticeably higher than those obtained with half-wavelength sampling. However, in an average of 10 such antenna patterns, the resulting averaged pattern, shown in Fig. 2, has reduced side lobe levels that are about 10 dB below the main lobe. Further averaging of such antenna patterns will result in lower side lobe levels approaching the -13.6 dB minimum level.

The width of the main lobe in examples shown in Figs. 1 and 2 is about the same as the width obtained with half wavelength sampling. Only the antenna pattern side lobe structure is significantly altered when using random data sampling. In a third example an average of 10 antenna patterns is shown in Fig. 3, where each Fourier antenna pattern is computed using a very sparse data set consisting of only 4 data samples, which are randomly distributed over a single dimension of 8 wavelengths in length. The re-



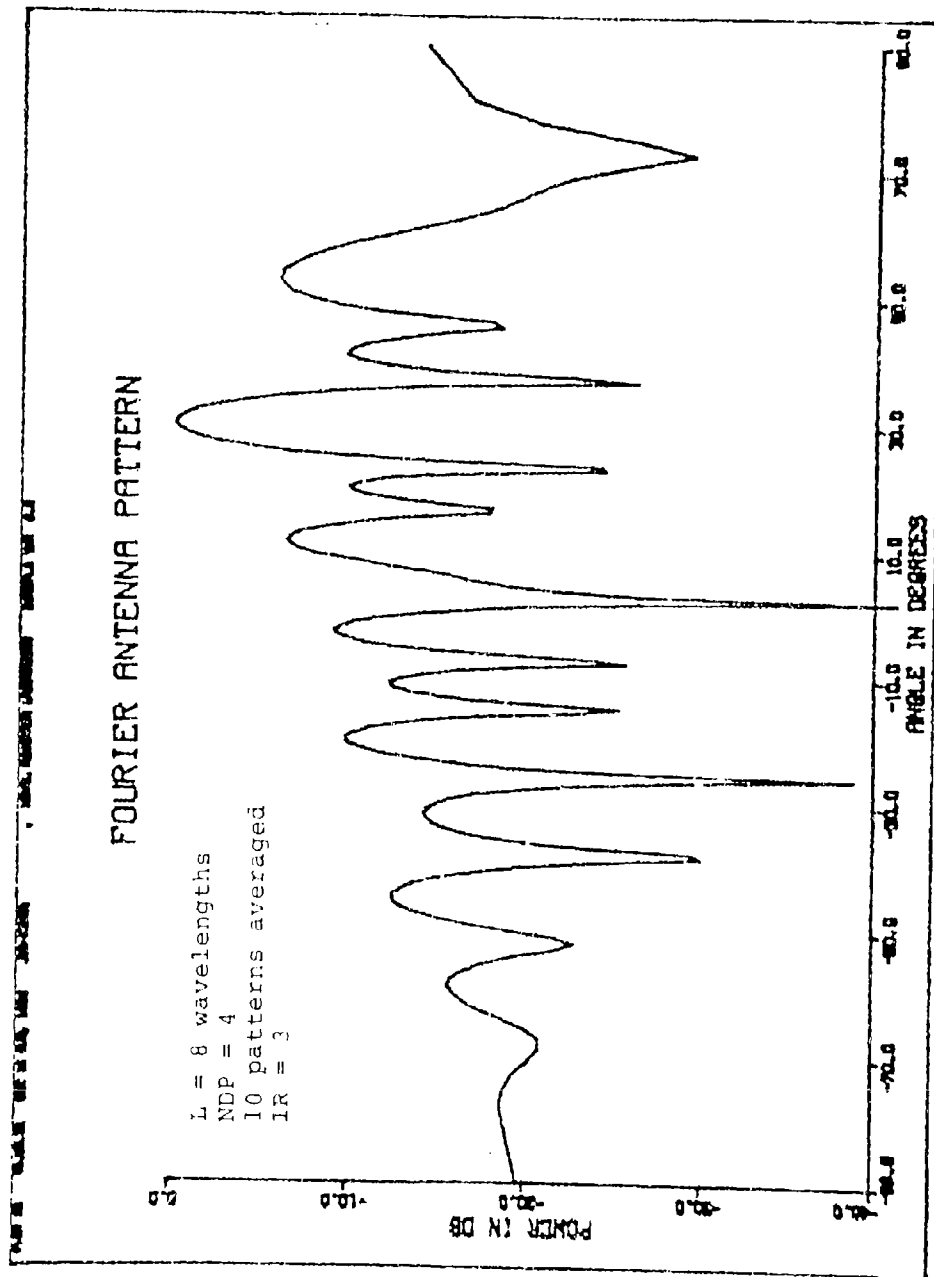
ONE SIGNAL AT 30 DEGREES
RANDOMLY LOCATED ANTENNAS

Fig. 1



ONE SIGNAL AT 30 DEGREES
 ANTENNAS LOCATED RANDOMLY

Fig. 2



RANDOMLY LOCATED ANTENNAS
ONE SIGNAL AT 30 DEGREES

Fig. 3

sultant averaged antenna pattern is surprisingly good, when it is considered that the detected signal is undersampled by a factor of four.

Examples of MEM Wavenumber Patterns

Because the maximum entropy method may be derived using the discrete Wiener prediction filter (2), it is unlikely that meaningful data predictions are possible with random data sampling. For example a predicted signal \hat{x}_m is given by the discrete convolution as follows:

$$\hat{x}_m = \sum_{n=1}^N b_n x_{m-n} \quad (3)$$

where the data set x_m must be a set of uniformly sampled data. If only a relatively small number of data samples are missing, then eqn. 3 still may provide useful predicted data from which the prediction error may be minimized. However, if the entire data set is obtained using random sampling, then the data set \hat{x}_m predicted using eqn. 3, is not expected to be very meaningful. Since the prediction filter b_n is derived from a minimum error derived with eqn. 3, the prediction filter b_n may also be an inefficient filter if the data set x_m is derived using random data sampling.

The MEM all-pole wavenumber spectra formulation does not present any apparent problem with use of random data sampling, since the MEM wavenumber spectra formulation contains only a discrete Fourier transform of the prediction filter b_n as indicated:

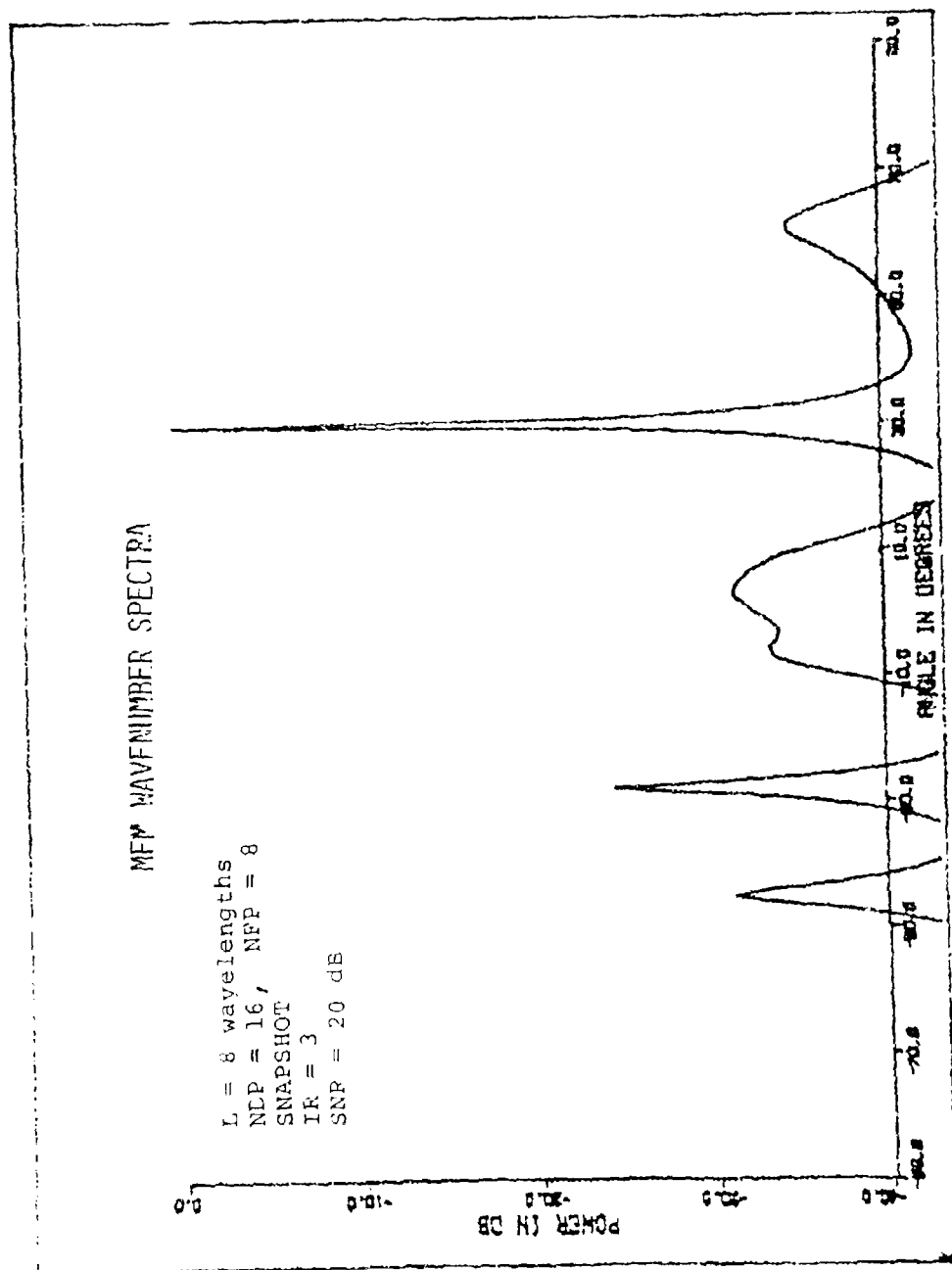
$$P(k) = (P_N/k) / \left| 1 - \sum_{n=1}^N b_n e^{-ikx_n} \right|^2 \quad (4)$$

However, since the prediction filter b_n is likely to be in error, the MEM power spectra as given by eqn. 4 may also not be very meaningful when computed using random data sampling. Examples of MEM wavenumber spectra are demonstrated in Figs. 4-6, where the first example is a MEM snapshot wavenumber spectra computed with uniform data sampling. Other MEM wavenumber spectra shown are

are computed using random data sampling.

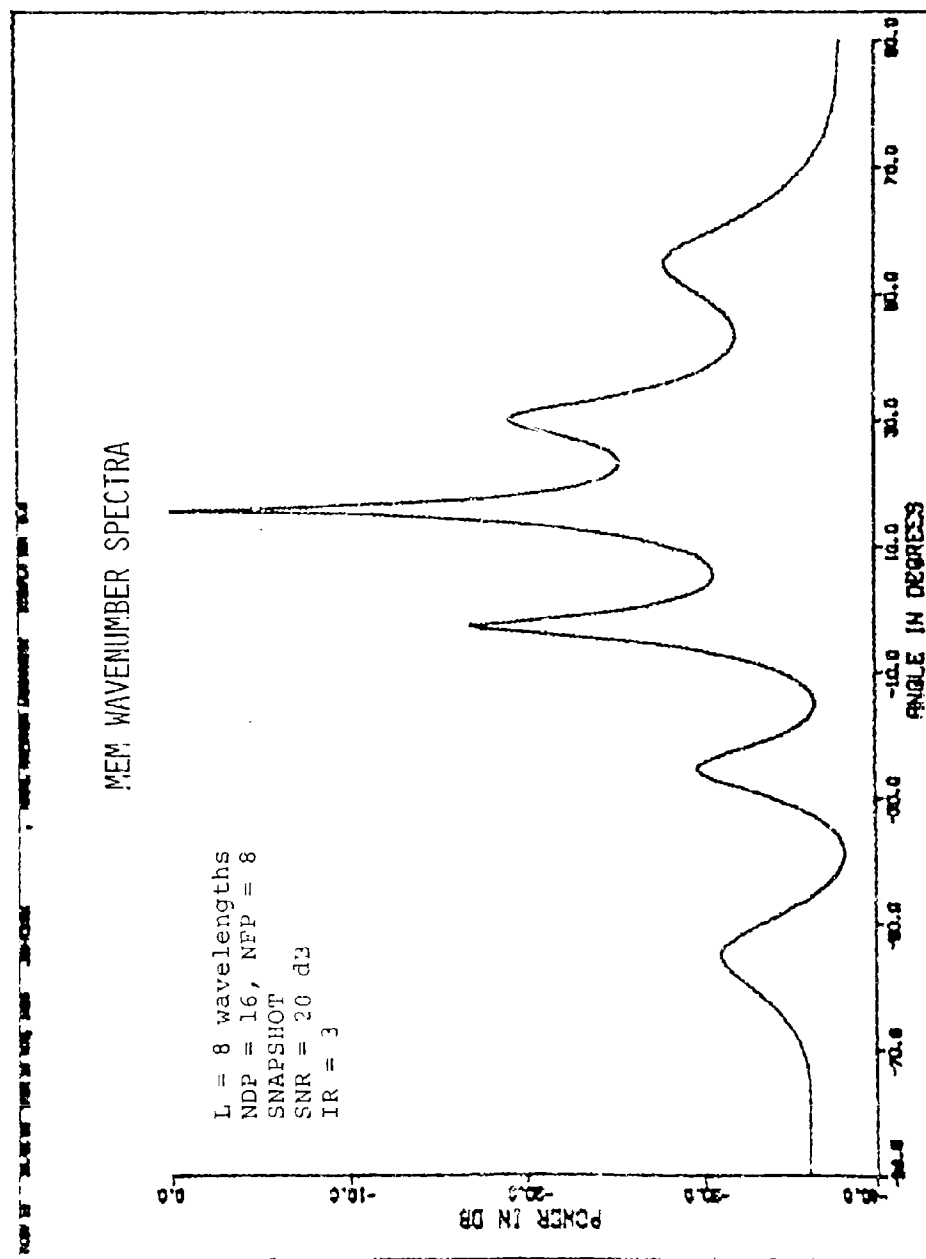
The signal is accurately detected in Fig. 4 by an 8 wavelength linear antenna array having uniform half-wavelength antenna spacing. The MEM wavenumber spectra shown in Fig. 5 is computed using 16 antennas randomly spaced along a straight line that is 8 wavelengths long. While both snapshot wavenumber spectra shown in Figs. 4 and 5 are computed for a signal incident to the antenna array at 30 degrees and with SNR of 20 dB, only the MEM spectra computed with uniform half-wavelength sampling accurately detects the signal. The MEM wavenumber spectra shown in Fig. 5 indicates that a signal is detected at about 16 degrees. Other MEM spectra computed with random data sampling (not shown) also contained similar false alarms. An average of 6 such MEM wavenumber spectra, where each spectra is computed using random data sampling, is shown in Fig. 6. Even though 16 antennas are located randomly along a straight line having a length of 8 wavelengths, neither the individual 6 computed spectra or the average spectra indicated a signal detection in a 6 degree window about the signal angle of 30 degrees. The averaged MEM wavenumber spectra shown in Fig. 6 contains only false alarm peaks.

As anticipated, the MEM wavenumber spectra computed using random data sampling are not useful spectra, since MEM does require the use of uniform data sampling at minimal half-wavelength intervals. Of course if it is possible to obtain accurate estimates of a uniformly spaced data set using some extrapolation method, then useful MEM spectra could conceivably be computed from a random data set. It is doubtful that any useful spectral estimates can be obtained with any spectral estimation technique based upon the prediction filter, if random data sampling is utilized. However conventional Fourier spectral estimation techniques do provide useful spectra using randomly sampled data.



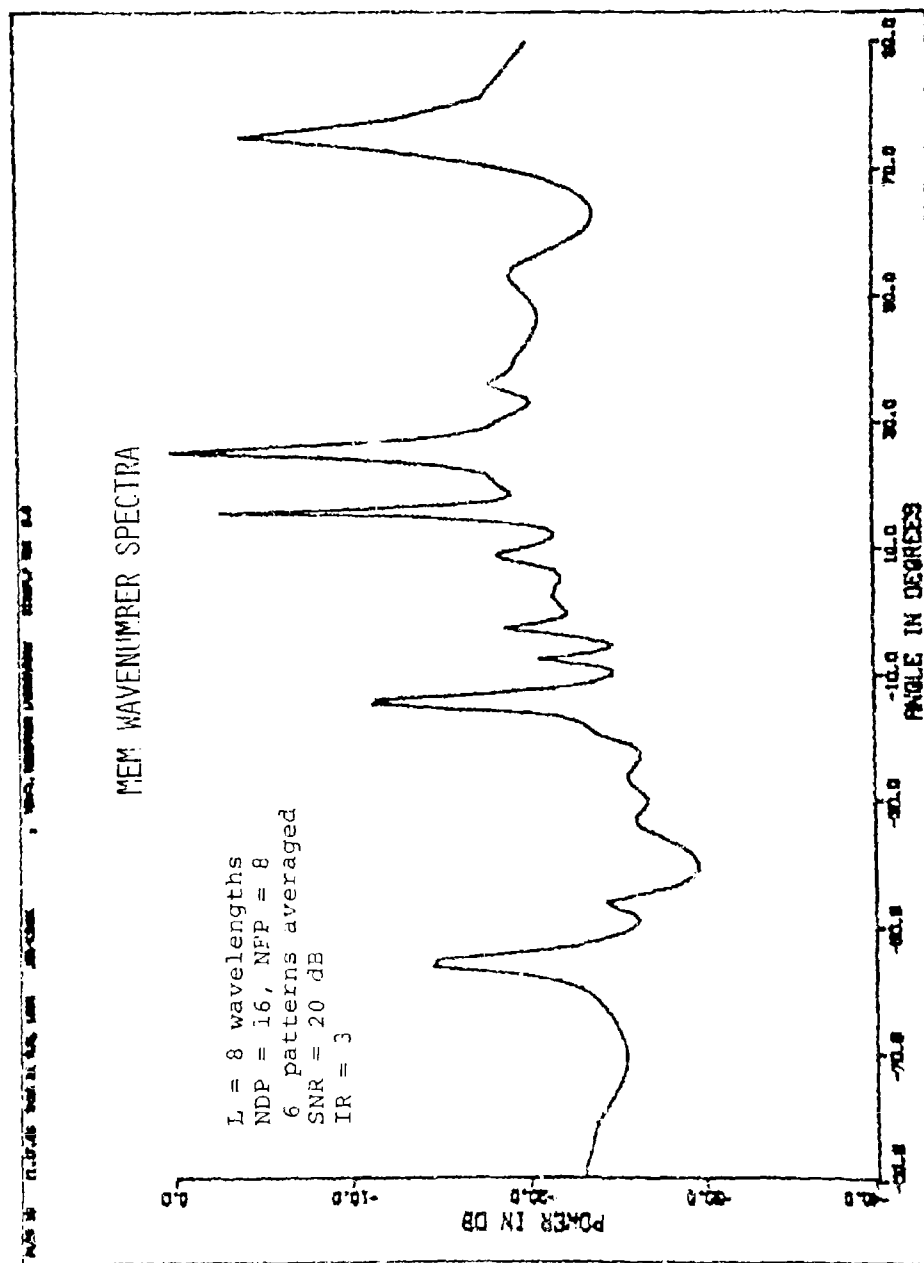
UNIFORM ANTENNA SPACING
ONE SIGNAL AT 30 DEGREES

Fig. 4



RANDOMLY LOCATED ANTENNAS
ONE SIGNAL AT 30 DEGREES

Fig. 5



RANDOMLY LOCATED ANTENNAS
ONE SIGNAL AT 30 DEGREES

Fig. 6

THE W-K SPECTRAL ESTIMATION TECHNIQUE

Introduction

The maximum entropy spectral analysis (MESA) technique and the autoregressive (AR) spectral analysis technique are both limited in accuracy and stability by increasingly noisy data. The MESA and AR techniques may be unnecessarily noise limited due to the definition of the Wiener prediction error, which is minimized in both techniques. It has been noted (1) that the conventional definition of the prediction error actually contains two error components. One error component is the actual prediction error inherent in the predicted data set \hat{x}_m consisting of M data points. The other component error is the noise present in the actual M data samples x_m .

The prediction error may be redefined so that there is only one error component, i.e. the inherent prediction error. By redefining the prediction error, it is anticipated that spectral estimation accuracy and stability of the resulting spectral estimator will be substantially improved at the lower signal-to-noise power levels. The resultant, new, spectral estimation technique is referred to as the Wiener-King (W-K) spectral estimator.

Prediction Error Definition

The conventional definition for the time dependent prediction error e_m is as follows:

$$e_m = x_m - \hat{x}_m \quad \text{for } (m=1, M) \quad (1)$$

where there are M data samples x_m and M predicted data points \hat{x}_m . The predicted data points are defined as follows:

$$\hat{x}_m = \sum_{n=1}^N a_n x_{m-n} \quad \text{for } N < M \quad (2)$$

where there are N prediction filter coefficients a_n ($n=1, N$).

The conventional prediction error e_m is a function of the noisy data as well as the predicted data. The data noise may be readily eliminated by redefining the prediction error as a function of noise free spectral components. A spectral component y_m^p , which has frequency f_p is defined by the exponential function as follows:

$$y_m^p = e^{i2\pi f_p m(\Delta t)} \quad (3)$$

The "new" noise free prediction error e_m^p is defined as follows:

$$e_m^p = y_m^p - \hat{x}_m$$

$$e_m^p = e^{i2\pi f_p m(\Delta t)} - \sum_{n=1}^N a_n x_{m-n} \quad (4)$$

The "new" prediction error contains only one error component, which is the inherent error present in the prediction function \hat{x}_m . A total mean squared prediction error may be computed by summing the time dependent squared error computed for all M predicted data points.

Prediction Filter

A "new" prediction filter may be defined by minimizing a redefined total mean squared prediction error. A total mean squared prediction error E_N^p may be defined as follows:

$$e_m^p = y_m^p - \hat{x}_m$$

$$e_m^p (e_m^p)^* = (y_m^p - \hat{x}_m) \cdot (y_m^p - \hat{x}_m)^*$$

$$= y_m^p (y_m^p)^* - \hat{x}_m (y_m^p)^* - \hat{x}_m^* y_m^p + \hat{x}_m \hat{x}_m^* \quad (5)$$

$$E_N^p = (1/(2M+1)) \sum_{m=-M}^M e_m^p (e_m^p)^* \quad (6)$$

The total mean squared prediction error is expressed in detail by combining eqns. (5) and (6) as follows:

$$E_N^P = \left[1/(2M+1) \right] \left[\sum_{m=-M}^M y_m^P (y_m^P)^* - \sum_{n=1}^N a_n \sum_{m=-M}^M x_{m-n} (y_m^P)^* - \sum_{n=1}^N a_n^* \sum_{m=-M}^M x_{m-n}^* y_m^P + \sum_{k=1}^N \sum_{n=1}^N a_n a_k^* \sum_{m=-M}^M x_{m-n} x_{m-k}^* \right] \quad (7)$$

By utilizing the definition of the autocorrelation and cross-correlation functions, expression (7) is simplified as follows:

$$E_N^P = r_y^P - \sum_{n=1}^N a_n r_{xy}^P(n) - \sum_{n=1}^N a_n^* r_{yx}^P(n) + \sum_{k=1}^N \sum_{n=1}^N a_n a_k^* r_x(k-n) \quad (8)$$

where the autocorrelation of function y^P is r_y^P , the autocorrelation of function x is r_x , and the crosscorrelation of the functions y^P and x is r_{xy} and r_{yx} .

The total mean squared prediction error may be minimized with respect to the unknown filter coefficients a_n as follows:

$$\frac{\partial E_N^P}{\partial a_n^*} = -r_{yx}^P(n) + \sum_{n=1}^N a_n r_x(n-n) = 0 \quad (9)$$

where $n = 1, N$.

The resultant expression eqn. (9) is a set of N equations that may be simultaneously solved for the N filter coefficients. The N equations may be written as follows:

It is necessary to solve eqn. (13) for all coefficients (a_1, a_2, \dots, a_N) for every spectral component f_p of interest. However it is possible to determine spectral regions of interest by simply computing the crosscorrelation vectors r_{yx}^p at every frequency f_p . In this way it is necessary only to solve for the prediction filter coefficients in spectral regions where the crosscorrelation vectors indicate a strong correlation.

Power Spectra

Consider another prediction error ϵ_m which is defined to include the unknown signal amplitude A_p , i.e.

$$\epsilon_m = A_p e_m^p \quad (14)$$

$$\epsilon_m = A_p [y_m^p - \hat{x}_m]$$

$$\epsilon_m = A_p \left[y_m^p - \sum_{n=1}^N a_n x_{m-n} \right] \quad (15)$$

The Fourier transform of eqn. (15) results in an expression for the spectral amplitude A_p as follows:

$$\xi(f) = A_p \left[\delta(f-f_p) - \sum_{n=1}^N a_n e^{-i2\pi f n \Delta t} \right]$$

$$A_p = \frac{\xi(f_p)}{\left[1 - X(f_p) \sum_{n=1}^N a_n e^{-i2\pi f_p n \Delta t} \right]} \quad (16)$$

The power spectra $P(f_p)$ is given by the following expression:

$$P(f) = A_p \cdot A_p^*$$

$$P(f_p) = \frac{\xi^2(f_p)}{\left| 1 - X(f_p) \sum_{n=1}^N a_n e^{-i2\pi f_p n(\Delta t)} \right|^2} \quad (17)$$

where $\xi(f)$, which is the Fourier transform of the prediction error ϵ_m , may be evaluated in the spectral region void of signals, i.e. $f \neq f_p$. For the present it is useful to consider the all pole representation of the W-K power spectral technique by evaluating the ratio of $P(f_p)/\xi^2(f_p)$.

It is anticipated that the W-K all pole power ratio spectra computed with eqn. (17) will be more stable but just as accurate as comparative spectra computed with MESA. The formulation of the W-K spectral estimator as given by eqn. (17) differs from that of MESA in that the Fourier transform $X(f_p)$ of the data set is utilized as indicated in eqn. (17). Of course the prediction filter coefficients a_n are different from the prediction coefficients used in MESA.

The presence of the data transfer function $X(f_p)$ is a stabilizing factor in the power spectral eqn. (17). Spectral resolution and accuracy of the W-K spectral estimator are expected to be comparable to similar characteristics of MESA, since both spectral estimation methods have a similar all pole formulation. However the W-K spectral estimator is expected to have better stability and whiter spectra than that obtainable with use of the MESA technique.

Example Wavenumber Power Spectra

A W-K wavenumber power spectra may be obtained from eqn. (17) by introducing the wavenumber k and spatial dimension x with aid of the variable relationships that follow:

$$k = V (2\pi f)$$

$$x = V t$$

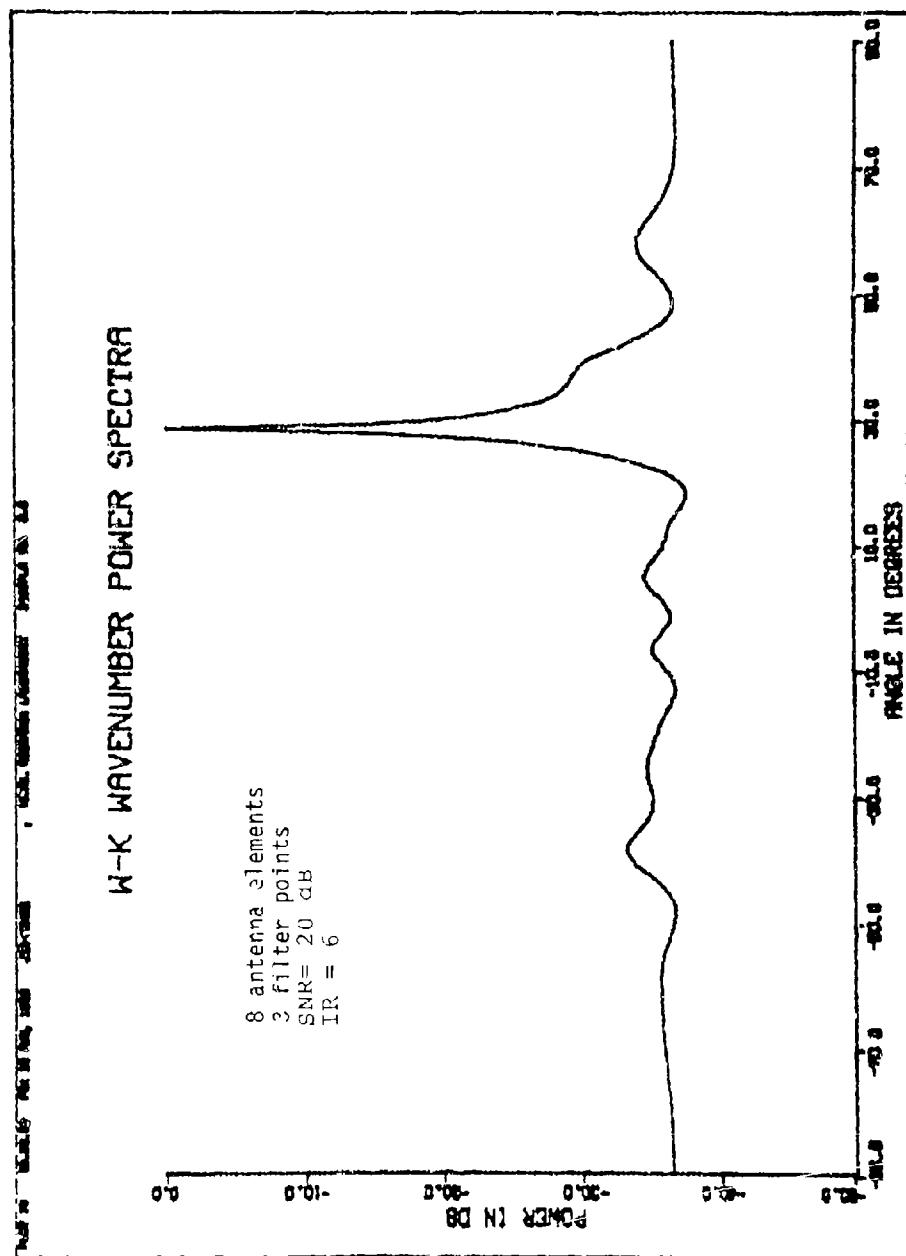
where V is the wave velocity. With the indicated change of

variables, examples of W-K wavenumber power spectra are computed for only a few simple signal and noise conditions. At this time the W-K spectral estimation technique is evaluated only to indicate that the W-K spectral estimator is a viable and useful method for obtaining stable, high resolution spectral estimations with only a single (snapshot) set of data.

A single signal is shown detected at 28.5 degrees in Fig. 1 using a 181 point W-K wavenumber power (ratio) spectra as given by eqn. (17). The simulated signal is actually incident to an 8 element linear antenna array at an angle of 30 degrees and with an SNR of 20 dB. The W-K spectrum shown in Fig. 1 is computed using only 3 filter coefficients. The snapshot spectra is well whitened by the W-K estimation technique although the signal location is imprecise with an error of 1.5 degrees. The same signal and noise model is used to obtain another W-K wavenumber spectra using 4 filter coefficients as shown in Fig. 2. Again the W-K spectra is well whitened, and again the signal peak is located with the same imprecision. A comparison of these two initial W-K spectra indicate a smaller filter size may provide better noise suppression by almost 10 dB in the examples given.

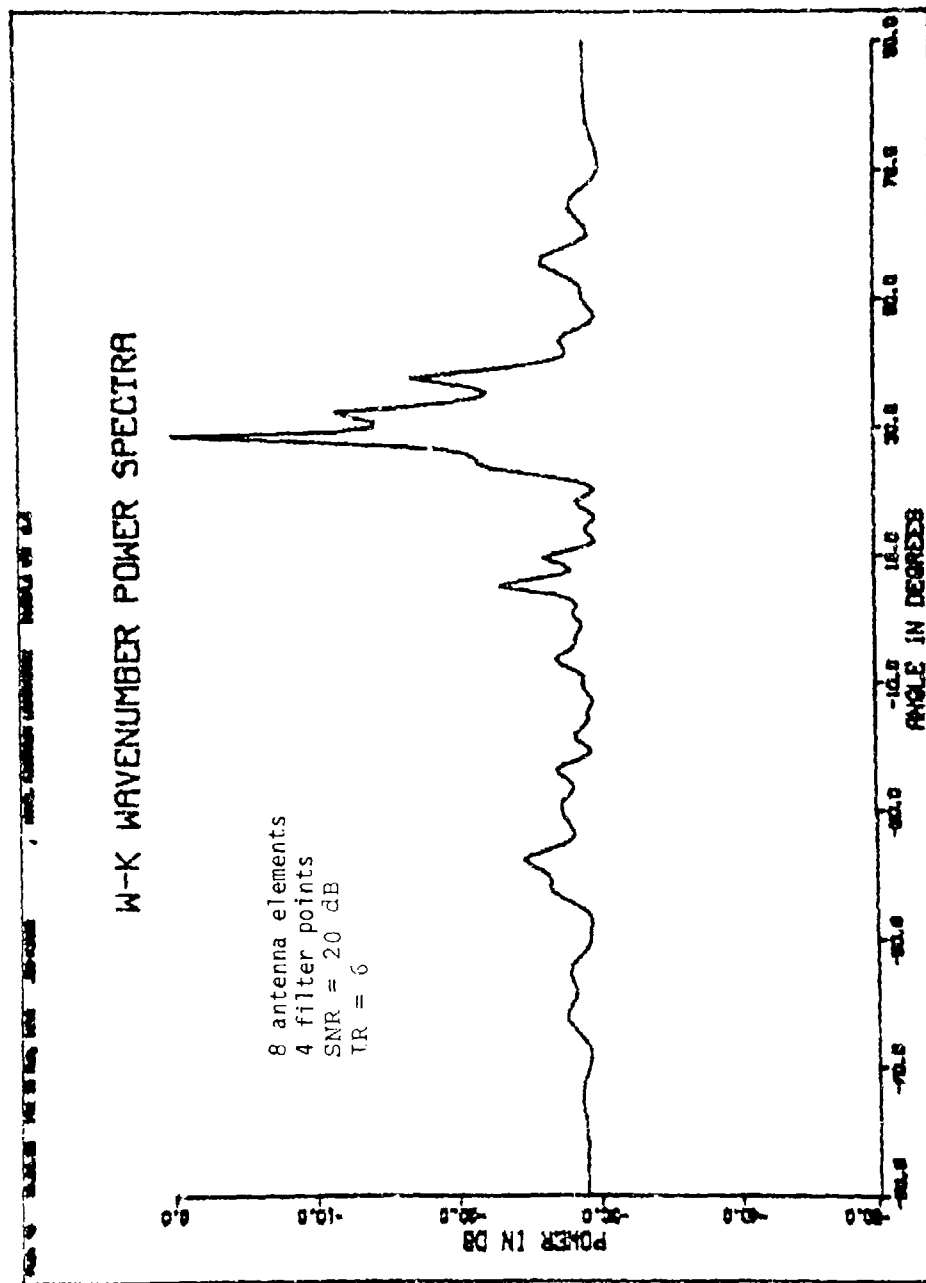
For comparison a MESA wavenumber spectra is computed for the same signal and noise model used in the two W-K spectra examples. However five filter coefficients are used in the computed MESA example to better illustrate the large noise peaks that frequently appear in MESA snapshot spectra. It should be noted that whitened spectra do result when MESA is applied to covariance matrix data that has been averaged over several snapshots of data. The example MESA wavenumber spectra is shown in Fig. 3, where indeed 5 large peaks appear in the spectrum, but only the peak located at about 31.5 degrees is representative of the signal.

In another example two signals incident to the antenna array at -30 and 30 degrees are shown correctly detected by the W-K spectral estimator in Fig. 4. The overall W-K spectra is well whitened with use of 5 filter coefficients. For comparison



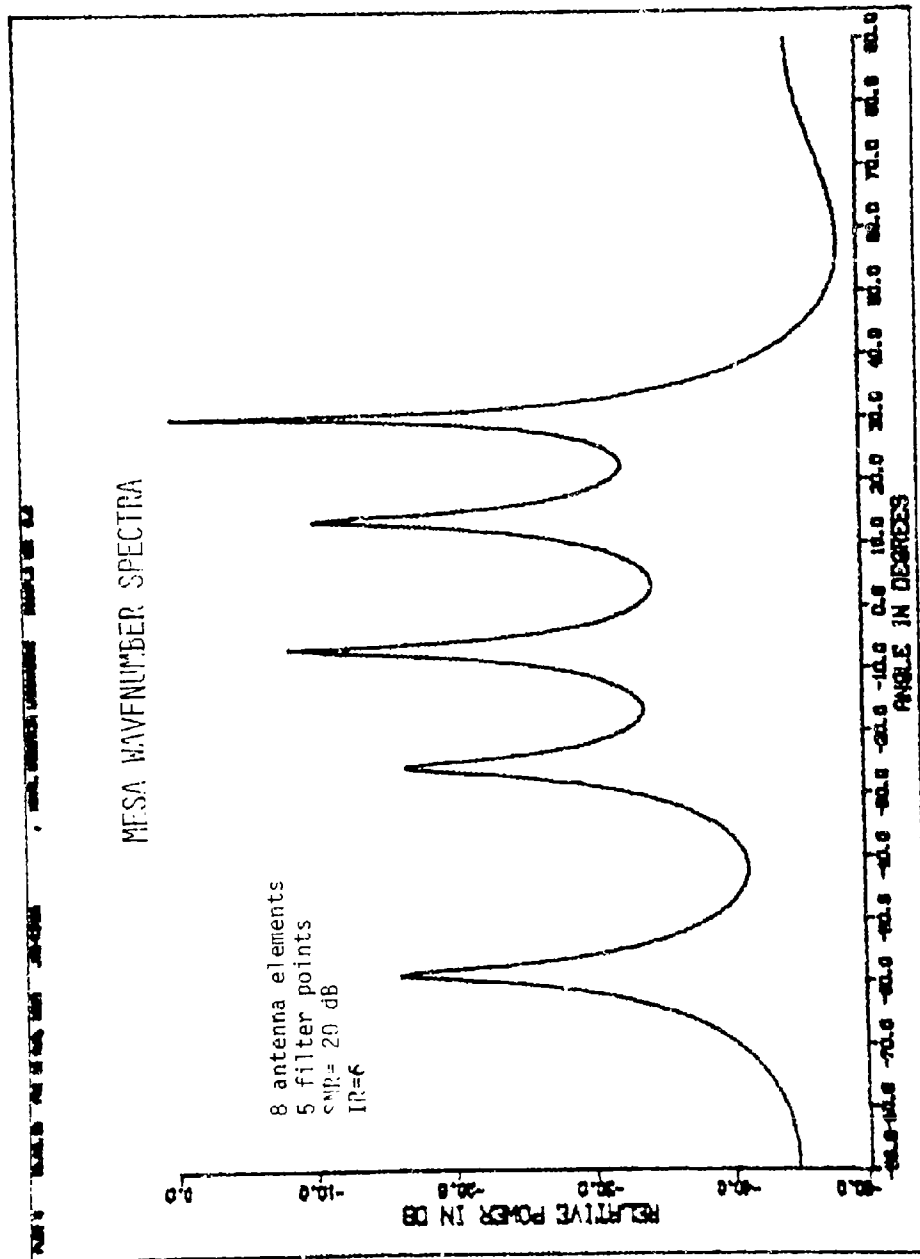
ONT SIGNAL AT 30 DEGRE

Fig. 1



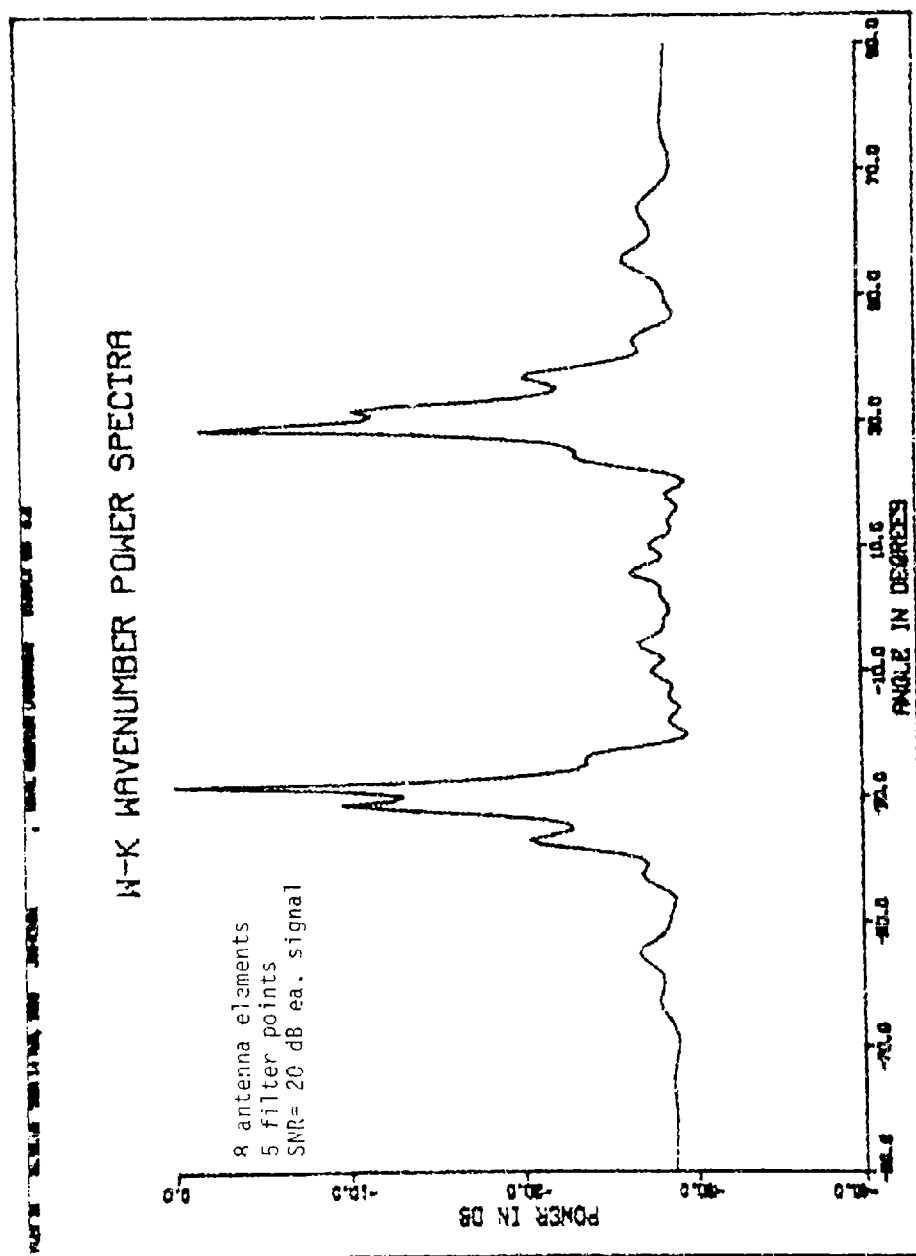
ONE SIGNAL AT 30 DEGREES

Fig. 2



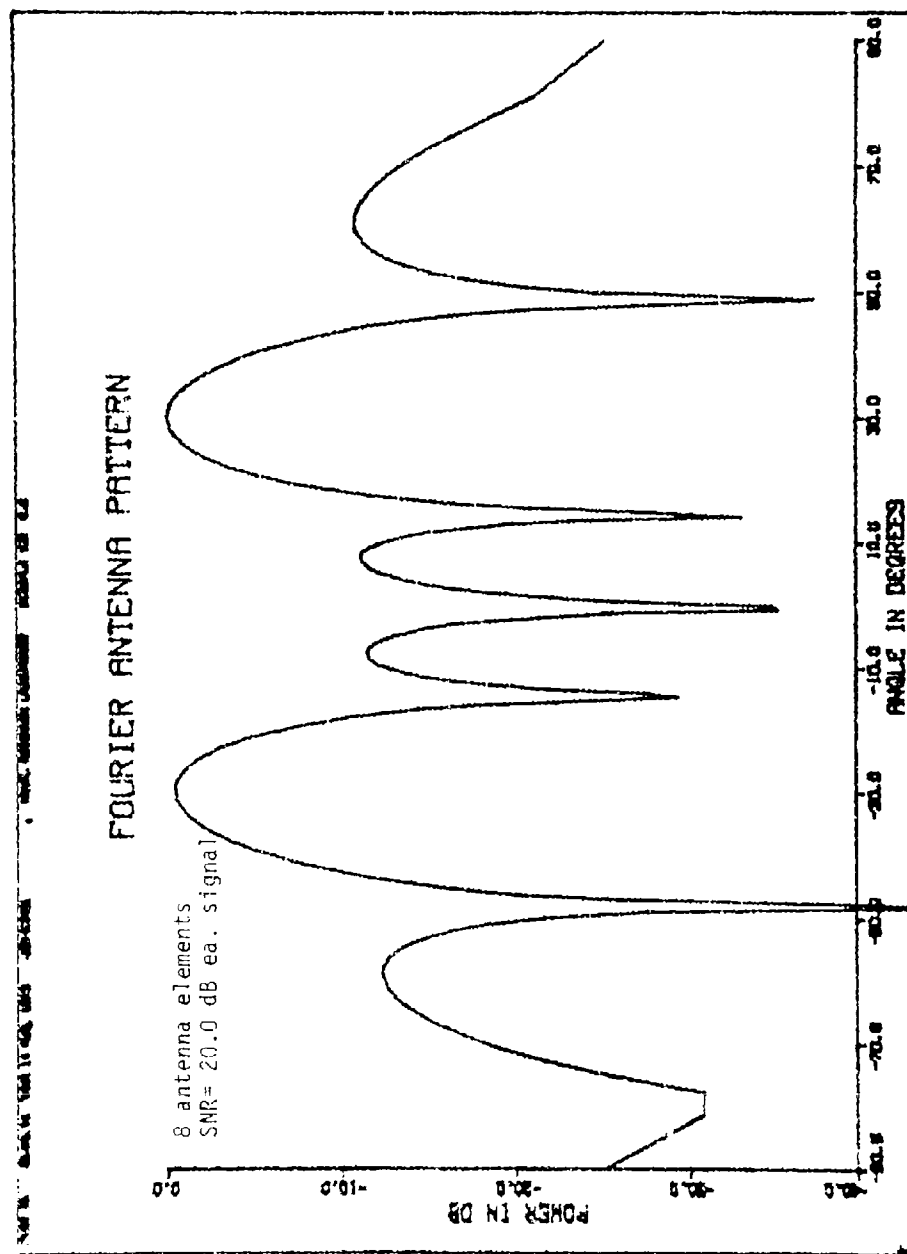
ONE SIGNAL AT 30 DEGREES

Fig. 3



TWO SIGNALS AT -30 and 30 DEGREES

Fig. 4



TWO SIGNALS AT -30 and 30 DEGREES

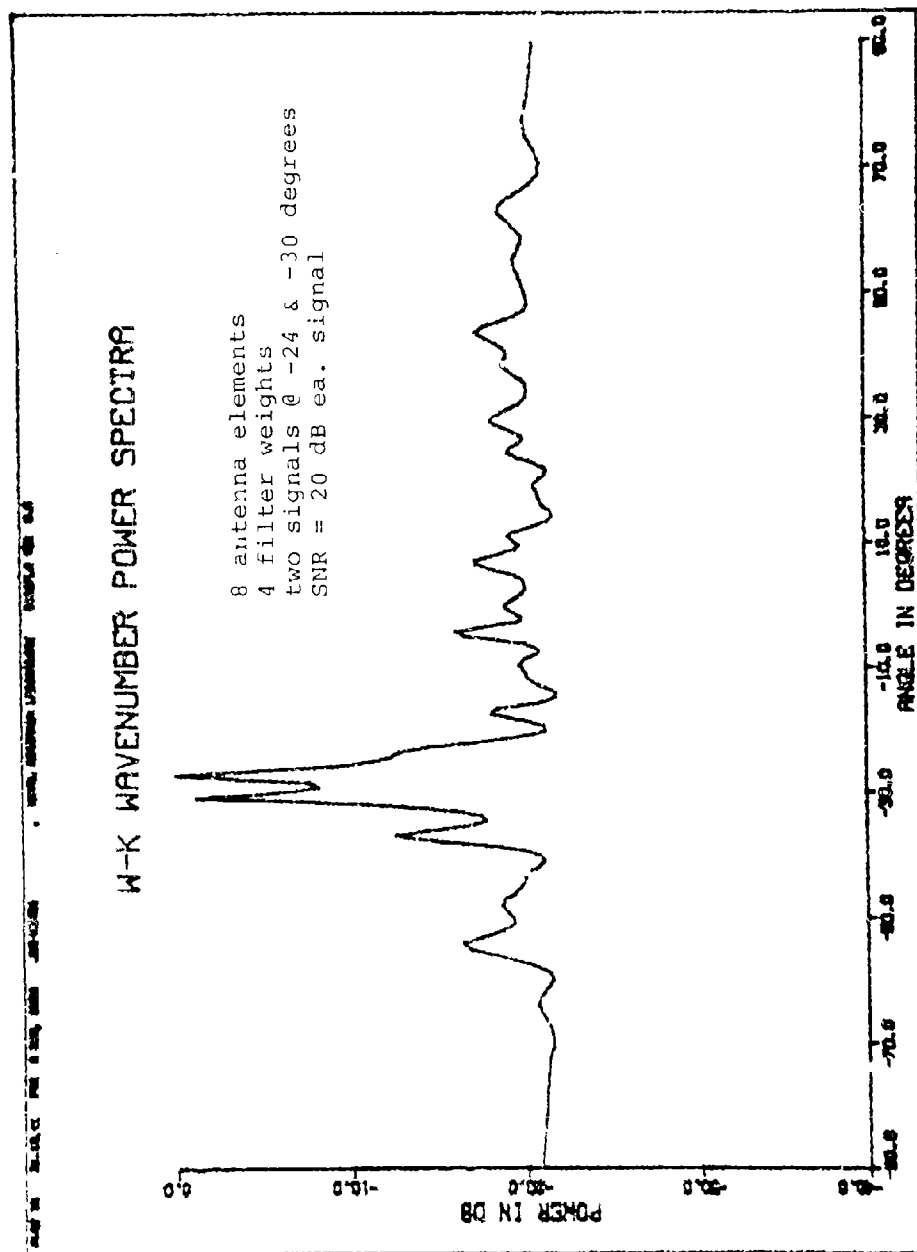
Fig. 5

the same two signals (SNR = 20 dB) and noise are shown in Fig. 5 detected by a conventional Fourier wavenumber antenna pattern. The strong Fourier side lobe structure that is present in Fig. 5 is only very mildly apparent in the W-K all-pole wavenumber spectra shown in Fig. 4. If the two spectra of Figs. 4 and 5 are superimposed, the Fourier side lobe structure is found to occur at the same spectral locations of the W-K side peaks. This similarity in side peak location is an indication of the stabilizing influence brought about by the presence of the Fourier transfer function $X(f_p)$ that appears in the W-K spectra formulization.

The resolution capability of the W-K spectral estimator is illustrated in Fig. 6, where two closely adjacent signals (6 degrees apart) are resolved by the W-K spectral estimator. For comparison purposes, the same two signals (SNR = 20 dB) are shown detected in Fig. 7 as a single peak in a conventional Fourier antenna pattern.

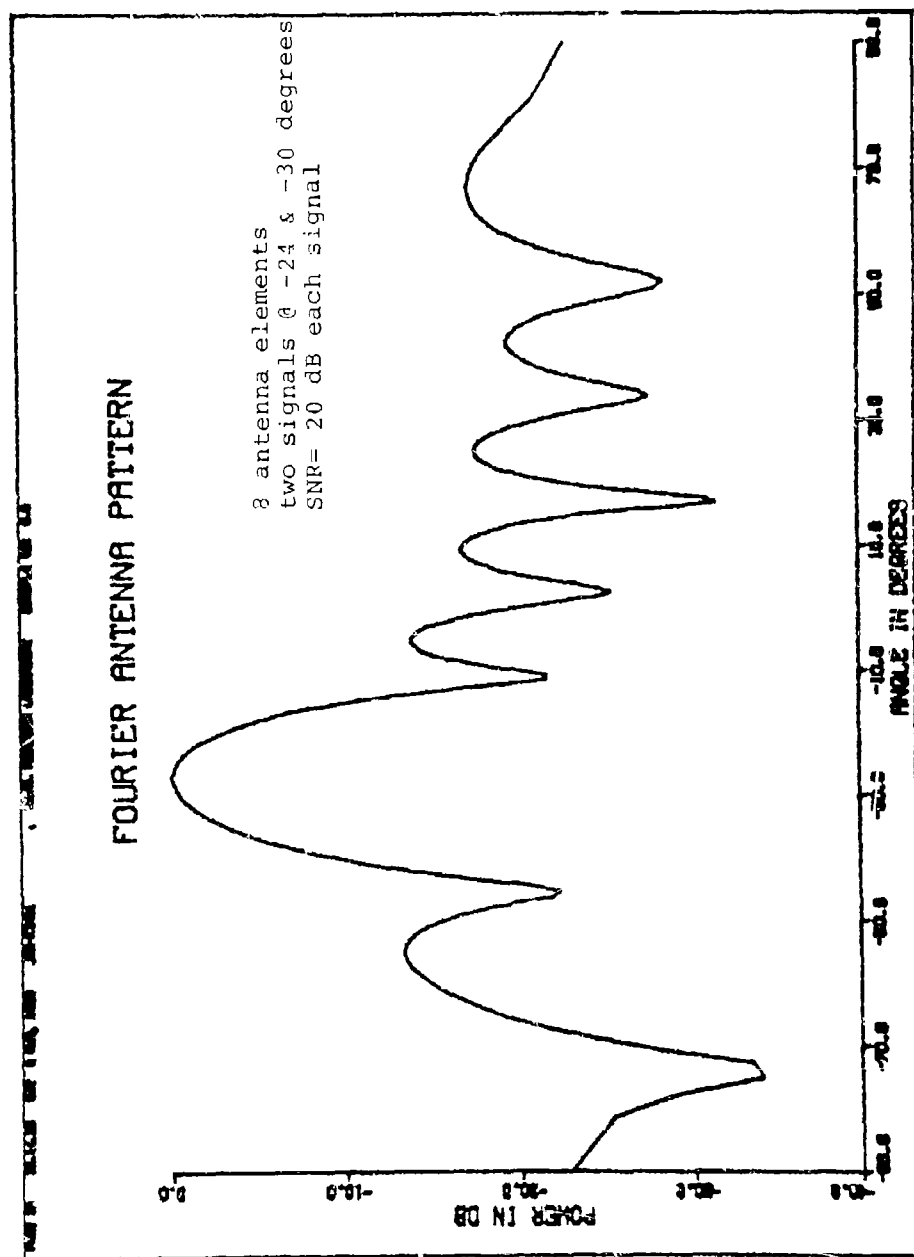
As had been anticipated, the W-K all pole spectral estimator is a very stable, high resolution spectral estimation technique. In all examples shown the computed wavenumber spectra is well whitened by the W-K spectral estimator. Spectral whitening is always achieved with only one snapshot of data. However some apparent improvements in this original version of the W-K spectral estimation technique are indicated by the example spectra. The small, numerous peaks that are often evident in the W-K spectra are a problem when they occur in the vicinity of a signal peak. In such instances the presence of the small, noisy peaks may be misintrepreted as a collection of several very close signals. Perhaps an improved version of the W-K estimator, or a simple correction of some overlooked programming error may serve to eliminate or at least minimize the presence of the small annoying noisy peaks.

The derivation of the W-K spectral estimator has utilized only the forward prediction error. Perhaps a minimization of the total (forward and backward) prediction error will serve to further improve the W-K spectral estimator.



TWO SIGNALS AT -24 and -30 DEGREES

Fig. 6



TWO SIGNALS AT -24 and -30 DEGREES

Fig. 7

REFERENCES

- (1) Steinberg, Bernard D., Principles of Aperture and Array System Design: including Random and Adaptive Arrays, John Wiley & Sons, New York, N. Y., 1976
- (2) King, W. R., "Maximum Entropy Wavenumber Analysis", NRL Report 8298, March 20, 1979

THE ALL-POLE AND ZERO-POLE FOURIER SPECTRAL ESTIMATOR

Introduction

The Wiener prediction filter is useful in deriving the high resolution maximum entropy and W-K spectral estimation techniques. Both of these spectral estimators employ prediction filters that are defined by minimizing a mean squared Wiener prediction error. The evaluation of these prediction filters may require the computation and manipulation of large matrices, which usually requires considerable computational time.

While these spectral estimation techniques have very unique and useful properties, it is also possible to obtain another useful spectral estimator by utilizing a very simple, and quickly computed, prediction filter. The resultant spectral estimator is named the "Fourier spectral estimator", because it employs only the Fourier transform of the data set. The Fourier spectral estimator (FSE) may be derived either as an all-pole or as a zero-pole model. Both models are presented in the analysis that follows.

Wiener Prediction Filter

Narrowband spectral components in a detected signal may be characterized with use of the Wiener prediction filter as follows:

$$A_p e^{i\omega_p t} = \hat{x}(t) - e(t) \quad (1)$$

where A_p and ω_p are the amplitude and frequency of a narrowband component, and $e(t)$ is the spectral prediction error. The prediction signal $\hat{x}(t)$ may be taken as the convolution of the prediction filter $b(t)$ with the measured function $x(t)$

as follows:

$$\hat{x}(t) = \int_{-\infty}^{\infty} b(\tau-t)x(\tau)d\tau \quad (2)$$

Filter Definition

The prediction filter $b(t)$ is usually defined by minimizing the mean squared prediction error. However it is much easier to choose a prediction filter that yields a zero prediction error at the exponential frequency ω_p . The filter is defined in the frequency domain by combining the Fourier transforms of eqns. (1) and (2) as follows:

$$A_p \delta(\omega - \omega_p) = B(\omega, t)X(\omega) - E(\omega) \quad (3)$$

If $E(\omega) \rightarrow 0$ as $\omega \rightarrow \omega_p$, then it follows from eqn. (3) that

$$B(\omega_p, t) = A_p / X(\omega_p) \quad (4)$$

All Pole Solution

Even though eqn. (4) is correct, ω_p is not known and it is not possible to evaluate $X(\omega_p)$. However, for high SNR values $X(\omega_p)$ is approximately equal to its maximum magnitude X_0 , which is more readily determined. The prediction filter transfer function may be specified approximately as follows:

$$B(\omega_p, t) \approx A_p / X_0 \quad (5)$$

By combining eqns. (3) and (5) the narrowband component amplitude is given as follows:

$$A_p \approx A_p X(\omega_p) / X_0 - E'(\omega_p) \quad (6)$$

$$A_p \approx -E'(\omega_p) / \{1 - X(\omega_p)/X_0\} \quad (7)$$

where $E'(\omega_p)$ is the prediction error due to the approximate value of the prediction filter transfer function used in eqn. (7). An all pole, white, spectral power ratio may be obtained from eqn. (7) as follows:

$$|A_p/E'|^2 \approx 1 / |1 - X(\omega_p)/X_0|^2 \quad (8)$$

The frequency ω_p of the exponential components may be approximated by determining the complex poles of eqn. (8).

Zero-Pole Solution

At spectral regions other than ω_p eqn. (3) reduces to the following expression for the prediction error:

$$E(\omega) = B(\omega, t) X(\omega) \quad (9)$$

The most obvious choice for the filter transfer function is zero, however it may be more preferable to choose $B(\omega, t) = 1.0$, so that

$$E(\omega) = X(\omega) \quad (10)$$

The choice of eqn. (10) permits other filter methods to be applied for the elimination of strong interference signals, that may otherwise appear as a pole in eqn. (8). A zero-pole Fourier power spectra results from combining eqn. (10) and eqn. (7) to obtain an expression useful over the entire frequency domain. The zero-pole Fourier spectral estimator is given as follows:

$$A_p A_p^* \approx |X(\omega) / (1 - X(\omega)/X_0)|^2 \quad (11)$$

Example Spectra

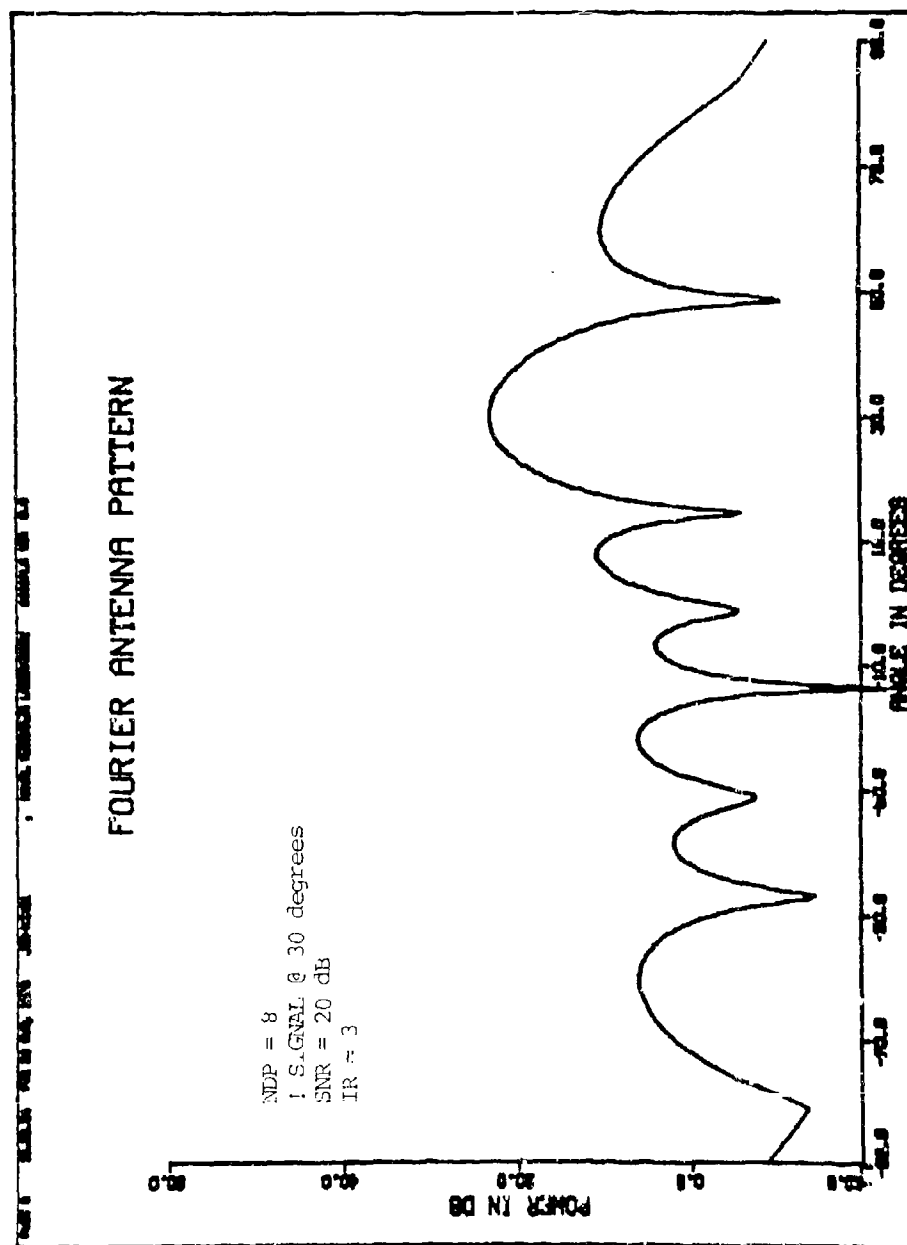
The conventional Fourier antenna pattern is compared with several examples of the stable, all-pole and zero-pole Fourier spectral estimator (FSE). All examples are snapshot antenna and wavenumber spectral patterns, that are computed for signals of 20 dB SNR which are incident to an 8 element, linear, antenna array. The white, Gaussian amplitude noise data is identical ($IR=3$) in every example presented.

The conventional Fourier antenna pattern for one signal incident at 30 degrees is shown in Fig. 1. The same signal is shown detected with the all-pole, Fourier estimator in Fig. 2, and with the zero-pole Fourier estimator in Fig. 3. Other comparative examples include two widely spaced signals incident at -30 and 30 degrees that are shown in Figs. 4, 5, and 6; two closely adjacent signals incident at 30 and 45 degrees, which are shown in Figs. 7, 8, and 9. One other set of examples (Figs. 10, 11, and 12) show five signals, all with the same power level (20 dB SNR), incident at angles of -60, -45, 0, 30, and 37 degrees.

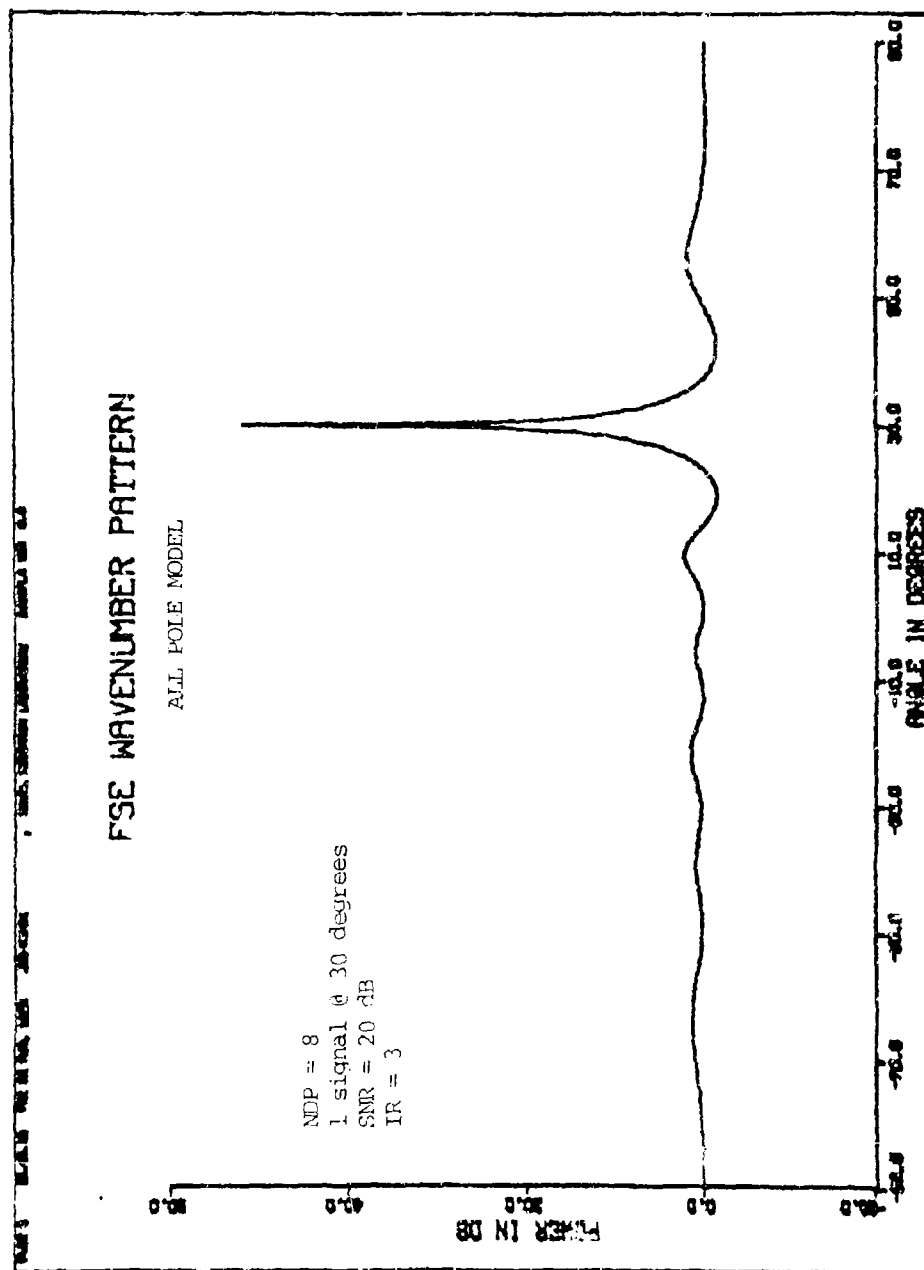
In all the examples shown, the FSE technique appears to have improved spectral accuracy and improved resolution and detection capability in comparison with the conventional Fourier power spectral method. The derivation of the FSE technique appears to indicate that these improved spectral characteristics are more significant with increasing SNR levels.

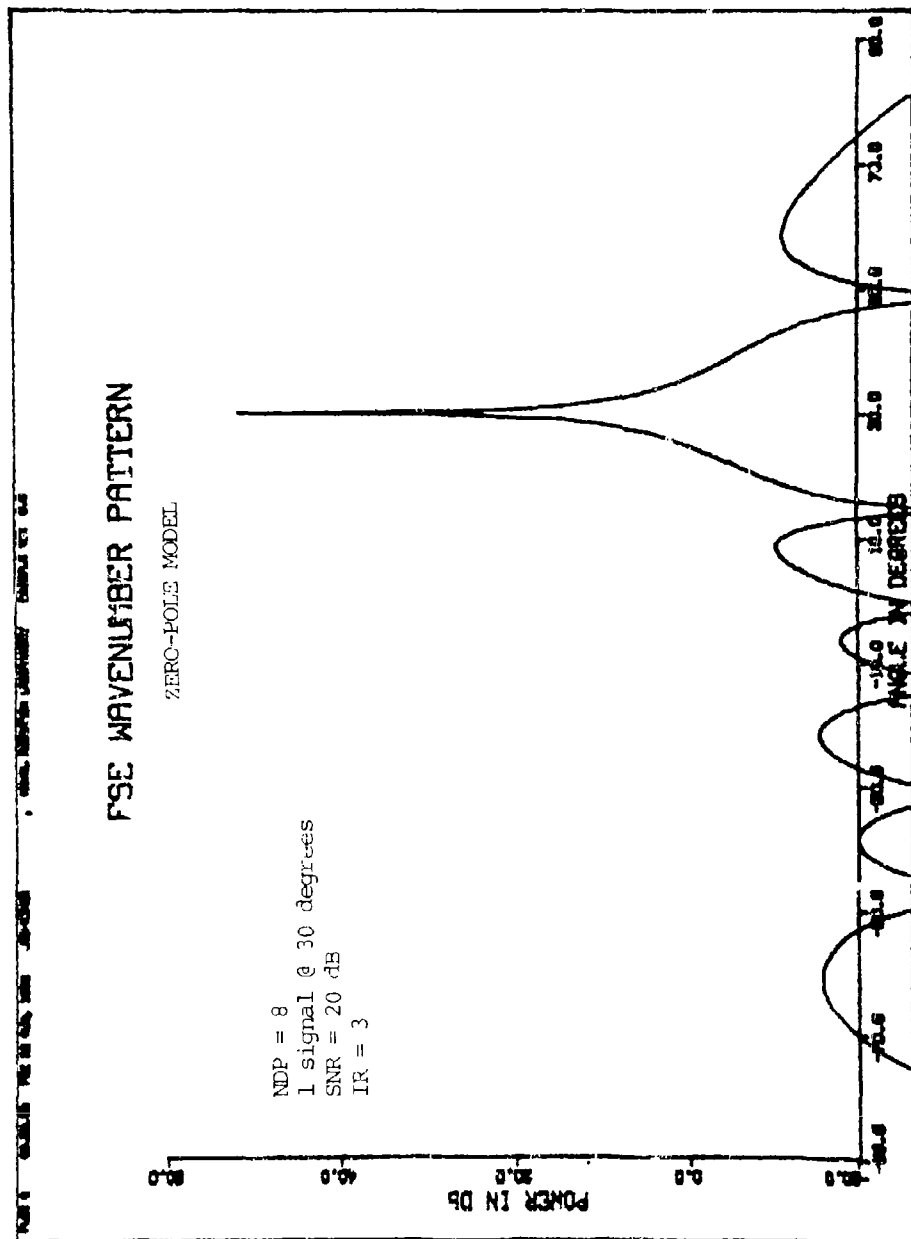
In the Fourier antenna pattern of Fig. 10, the signal power levels of the three signals detected near 0, 30, and 37 degrees are in error by several dB. These same errors are, in effect, magnified by the FSE examples given in Figs. 11 and 12. Consequently signal power levels indicated by either FSE technique, are in much greater error than the power levels indicated by the conventional Fourier antenna pattern. It may be difficult to measure either absolute or relative power levels from computed FSE wavenumber spectra.

Perhaps all signal parameters may be more accurately determined by using both the conventional Fourier spectral and the Fourier spectral estimator techniques. Hopefully the FSE detection, resolution, and spectral characteristics may be determined in a future extensive analysis.



ONE SIGNAL AT 30 DEGREES



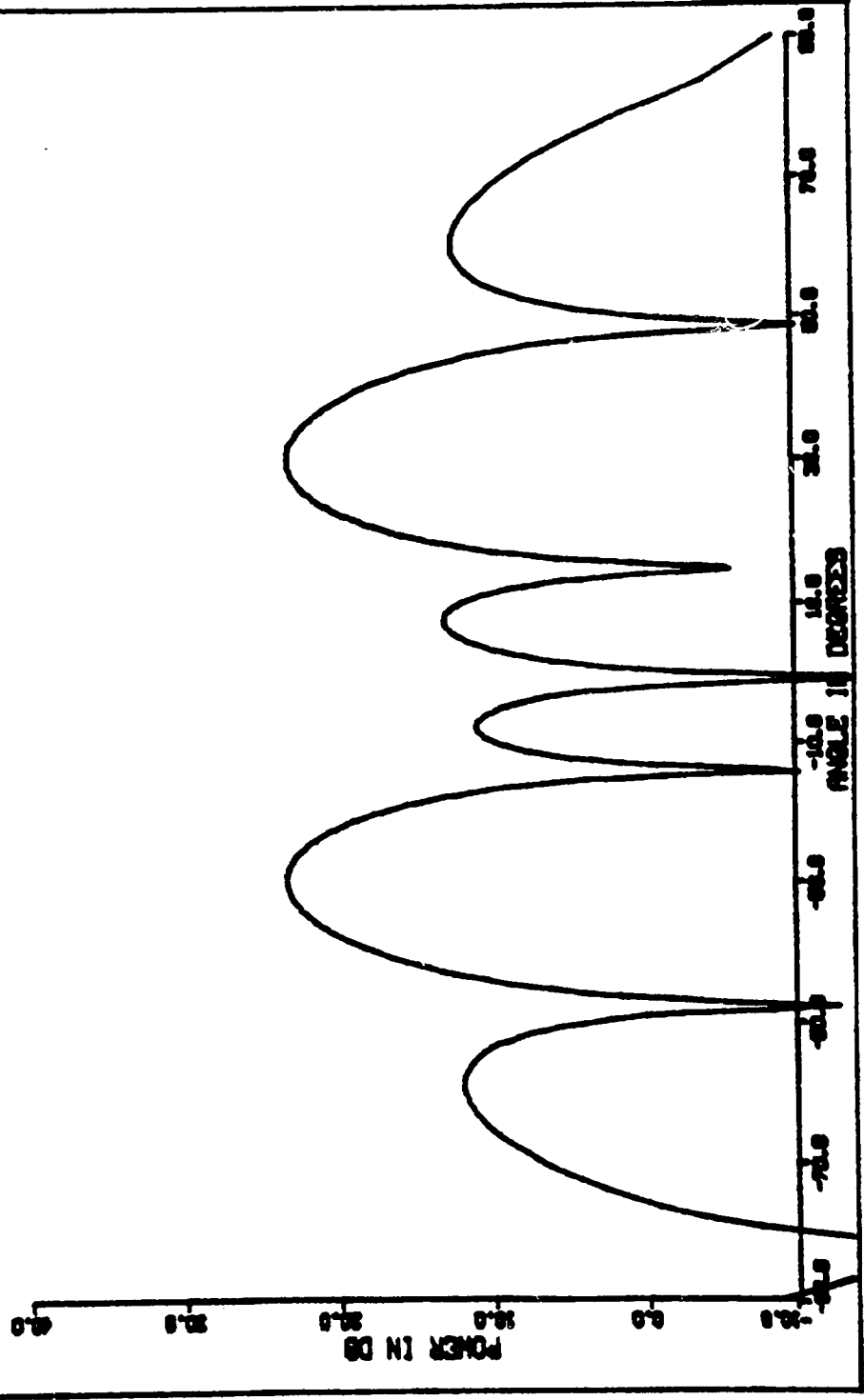


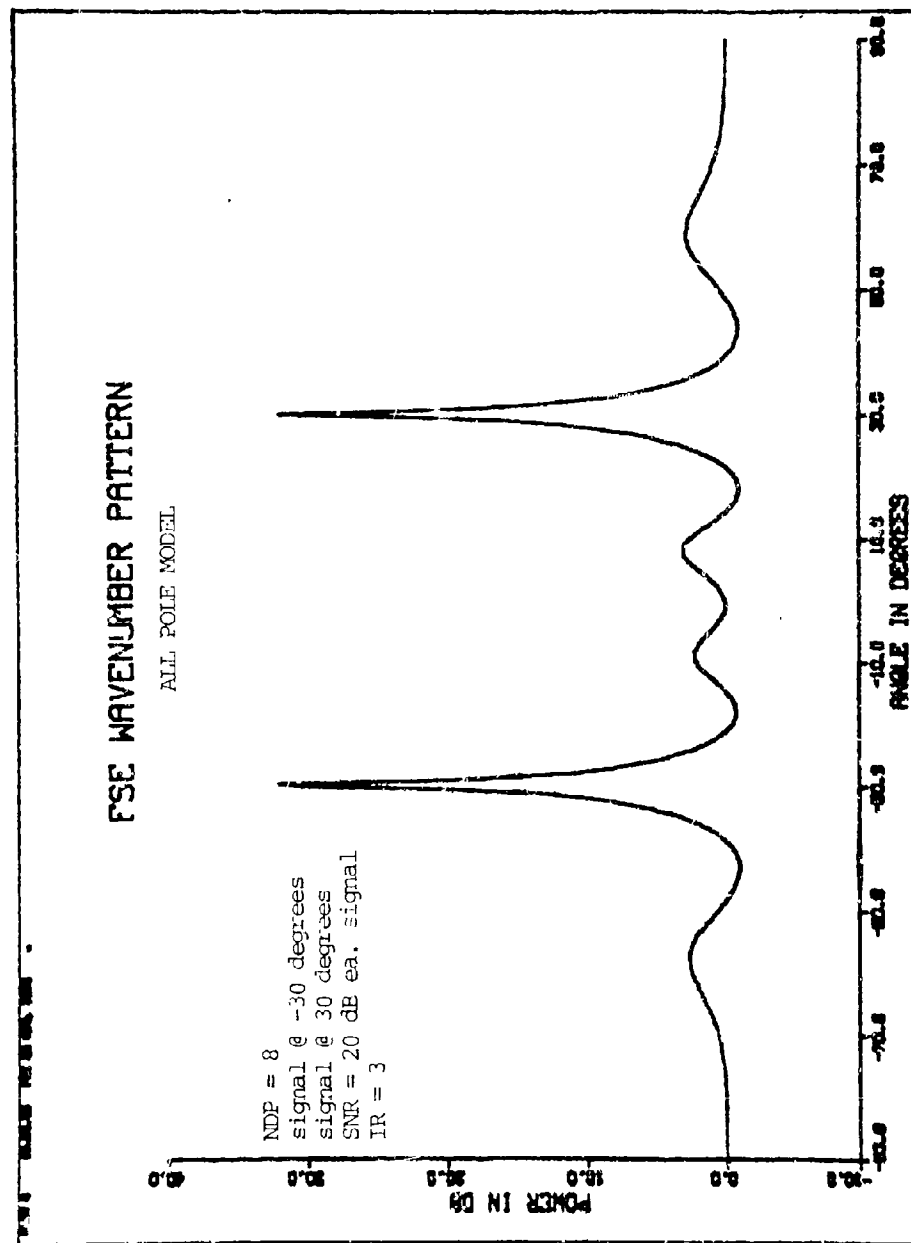
ONE SIGNAL AT 30 DEGREES

FOURIER ANTENNA PATTERN

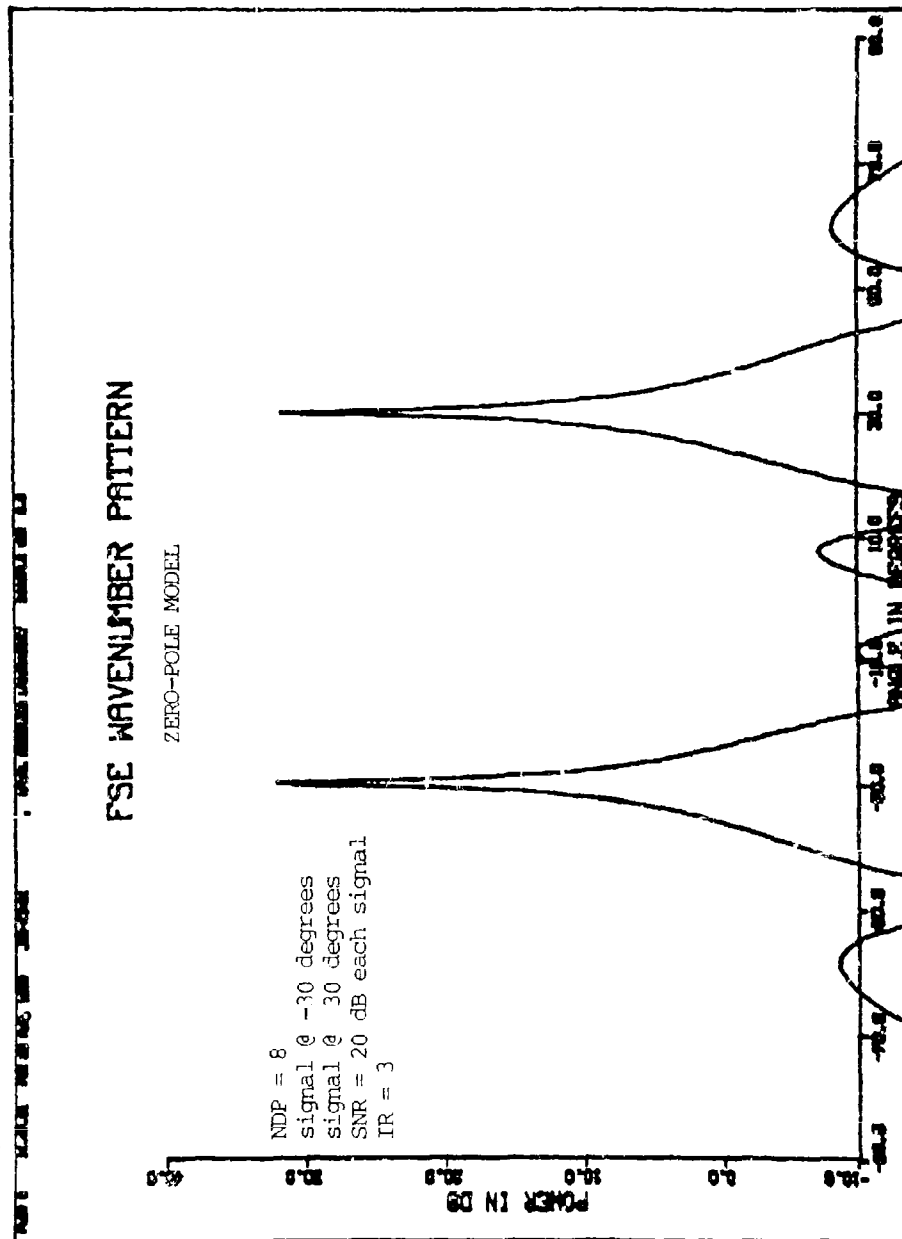
Angle in Degrees	Power in dB
-90.0	-15.0
-75.0	-10.0
-60.0	-5.0
-45.0	0.0
-30.0	15.0
-15.0	25.0
0.0	35.0
15.0	25.0
30.0	15.0
45.0	0.0
60.0	-5.0
75.0	-10.0
90.0	-15.0

FOURIER ANTENNA PATTERN



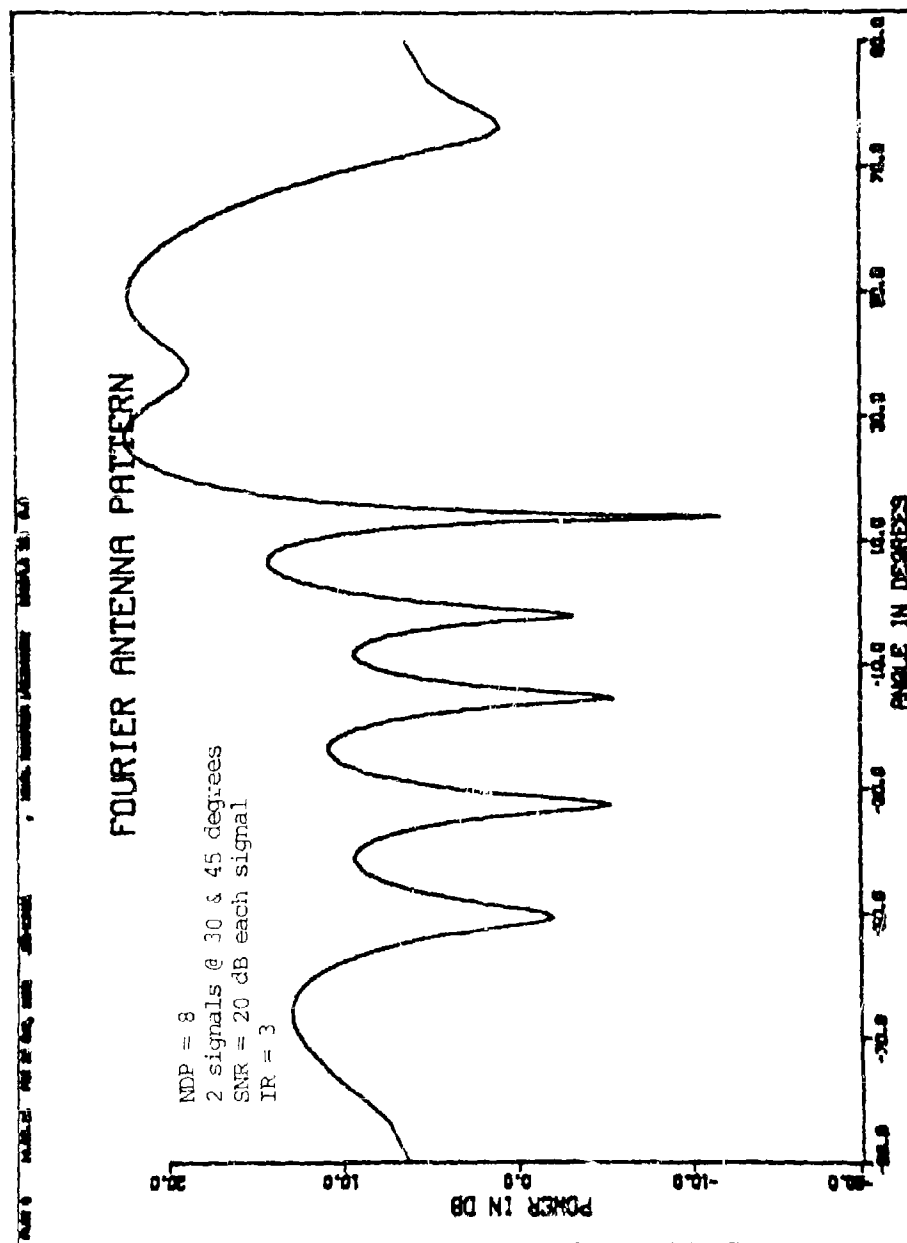


TWO SIGNALS AT -30 and 30 DEGREES
ALL POLE MODEL

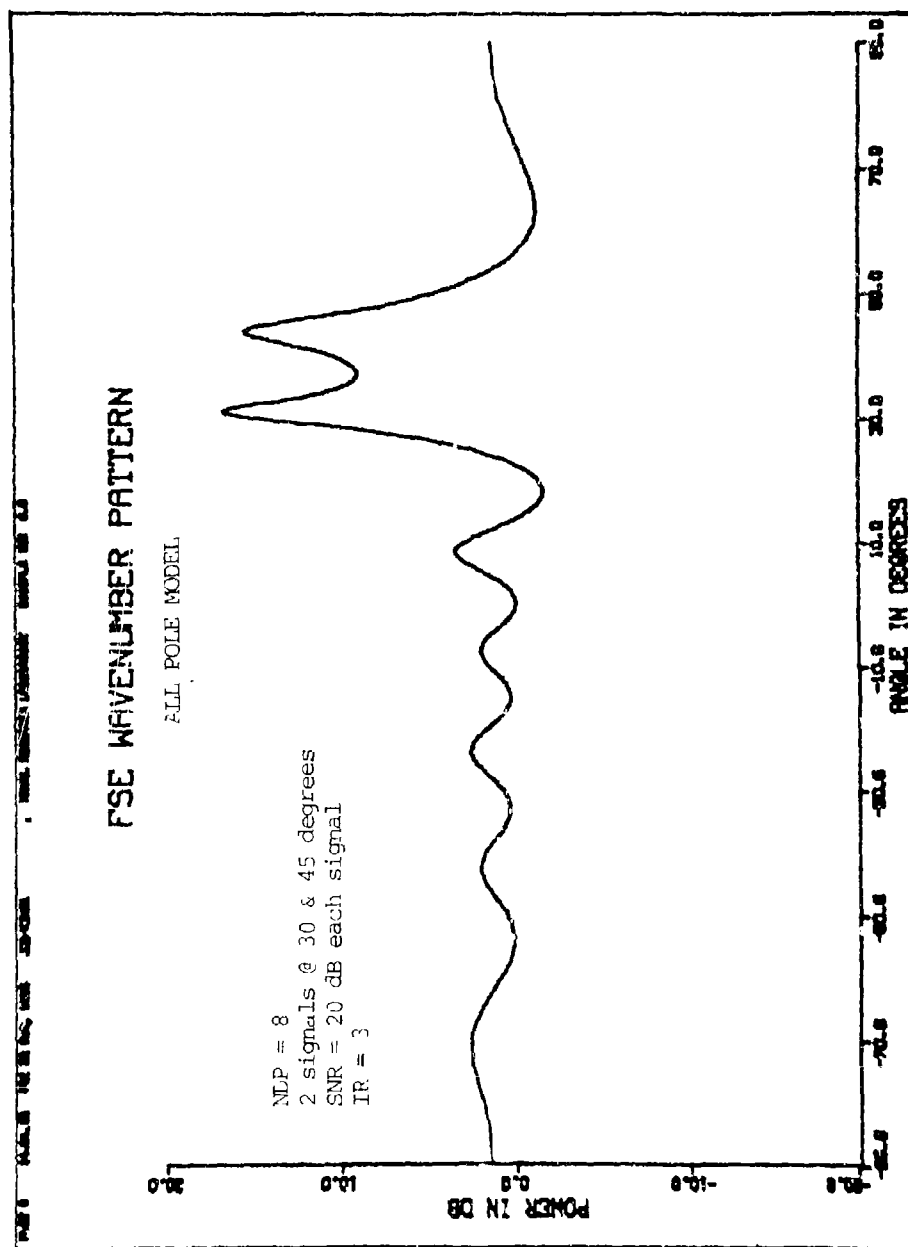


TWO SIGNALS AT -30 and 30 DEGREES

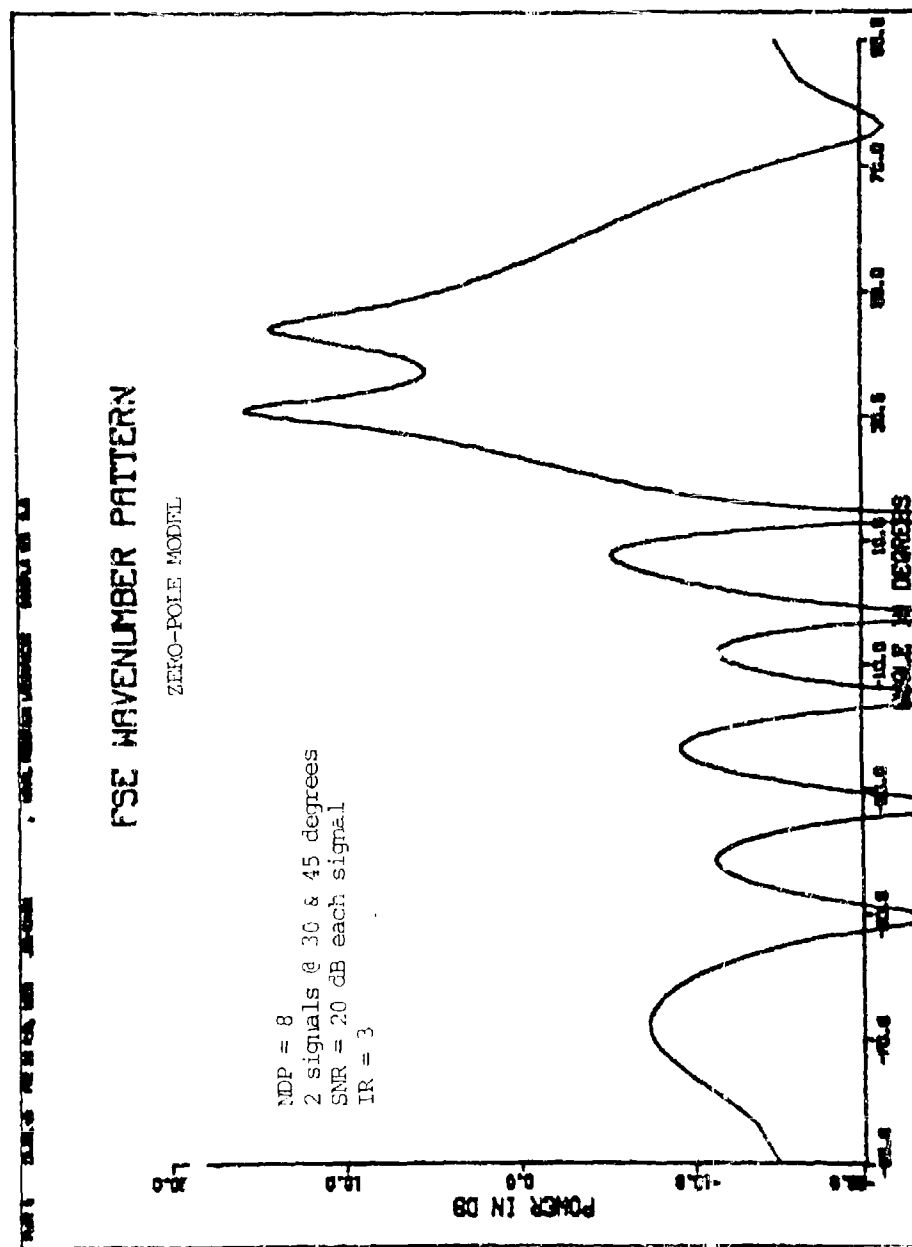
ZERO-POLE MODEL



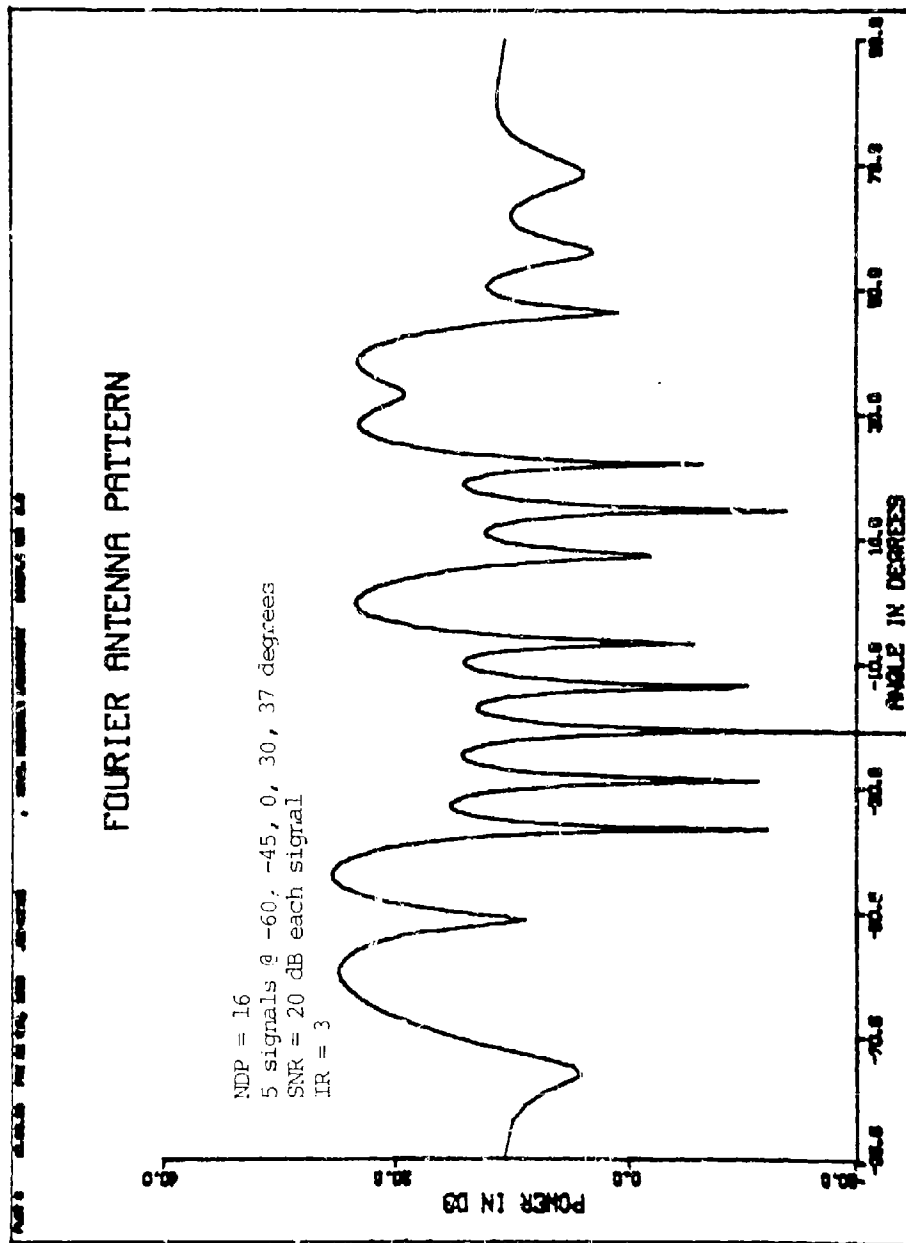
TWO SIGNALS AT 30 AND 45 DEGREES



TWO SIGNALS AT 30 AND 45 DEGREES



TWO SIGNALS AT 30 AND 45 DEGREES



FIVE SIGNALS

